The Cosmic Ray Background at L_2 as Seen in *Gaia* Observations

Master's Thesis in Physics

Presented by
Christian Thomas Kirsch
Tuesday 30th October, 2018

Dr. Karl Remeis-Sternwarte Bamberg
Friedrich-Alexander-Universität Erlangen-Nürnberg

Supervisor: Prof. Dr. Jörn Wilms

Abstract

For any space telescope, an important part of the signal background is caused by energetic particles known as cosmic rays, which in worst cases make certain scientific observations impossible. At the second Lagrangian point of the Sun-Earth system, understanding this background signal is extremely important, due to the many highly sensitive astronomy missions planned to orbit this point in the near future. As the only active observatory at L_2 since 2014, the European Space Agency's *Gaia* satellite is an important laboratory for this background component, especially given its large focal plane with many individual CCD sensors.

In this thesis, I develop software pipelines to systematically extract cosmic ray tracks from a selection of raw *Gaia* observations, creating a catalog containing both on-chip particle rates and individual event properties such as the ionizing energy deposited by each particle. The extraction algorithms used therein are custom-developed to separate the cosmic ray background from the science signal of each observation type and produce a final, shared data product for all observation types.

After their extraction, I first internally compare datasets extracted from different observations, finding them to be mostly consistent aside from slight systematics due to differences in the science signal and CCD types. I also find the extracted on-chip rates to be consistent with existing on-board event rejection counters for cosmic rays.

In comparing on-chip particle rates from *Gaia* to particle data from other spacecraft, I find that the *Gaia* data traces both the evolution of galactic cosmic ray rates over the solar cycle as well as solar particle events detected by other particle monitors. Additionally, I find significant differences between the intensity-time profiles of solar particle events seen in different *Gaia* chips, which can be traced back to the different radiation shielding of *Gaia*'s CCDs due to their location on its focal plane.

Finally, I compare the measured energy loss of particles both outside of and during solar particle events, finding distributions consistent with a galactic cosmic ray background dominated by minimum ionizing particles as well as a strong excess of lower energy particles during solar particle events.

Contents

Chapter 1

Introduction: Cosmic Rays and their Effects on Spacecraft

Cosmic Rays, discovered during balloon flights by Hess (1912), are a population of high energy particles originating from various extraterrestrial sources. Since their discovery, they were found to mostly consist of protons (90 %, Blasi (2013)), with the rest made up by ionized heavier elements. In order to discuss their origin, it is easiest to divide them into particles originating from the Sun and from outside the solar system.

Varying conditions in the solar system, including cosmic rays, are referred to as space weather. Due to their effects on both ground- and space-based infrastructure, developing an understanding of these phenomena has become increasingly important. In the following, I will briefly summarize the origin of cosmic rays, their measurement in space and the hazardous effects they can have on satellites.

1.1 Solar Cosmic Rays

Energetic particles originating from the Sun can be divided into two categories (Schwenn, 2006) – a fairly steady stream of magnetized plasma called the solar wind and a more energetic population referred to as solar energetic particles (SEPs) emitted in bursts.

The solar wind itself originates from active regions near the Sun's equator as well as from coronal holes at quiet zones near its poles. Outflows from these regions make up the turbulent *slow solar wind* and the less turbulent *fast solar wind*.

This outflowing plasma carries the Sun's magnetic field into the rest of the solar system as magnetic field lines curved like Archimedean spirals, called *Parker spirals*. When interacting with planetary magnetospheres, it causes the formation of their characteristic extended tails and bow shocks.

As mentioned above, SEPs usually appear in discrete events, with bursts of electromagnetic and energetic particle fluxes. These events are understood to originate from solar flares and coronal mass ejections (CMEs) (Reames, 1999). Solar flares are a result of particle acceleration within magnetic loops in the Sun's upper atmosphere, releasing both particles and bremsstrahlung across many wavebands (Klein & Dalla, 2017). CMEs, on the other hand, are outbursts of large amounts of solar plasma, often associated with flares or other forms of solar activity. While their precise mechanism is still debated, they are, like solar flares, understood to be powered

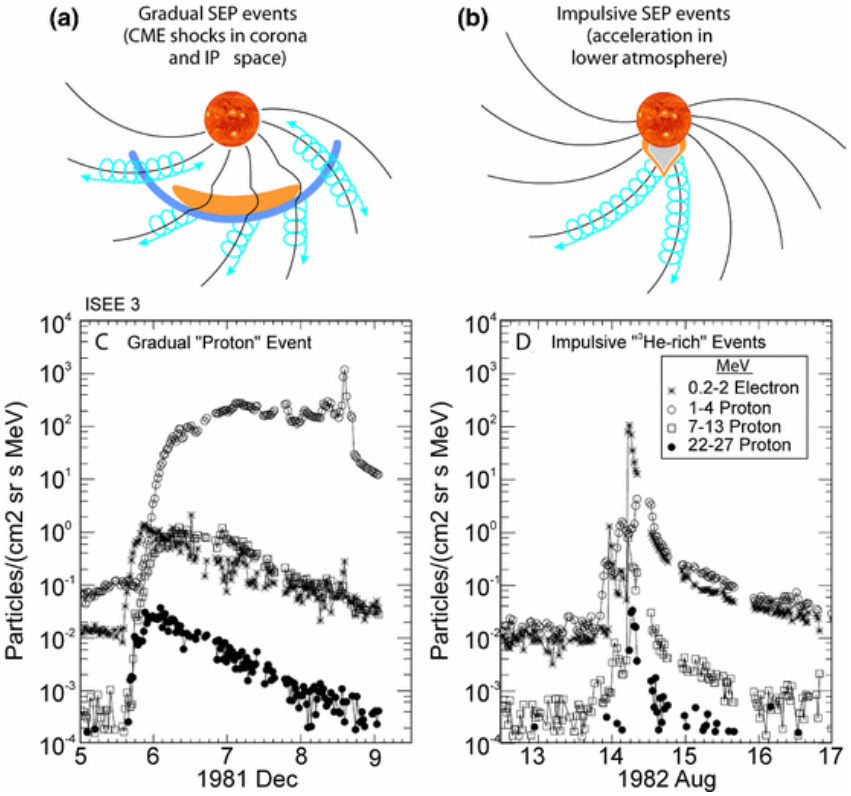

Figure 1.1: Models and observational signatures for for gradual, CME driven SEP events (left) and impulsive events (right). In the former, the interplanetary magnetic field is populated with SEPs over a large longitudinal area. Impulsive events, on the other hand, populate only well-connected field lines. Figure taken from Desai & Giacalone (2016), where it is in turn adapted from Reames (1999).

by the release of magnetic energy from the Sun. Once ejected, a CME drives a shock wave in the previously released solar plasma, accelerating a large population of particles. Figure 1.1 illustrates this two-class picture of SEP events.

For an observer, the two types of SEP events are most easily separated by their differences in X-ray and particle intensity timescales – impulsive flare events lasting several hours as opposed to the more gradual CME events spanning days – as well as their elemental abundances, as CME events match solar abundances, while flare SEPs have enhanced ^{3}He/^{4}He and Fe/O ratios (Reames, 1999).

The frequency of these events, alongside other aspects of solar activity such as the sunspot number and radio flux, all vary within an 11 year *solar cycle* (Hathaway, 2015). In these cycles, observations show a single minimum of solar activity with up to two fairly close maxima, the last maximum as of this report having been in the early year 2014, with decreased activity since then.

1.2 Galactic Cosmic Rays

Compared to solar cosmic rays, galactic cosmic rays distinguish themselves by their relatively high energies. Fig. 1.2 shows the differential all-particle spectrum for galactic cosmic rays, which shows a steep decrease in energy with notable features named *knees* and *ankles*. The reason behind these features is still under debate, but are speculated to be due to galactic accelerators reaching their maximum energies for the knees and the domination of extragalactic particles in the ankle region (Tanabashi et al., 2018).

Supernova remnants are a strong candidate for a galactic source of GCRs, thought to bring them to high energies via shock acceleration (Blasi, 2013). Evidence of protons with GCR energies

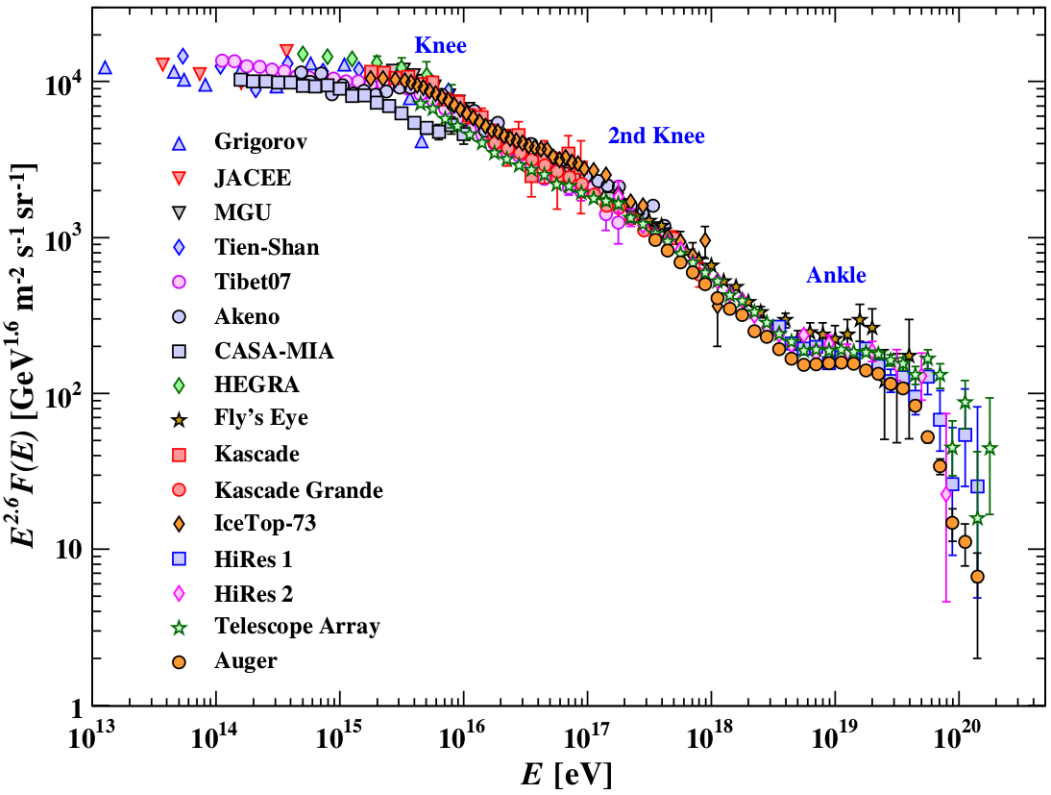

Figure 1.2: The all-particle differential spectrum of galactic cosmic rays as measured from air showers. The spectrum has been multiplied by a factor of $E^{2.6}$ to better display notable the knee and ankle features. Figure taken from Tanabashi et al. (2018).

in supernova remnants has been found by Ackermann et al. (2013) via the decay signature of pions produced by high energy protons interacting with interstellar material, supporting this model. Especially the more energetic ultra high energy cosmic rays, however, are proposed to come from other sources, such as active galactic nuclei (Anchordoqui, 2018).

When considering cosmic rays observationally, it is also interesting to note that the overall cosmic ray flux undergoes periodic modulations, with the dominant timescale being the aforementioned solar cycle (Potgieter, 2013). Concretely, GCR intensities are anticorrelated to solar activity. While precise modeling of these modulations is complex, it is generally understood that GCRs are deflected by the extended heliosphere and its magnetic field, which is richer in plasma during active periods.

1.3 Satellite-Based Measurements

Especially in the case of solar particles, satellite-based measurements have contributed a large amount of knowledge to the field of cosmic rays, providing in-situ measurements of the solar wind, observations of the same event in multiple locations (Reames, 1999) and generally giving a view of particles unobscured by the shielding of Earth's magnetic field. Especially measurements using multiple spacecraft have greatly contributed to the understanding of both the sources (Reames, 1999) and propagation of solar particle events throughout the solar system, improving on the single-point measurements that could be taken from Earth and satellites in close orbit (Battarbee et al., 2018).

While the precise instrumentation of particle sensors is mission specific, most modern satellites utilize solid state telescopes for the detection of particles and the measurement of their characteristica. For these solid state detectors, signals are formed via the excitation of electrons in the semiconductor material via electronic interactions.

At the energies relevant for this thesis, the mean rate of energy loss of a charged particle in a solid is well-described by the *Bethe equation* (Tanabashi et al., 2018),

$$\left\langle -\frac{dE}{dx} \right\rangle = Kz^2 \frac{Z}{A} \frac{1}{\beta^2} \left[\frac{1}{2} \ln \frac{2m_e c^2 \beta^2 \gamma^2 W_{\max}}{I^2} - \beta^2 - \frac{\delta(\beta\gamma)}{2} \right], \tag{1.1}$$

with the constants being

- the standard relativistic kinematic variables β and γ of the charged particle
- the charge number z of the incident particle
- the vacuum speed of light c
- the electron mass m_e
- the atomic number Z and mass A of the absorber
- the absorber's mean excitation energy I
- the constant $K = 4\pi N_A r_e^2 c^2$, with Avogadro's number N_A and classical electron radius r_e
- the maximum energy transfer to an electron in a single collision
$W_{\max} = [2m_e c^2 \beta^2 \gamma^2]/[1 + 2\gamma m_e/M + (m_e/M)^2]$, with M being the particle's mass
- a relativistic density effect correction $\delta(\beta\gamma)$

the thus-defined energy loss is often given in units of units of $\mathrm{MeV\,g^{-1}\,cm^2}$ as a *mass stopping power*, and given the medium's density ρ is easily converted to a *linear stopping power* $\rho \cdot \langle -dE/dx \rangle$ as the energy loss per unit of length in, e.g., MeV/cm.

Figure 1.3 plots this mass stopping power for a variety of materials and charged particles. Notable characteristics of these curves are the steep decay until $\beta\gamma \approx 1$, dominated by the $1/\beta^2$-term of Eq. 1.1, followed by a local minimum and a logarithmic increase. Particles with momenta corresponding to this local minimum are referred to as *minimum ionizing particles* (MIPs). These particles most easily penetrate materials and make up a majority of particles that reach shielded detectors.

As a note of caution, it should be pointed out that while the Bethe equation approximates the mean energy loss of a charged particle via ionization, the statistical distribution of energy losses does not follow a simple distribution like a Gaussian, but rather the asymmetric *Landau-Vavilov* distribution (Landau, 1944), a distribution with a long tail to high energies, for which a mean is actually undefined. The sample mean thus varies strongly with the number of measurements and energy cut-off chosen for statistics, making the most probable energy loss of a particle a better measurement value (Tanabashi et al., 2018).

In semiconductors, the energy transferred to valence electrons in a particle's path is sufficiently high to transfer the electron to the conduction band, creating an electron-hole pair. These electron-hole pairs are generated along the path of the particle through the material, creating a track of charges (see Fig. 1.4). These signal charges are then collected via electrodes, where the position of the electrodes and exact method of signal collection depend on the detector specification and its requirements in timing, energy resolution and other aspects.

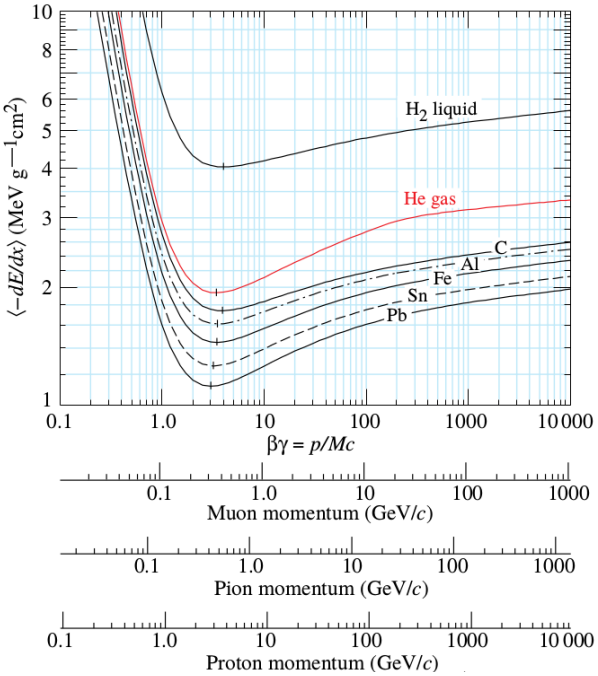

Figure 1.3: Mean ionizing energy loss rates for a variety of materials. The relativistic $\beta\gamma$ has been converted to particle momenta for muons, pions and protons. Figure taken from Tanabashi et al. (2018).

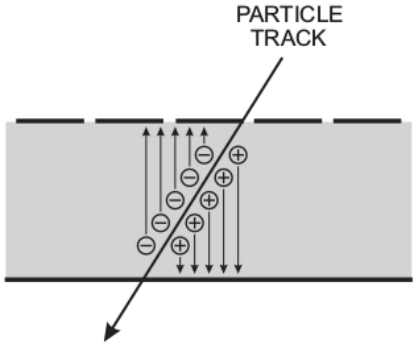

Figure 1.4: Formation of a particle track via ionization, taken from Spieler (2005) for the example of a gas detector; the same principle holds in a semiconductor. Segmented electrodes (on the top) allow for the detection of the track location.

To measure a particle flux coming from within a fixed solid angle, satellite particle detectors often employ a telescope scheme, here explained by the example of the Solar Isotope Spectrometer (SIS) (Stone et al., 1998) on the *Advanced Composition Explorer* (*ACE*) (Stone et al., 1998) mission. As shown in Fig. 1.5, an entrance window allows only particles within a restricted opening angle to enter the telescope, where they subsequently interact with a series of detectors, each providing a measurement of the energy deposited by a particle. The individual stack detectors each provide signals that can be combined to – in the case of the Solar Isotope Spectrometer – determine the charge, mass and energy of a measured particle.

By then converting raw particle counts to differential particle fluxes using telescope-dependent conversion factors (Sullivan, 1971), data from different satellites and instruments thereof can be treated in a uniform manner for scientific analysis (Battarbee et al., 2018).

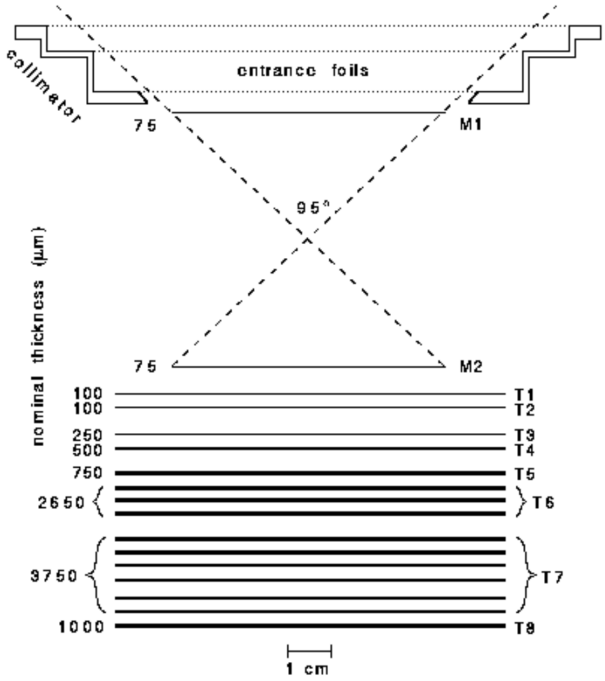

Figure 1.5: Scale drawing of an *ACE* SIS telescope, showing only active detector regions. The two detectors labeled as M1 and M2 are position sensitive matrix detectors to determine particle entrance angles. The labeling on the left displays total silicon thicknesses in μm for each labeled detector. In the case of T6 and T7, the signals of several individual detectors are combined into one.

1.4 Radiation Effects on Satellites

Far from being only a matter of scientific interest, cosmic rays have important effects on any spacecraft which are crucial both in their design and operation.

One problem posed by cosmic rays is in their direct interaction with spacecraft electronics (Adams, 1985). In such interactions, the energy deposited by a cosmic ray interaction in a microprocessor can cause a logical error (referred to as "single event upsets") flip bits in solid state memory or even potentially destroy microelectronics. Normal modern processors, being extremely miniaturized, are especially vulnerable to such effects due to the high density of circuitry. As such, spacecraft need to utilize specialized radiation-proof electronics.

Additionally, particles interacting with semiconductors can cause what is referred to as *displacement damage*, modifying their crystal lattice and causing defects that can trap charges and effectively change the detector doping and band gap (Horne et al., 2013). This effect may eventually end a satellite's operations, as the power supplied by commonly used solar panels is reduced by this effect, with a single SEP event causing power losses in the order of 1-2 %, in addition to the constant degradation due to GCRs and the solar wind. Aside from solar panel degradation, displacement damage also affects the performance of any solid state detectors on a satellite, which may be a dominating factor in some scientific mission's lifetimes (Crowley et al., 2016). Furthermore, cosmic rays can electrostatically charge a satellite both internally and externally, causing additional issues for its electronics (Horne et al., 2013).

For astronomical satellites in particular, cosmic rays are often a source of background signal which needs to be removed from actual scientific observations. Notable examples of such missions include imaging missions such as *Hubble*, where cosmic ray tracks in images inhibit their scientific use, requiring either special observation strategies or removal algorithms (Salzberg et al., 1995; van Dokkum, 2001). In the *Planck* satellite, cosmic ray impacts were picked up by bolometers as temperature spikes, which make data unusable for scientific analysis (Miniussi et al., 2014). X-ray missions are historically affected by cosmic rays, with flaring due to SEP events or passages

through Earth's radiation belts degrading images, light curves and spectra by creating fake events in their detectors through ionization, which are energetically too similar to photons to distinguish them (Walsh et al., 2014; Molendi, 2017; Eckart et al., 2018).

Given these issues, it is especially important for astronomical satellites, equipped with increasingly sensitive detectors, to understand their radiation environment, as with ESA's Standard Radiation Environment Monitors (Mohammadzadeh et al., 2003), to shield their detectors and to understand the remaining particle background in their measurements (Gastaldello et al., 2017).

In this thesis, I will systematically extract the cosmic ray background signal in observations of the *Gaia* mission. This mission will be described in Chapter 2, where we will see that it provides an excellent laboratory for a radiation background that will affect many future astronomical missions due to its large focal plane equipped with many CCD detectors as well as its orbit around the Sun-Earth L_2 point.

Following this motivation, Chapter 3 will develop software pipelines to extract a catalog of cosmic ray events from several different types of observations on *Gaia*. This will be achieved by algorithms tailored to each dataset, using techniques such as simple signal thresholding, morphological separation of cosmic ray tracks from stars and the stacking of sequential images. Based on this event detection, we will then determine individual event properties such as the deposited energy per particle and convert individual *Gaia* observations into measurements of the on-chip particle rate.

Chapter 4 will outline a first analysis of our dataset focused on data validation. This includes a comparison of *Gaia* datasets internally, where we will focus on the recovered particle rates and deposited energies, which we will both find to be consistent when observing the same particle environment. Afterwards, we will compare the particle rates as a function of time from our data with proton fluxes from particle monitors on other satellites, finding both a consistent galactic cosmic ray background and solar particle events. Using the latter, we will also see that there is a significant difference in the particle shielding of *Gaia*'s CCDs on different parts of its focal plane, as indicated by earlier modeling. Lastly, we will use particle track data to estimate the ionizing energy loss rate of cosmics on Gaia's FPA, which will be consistent with high-energy galactic cosmic rays and lower energy solar particles.

Chapter 5 will then summarize our results and list future applications of and refinements to the dataset generated in this work.

Chapter 2

Gaia

Gaia (Gaia Collaboration et al., 2016) is a science mission of the European Space Agency launched in December 2013. Being an astrometry mission, its primary goal is the determination of both the positions and proper motions of more than a billion stars to high precision, along with the spectroscopic determination of key stellar parameters. Using 22 months of data, the recent second *Gaia* data release (DR2, Gaia Collaboration et al. (2018)) already contains celestial positions and apparent brightnesses for 1.7 billion stars, with parallaxes and proper motions available for a subset of 1.3 billion sources. This data provides a map of the Galaxy unprecedented in detail as seen in Fig 2.1, which shows a color map generated from the *Gaia* catalog and further indicates the wealth of knowledge of the galactic structure within this data.

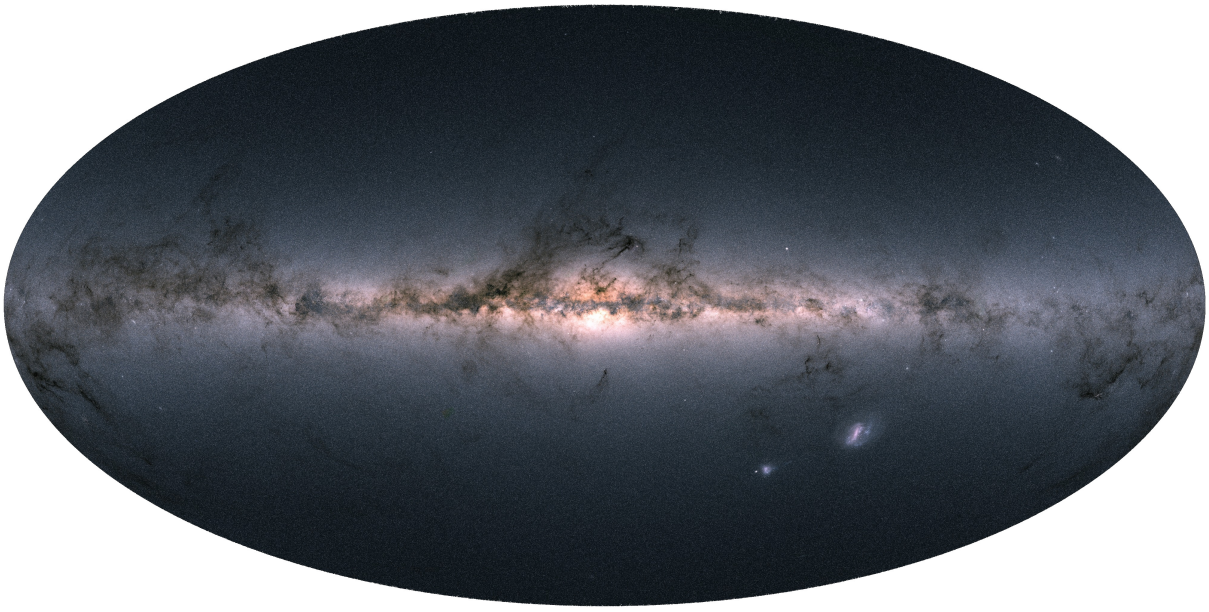

Figure 2.1: Map of source fluxes in *Gaia*'s color bands as a Hammer projection of the full sky. Image taken from Gaia Collaboration et al. (2018).

In order to make its precise distance measurements, *Gaia* determines the absolute stellar parallaxes of its target sources. To achieve this, the spacecraft images two fields of view separated by an angle of 106.5° onto the same detector using two identical telescopes (Fig. 2.2, left), determining the angular distances in the sky of simultaneously imaged stars via their positions on its focal

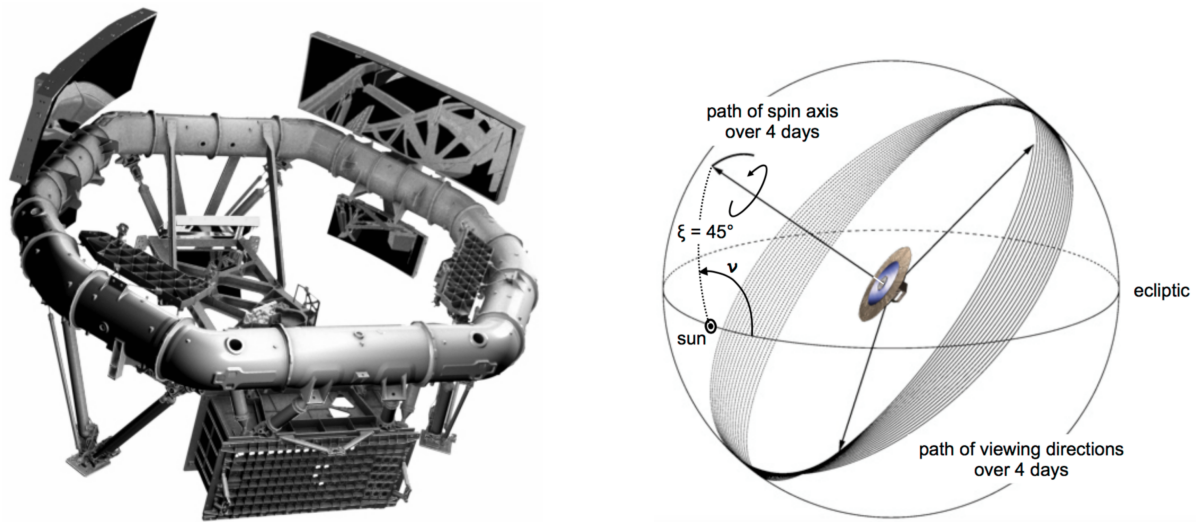

Figure 2.2: *Left:* Schematic overview of *Gaia*'s payload module. The primary mirrors of the two telescopes are mounted above the hexagonal structure, while the Focal Plane Assembly is mounted on the bottom, towards the viewer. *Right:* Illustration of *Gaia*'s scanning law, showing its movement relative to the ecliptic and the path of its viewing directions over four days. Both images taken from Gaia Collaboration et al. (2016).

plane. By spinning with a period of 6 h, with its spin axis precessing around the Sun (Fig. 2.2, right), *Gaia* scans the sky and determines the relative positions of many pairs of stars. Using this network of relative source positions, detailed on-ground processing calculates the positions, parallaxes and proper motions of the imaged sources (Lindegren et al., 2018).

In the following, we will describe *Gaia*'s focal plane and the different measurements using its detectors. With its unique focal plane and orbit around the Sun-Earth L_2 point, we will then motivate the use of *Gaia* as a particle environment monitor.

2.1 Focal Plane and Measurements

One of the key elements to *Gaia*'s high precision is without a doubt its focal plane assembly Kohley et al. (2012). Containing 106 individual CCDs with a total of almost one billion pixels, its focal plane spans roughly 1 by 0.5 m, being the largest ever flown in space. Figure 2.3 shows both a photograph of the FPA with all CCDs mounted and a schematic description.

As the figure shows, *Gaia*'s FPA actually uses three variants of the same e2v CCD91-72 chips. Their common feature are their rectangular pixels of 10 by 30 μm, being thinner in the direction of the apparent movements of stars. This movement direction defines the *along-scan* (AL) direction on the focal plane, as opposed to the *across-scan* (AC) direction perpendicular to it. The different chip variants are:

- AF-type: A broadband standard silicon chip with a thickness of 16 μm.
- BP-type: A blue-optimized standard silicon chip with a thickness of 16 μm.
- RP-type: A red-optimized, deep-depletion silicon chip with a thickness of 40 μm.

A star imaged by *Gaia*'s telescopes drifts across the FPA in the along-scan direction, left to right in Figure 2.3. Each chip that a star drifts across effectively creates a single image of the star

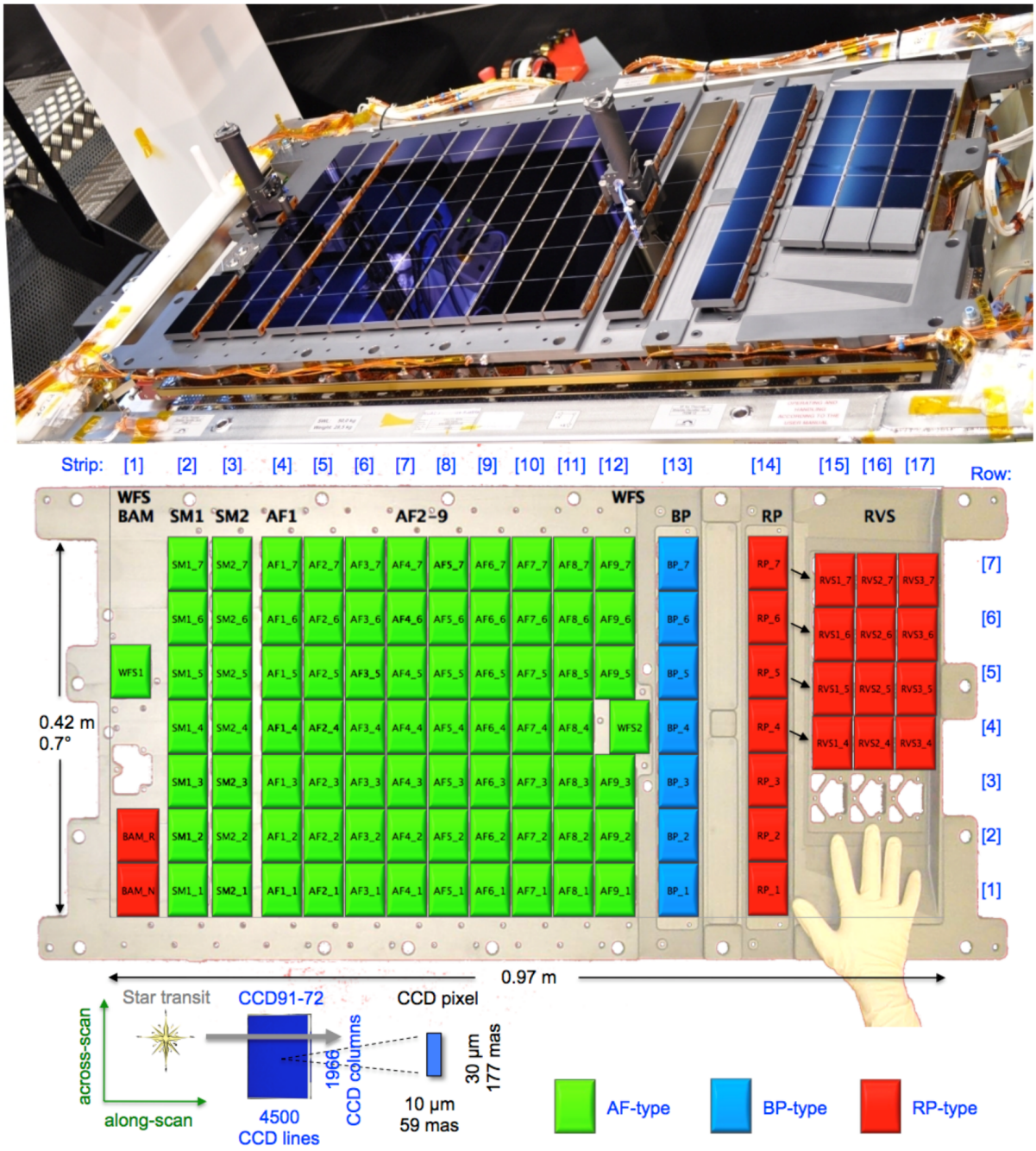

Figure 2.3: Picture and schematic of *Gaia*'s FPA with all CCDs mounted to the structure. Chip coloration in the bottom image indicates the three variants of e2v CCD91-72 chips used, as well as the assignment of each chip to different instruments. Figure taken from Kohley et al. (2012).

by using *Time-Delay-Integration* (TDI), where charges are shifted at the same rate that a star moves across the FPA. The accumulated charges thus follow the movement of the star across the chip, which in turn is continuously read out. This is opposed to typical CCD readout, where an image is integrated in place for a fixed amount of time and then read out at once.

Stars first appear on one of the *Sky Mapper* (SM) chips, with optical paths set such that stars from the first telescope only appear on the SM1 column and those of the second telescope on the

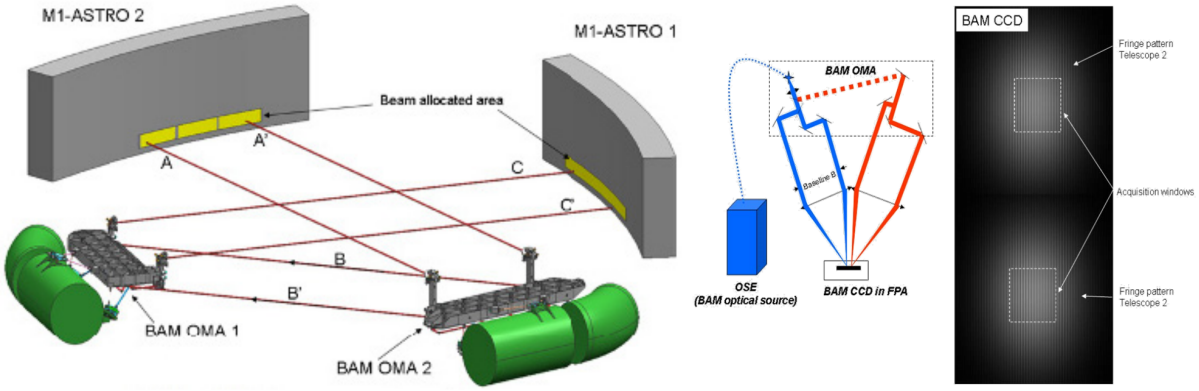

Figure 2.4: Overview of the basic angle monitor. *Left and Middle:* The two optical benches divide the light of a single source laser into four beams, injecting two into each telescope entrance pupil. *Right:* This creates one Young interference pattern per telescope on a BAM CCD. The movements of their fringes track changes in the basic angle. Figure and modified caption taken from Mora et al. (2016).

SM2 column. This way, objects are first assigned to their respective fields of view and readout windows for all interesting objects are created for the following chips.

After the SM, all stars drift across the *Astrometric Field* (AF), whose images are used to determine their relative positions. It should be noted that only data from readout windows created via the Sky Mapper are recorded and down linked, due to bandwidth constraints.

Following the astrometric field, stars are imaged in the blue and red photometer chips (BP and RP), with blue and red fused-silica prisms in the optical paths of the respective columns enabling two-color photometry.

The rightmost group of chips belong to the *Radial-Velocity-Spectrometer*, with an optical grating mounted in the optical path to the respective chips. For sufficiently bright stars, the taken spectra yield radial velocities via their Doppler-shifts and a subset of stellar and astrophysical parameters, such as selected abundances and interstellar reddening.

The two WF-chips left and right of the astrometric field are the detectors for *Gaia*'s wave-front sensors, assessing the optical performances of their respective telescopes and allowing for alignment and focussing.

The BAM chips, making up the detectors for the basic angle monitoring device, are not used for astronomical imaging, instead being utilized to track the angle between the two individual telescopes. As the core principle of *Gaia*'s measurements is the determination of the angular distance of sources imaged separately by the telescopes, any variations in this basic angle need to be tracked to high precision.

The evaluation and results of these basic angle measurements are described in detail by Mora et al. (2016) and shown in Fig. 2.4. As described in the figure, light from a single laser is split into four beams, with two beams each injected into entrance pupils of both telescopes. These beams create an interference pattern for each telescope on the BAM chips. Using the movement of their fringes, these inteference patterns can be used to track variations of the basic angle on the level of μas.

It should be noted here that there are in fact two sets of the basic angle monitor aboard *Gaia*, using the BAM_N and BAM_R chips respectively. The second unit is kept as a redundant unit in case of failure of the nominal instrument and has not been used so far.

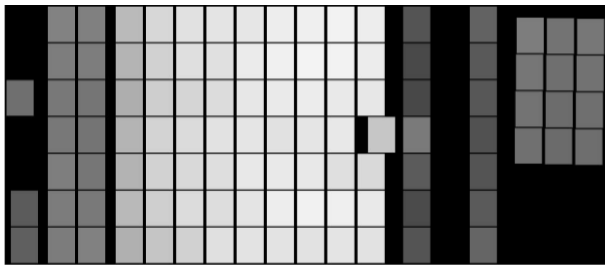

Figure 2.5: Results of a sector analysis by EADS Astrium, showing the expected proton irradiance until the *Gaia*'s end of life. Values are plotted in gray scale per chip, ranging from 1.4 to 3.9×10^9 protons/cm^2, the maximum value being the brightest. The varying shielding is best explained using Fig. 2.6. Image taken from Kohley et al. (2012).

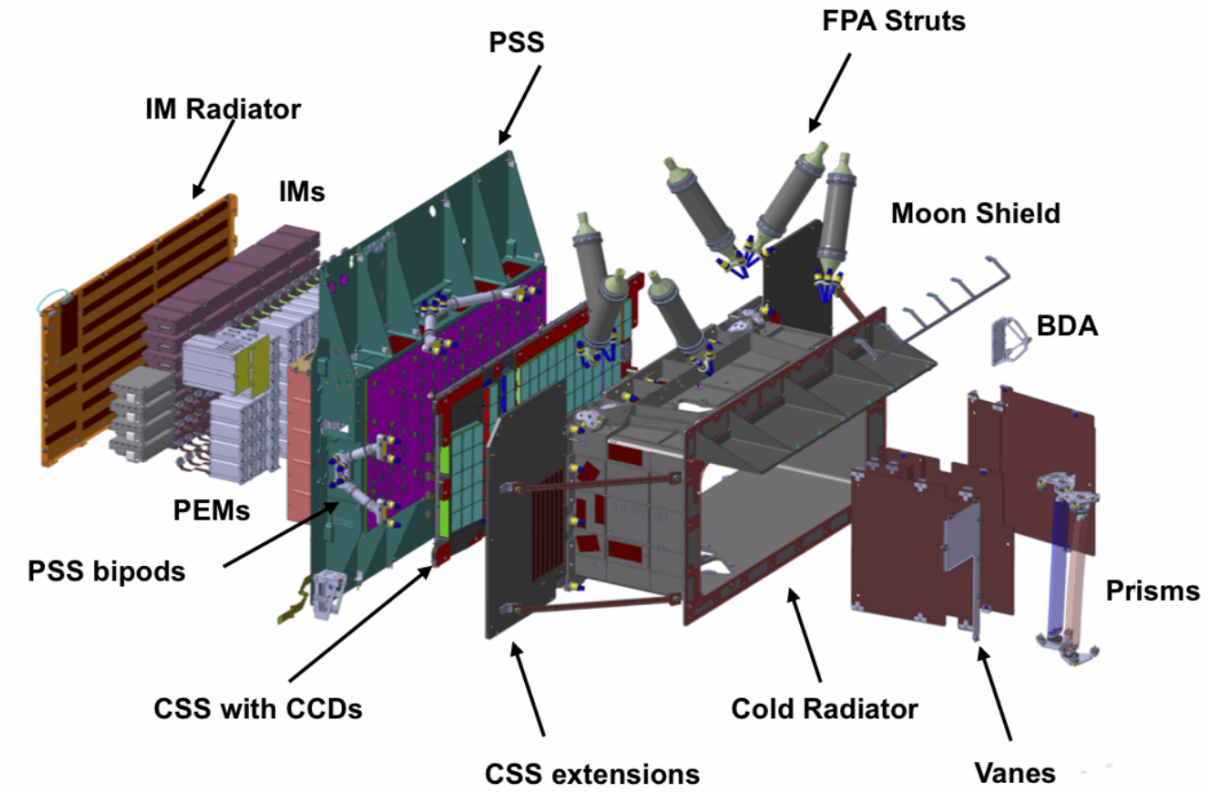

Figure 2.6: Schematic composition of *Gaia*'s FPA. As seen by the arrangement of the CCDs, the FPA is rotated by 180° relative to Fig. 2.3. The most likely sources for the gradient in proton irradiance from Fig. 2.5 are the cold radiator, the photometer prisms and vertical vanes. Image taken from Kohley et al. (2012).

Given the variety of measurements *Gaia* makes with its large set of CCDs, radiation damage is a serious concern for the continued operation of the spacecraft. Of special note is the reduction of a CCDs *charge transfer efficiency* – the success rate of charge shifts in a CCD – due to radiation damage, given the constant shifting of charges in TDI mode, where inefficiencies can easily distort images and thus measurements of positions. Accordingly, a sector analysis by EADS Astrium was made before the mission, whose results in units of proton irradiance are shown in Fig. 2.5.

In short, the total proton irradiance, especially in the astrometric field, increases in the along-scan direction, with the proton flux being reduced for certain chips due to additional components installed in front of them. A probable main cause of this feature is the composition of the FPA which the CCDs are embedded in, shown in Fig. 2.6.

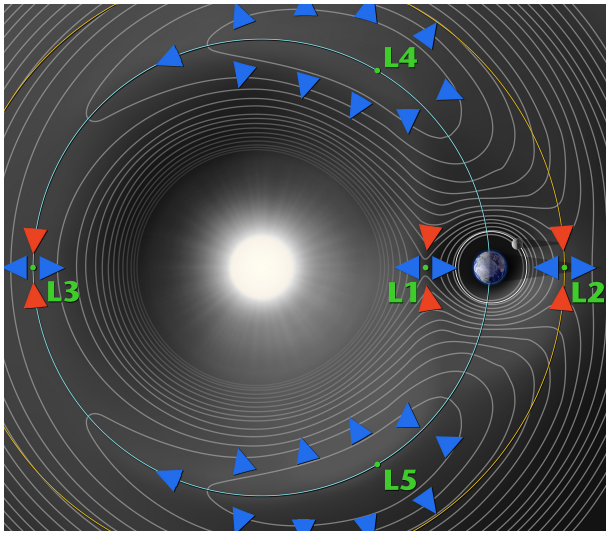

Figure 2.7: Contour plot of the effective potential in the co-rotating Sun-Earth system, not to scale. The Lagrangian points are marked, with blue and orange arrows indicating decreasing and increasing potential, respectively. Figure taken from NASA web-pages, retrieved from `https://solarsystem.nasa.gov/resources/754/what-is-a-lagrange-point/`, 26-10-2018.

Crowley et al. (2016) have also analyzed the performance of *Gaia*'s CCDs after two years of exposure to its radiation field. They find a spatial distribution of damage as indicated by the earlier sector analysis, with the degradation of the charge transfer being an order of magnitude below initially expected values.

2.2 Lagrangian Point L_2

The Lagrangian points are special points in celestial mechanics (Fitzpatrick, 2012), existing as points in the co-rotating system of two orbiting bodies which a satellite can orbit with low or no fuel consumption. Figure 2.7 gives an overview of these Lagrangian points in the Sun-Earth system.

The second Lagrangian point of the Sun-Earth system – from here on referred to as L_2 – is of special interest for astronomical missions. Located 1.5 million km or 0.01 AU from Earth in opposition to the Sun, it has been used by observatories such as *WMAP* (Bennett et al., 2003), *Planck* (Tauber, J. A. et al., 2010) and *Herschel* (Harwit, 2004). Furthermore, planned observatories such as the *James Webb Space Telescope* (Gardner et al., 2006), *Spectrum-Roentgen-Gamma* (Pavlinsky et al., 2008), *Athena* (Nandra et al., 2013) and many more have either selected or favor an orbit around L_2. Most relevant for this thesis, *Gaia* also orbits the L_2 point in a Lissajous orbit (Gaia Collaboration et al., 2016), being the only active spacecraft there since the start of its operations.

Compared to an orbit close to Earth, L_2 orbits have the benefit of a stable thermal environment for the spacecraft by avoiding eclipses solar eclipses from Earth – although *Gaia* will perform one maneuver to avoid Earth's core shadow. They also provide a high observing efficiency, as the Sun, Earth and Moon are easily kept out of the telescope's field of view. Due to this configuration, *Gaia* is actually able to integrate its antenna into its solar shield, as Earth and the Sun are within the same direction relative to L_2. Lastly, and as pointed out above, the radiation environment at L_2 is relatively benign – while not within the protection of Earth's magnetic field as for a low earth orbit, an L_2 orbit does avoid passages through Earth's radiation belts as experienced by missions like *XMM-Newton* (Gastaldello et al., 2017) with eccentric orbits around Earth.

Given the high interest in the Sun-Earth L_2 point in the coming years, any knowledge of the

effect of its radiation environment on astronomical missions will be very valuable. *Gaia*, with its unique FPA, provides a great laboratory for the investigation of these effects. While we have seen that the long-term effects of cosmic rays on *Gaia* are already being analyzed, there has been little analysis on the spurious signal caused by the same particles. In the next chapters, we will develop algorithms to extract exactly this signal from selected *Gaia* datasets.

Chapter 3

Dataset Generation

This chapter will describe the creation of a catalog of cosmic ray events detected in *Gaia* observations. After establishing additional CCD terminology and describing our source observations, we will explain the two steps in creating this catalog, namely the extraction of cosmic ray tracks in images (Sec. 3.3) and the processing of these tracks to obtain flux measurements and individual event properties (Sec. 3.4). Both processing steps will be validated using simulations of particle tracks in CCD images.

For the track extraction, we will use event detection algorithms tailored to the respective detector type and source data product, separating the main observational data in each dataset from cosmic rays by using our knowledge of the former. All our algorithms expand on existing algorithms for cosmic ray detection in CCD observations. Taking these algorithms, we then develop a first extraction pipeline to produce for every observation a list of objects that have been recognized as cosmic ray tracks.

For our post-processing pipeline, we will develop algorithms to further refine our raw event lists, adding information such as track lengths and orientation on the FPA, as well as the flux measured in each observation. We will then arrive at a final data product, which will be examined in Chapter 4.

3.1 *Gaia* Conventions

The following set of definitions and conventions are simply a subset of those (thoroughly) defined by Bastian (2004). We have adopted those referring to CCD characteristics and relevant for this thesis. Appendix A also contains a list of *Gaia* Acronyms defined in the introduction and used below.

3.1.1 CCD Definitions

• A 'pixel' is the elementary charge generation and storage element in the light-sensitive area of the CCD.

• A 'column' is the set of all pixels having the same across-scan coordinate.

• A 'line' is the set of all pixels having the same along-scan coordinate.

• The 'summing register' is a special pixel line following the light-sensitive pixels. It is used to combine (add or bin) the charges from several lines into one.

• The ‘read-out register’ is the special pixel line which is used to transfer the accumulated charges from the CCD chip into the read-out amplifier (and thus further into the further amplification and digitization electronics).

• The ‘read-out amplifier’ is the electronic circuit at the end of the read-out register where the registration and pre-amplification of the photoelectric charges takes place.

• The ‘time delay integration’ mode (TDI mode) consists of gradually shifting the photoelectric charges from “left” to “right” — and eventually into the read-out register — to follow moving optical images over the light-sensitive area.

• ‘Gates’ are special lines within the light-sensitive area. If activated they act like summing registers, holding up charges, preventing them from moving along scan in spite of the TDI clocking. This causes a compression (summing) of the already accumulated TDI images into a single line, and the creation of a new “blank” empty space “in front of” this line.

Figure 3.1 summarizes these definitions.

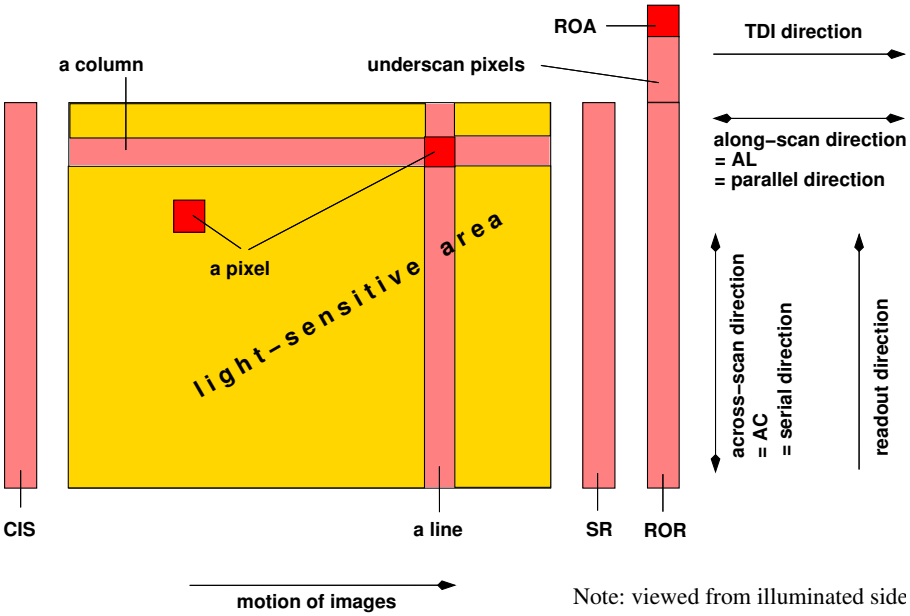

Figure 3.1: CCD-related notations, taken from Bastian (2004).

3.1.2 Focal Plane Reference System

Figure 3.2 shows the reference system used for the *Gaia* Focal Plan Array.

3.2 Data Sources

For the analysis of the cosmic rays in *Gaia* CCDs we have used a number of different *engineering* datasets, namely:

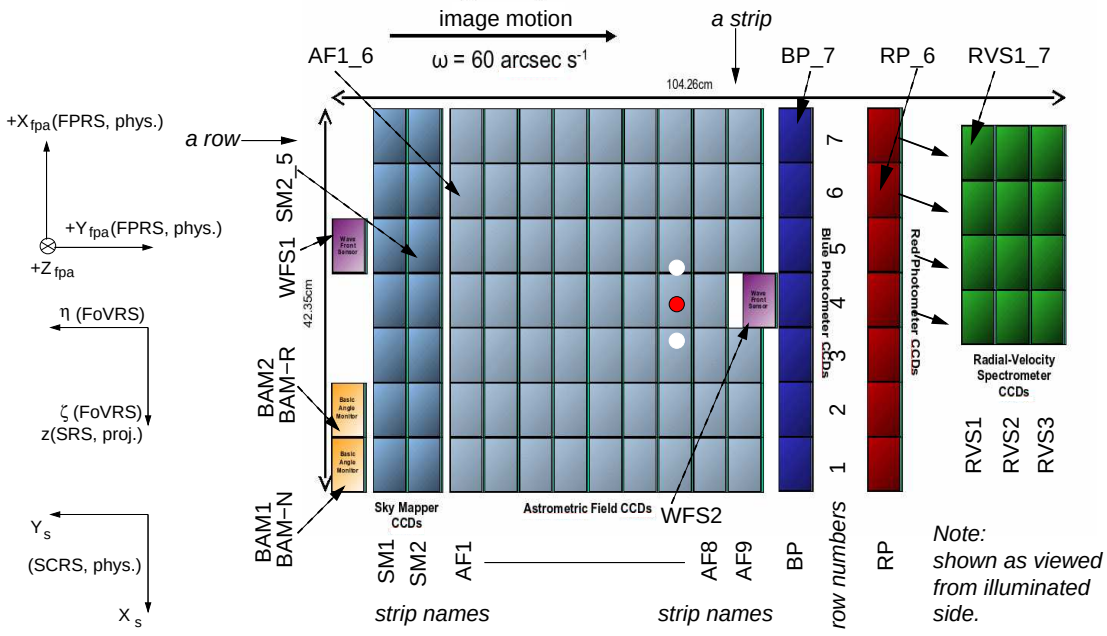

Figure 3.2: The Focal-Plane Reference System, taken from Bastian (2004).

- Sky Mapper images down linked via the Service Interface Function - from here on shortened to SM-SIF. These images are recorded fully in TDI mode and contain objects of interest such as planets, comets, dense stellar fields such as globular clusters or the Galactic center as well as, most frequently, very bright stars that drive the CCDs into saturation.

- Nominal BAM observations, from here on shortened to BAM-OBS. These images consist of two readout windows roughly $1 \times 1\,\mathrm{cm}$ in size located on one chip, which continuously observe the interference pattern of the BAM in staring mode.

- SIF BAM observations, shortened to BAM-SIF. These images record the same AC region as the BAM-OBS source images, but span the width of the entire chip in AL. They thus contain off-pattern regions with a very weak background. This dataset has been previously analyzed for cosmics by Kohley (2015).

3.3 Feature Extraction

The goal of the feature extraction step is to collect all the objects recognized as cosmic ray tracks from the different datasets into a source-independent dataset for the post-processing. To that extent, we have defined an intermediary dataset named TrackObs (short for track observation), which collects necessary metadata on the source observation and contains a list of all identified objects.

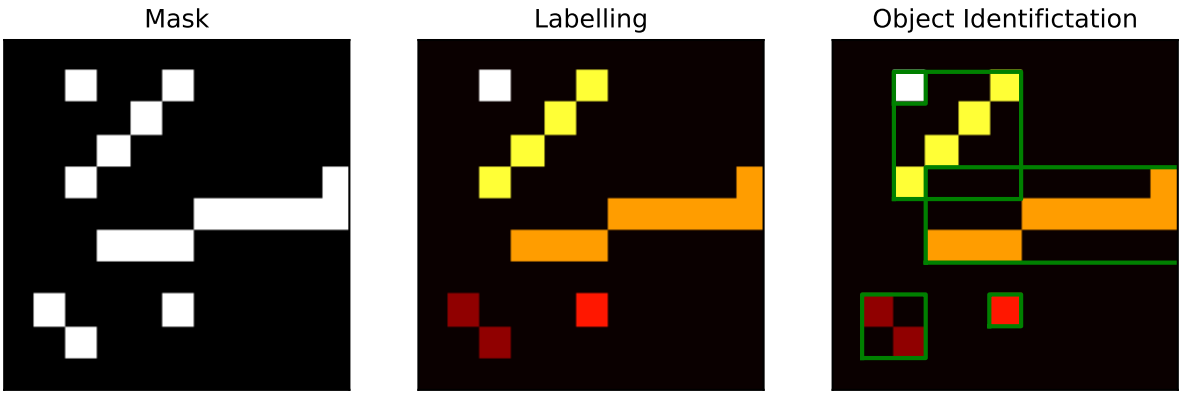

Figure 3.3: Identification of individual connected objects from a cosmic ray mask. The boolean mask (left panel) is used to calculate an integer array for all 8-connected pixels, which are labeled with a unique integer per object (middle panel). Objects are then identified by their labels as rectangular image sections around all pixels with a common label (green boxes in right panel).

The metadata saved in this dataset includes:

- The type of source observation (SM-SIF, BAM-OBS, BAM-SIF)
- The acquisition time in OBMT
- The source image dimension (in AL and AC)
- The number of pixels not used for extracting cosmics (for the calculation of the exposed area)
- The sample binning, in AL and AC
- The CCD gain
- The chip location on the FPA (row and FoV)

The output of all of the following algorithms are three two-dimensional arrays of the same size as the input image: A boolean mask array set to True for all pixels identified as cosmics, a signal array consisting of the original image minus the non-cosmic "background", and an array of the uncertainty of this signal array. As the conversion of these arrays into cosmic ray tracks is the same in all of the following algorithms, we will explain the process here.

First, individual objects are identified from the mask. This process is shown in Figure 3.3. From the boolean mask, a labeling algorithm from the `scipy` Python distribution is used to assign the same integer value to all neighboring pixels set to True – in this case, if they are horizontally, vertically or diagonally adjacent. The labeled array is then used by a `scipy` object finding algorithm to identify the bounding boxes of all pixels of the same label.

Each TrackObs then contains an array whose rows represent information on one of the objects identified in the above steps. For each track, it lists:

- The AL and AC lengths of the bounding box
- The location of the track, encoded as the lowest AL and AC value in its bounding box
- The sub-image of the track from the signal array, encoded in ADU. Note that this only includes those pixels inside the bounding box with the corresponding label - in the right panel of Fig. 3.3, the image of the 4×4 diagonal track in the upper left does not include the single pixel track in

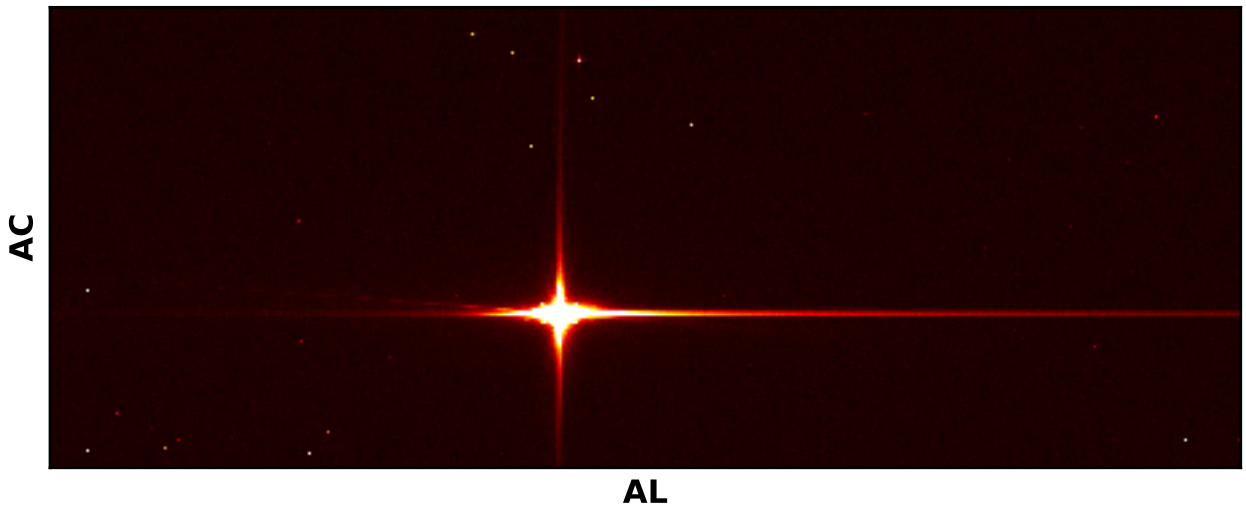

Figure 3.4: An example of a SM-SIF source image. Axis orientation is the standard *Gaia* convention, with the serial register to the right and readout to the upper right corner. The aspect ratio has not been corrected for pixel geometry and binning.

its bounding box, which has a different label.

- The sum of signal values of the track in electrons, corresponding to the total measured ionizing energy.
- The uncertainty of the total ionizing energy, being the square root of the sum of the squares of the individual pixel uncertainties.

Each of the following algorithms produces such TrackObs objects, which are saved intermediately as FITS files.

3.3.1 SM-SIF: Laplacian Edge Detection

Figure 3.4 demonstrates a typical image in the SM-SIF dataset. The image contains a bright star object with a PSF that consists of long diffraction spikes and a saturated core. Less bright stars and what appear to be cosmic ray tracks can be recognized by bare eye.

To automate the detection of cosmic ray tracks in these images, they must be successfully separated from the imaged astronomical objects. Such algorithms, usually used to remove unwanted cosmic rays, have been developed for earlier ground- and space-based observatories and can be used in to our advantage. For this dataset, we decided to utilize the L.A. Cosmic algorithm described by van Dokkum (2001). Briefly summarized, this algorithm utilizes a variation of Laplacian edge detection to discriminate cosmic ray tracks from stars by their sharp edges, which separates them from the smoother PSFs of stars.

In more detail, the algorithm first convolves a subsampled version of the original image with a derivative filter, which assigns high values to sharp edges. The resulting image is compared with a noise image, calculated by a 5×5 median filter of the image and including the CCD readout noise. Pixels with a signal-to-noise-ratio above a high threshold are then selected as first candidates for noise pixels, after which a lower threshold is applied to neighboring pixels. The identified pixels are then masked and the original image is cleaned, replacing the cosmic ray

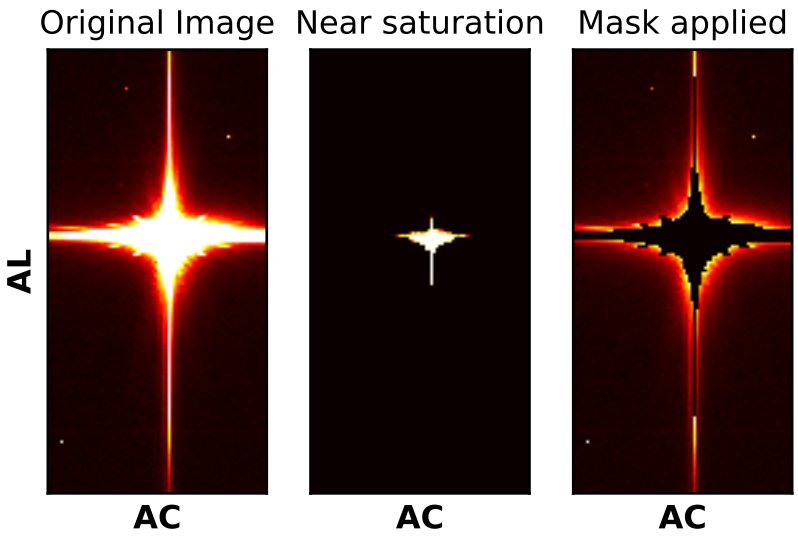

Figure 3.5: Bright stars in SM-SIF and how they are masked. *Left:* The appearance of the bright star from Fig. 3.4. *Middle:* The left panel after applying a high threshold. The bright pixels are fully saturated and show a sharp charge transfer pattern. *Right:* The left panel after applying bright star filtering - the core and a large part of the diffraction spikes are masked.

pixels with the median or mean of the surrounding, unmasked pixels. This procedure, starting from the convolution, is applied iteratively until either no more pixels are identified or the maximum number of iterations has been reached.

This analysis utilizes a Python implementation of the L.A. Cosmic algorithm called Astro-SCRAPPY (McCully, 2015) for cosmic ray identification.

First attempts at simply applying Astro-SCRAPPY to images like the one in Fig. 3.4 revealed that the bright stars in most of the SM-SIF images were still falsely detected as cosmics. The reason for this is their saturation of the detector – see especially the middle panel of Figure 3.5. The bright star, as it saturates the detector, causes a strong blooming and smearing, saturating even the pixels read in after those exposed to the bright stars (the image read out direction is to the top). As the panel shows, the resulting pattern has a very sharp gradient, which is picked up by the Laplacian filter and mis-identified as a cosmic.

To eliminate these bright star cores and mask their extended field, in which cosmics will disappear under the shot noise of the star, we apply a simple algorithm before extracting cosmics. Its steps are:

1. Object finding: Construct a mask set to 1 for every pixel above a low threshold and apply object labeling to this mask. This step essentially catches all stars and cosmics.

2. Saturated object identification: Of all objects, select only those that contain at least one pixel at a value of 65535 ADU, the maximum signal value of the 16-bit image.

3. Masking: Add all the objects identified in the previous steps to a mask (set to 1 for invalid pixels). This mask can be forwarded to Astro-SCRAPPY, which supports masked regions and does not use them for cosmic identification.

The results of this algorithm can be seen in the right panel of Fig. 3.5, where all pixels belonging to the bright star are set to zero. There still remain some parts of the bright star's PSF - these,

however, are very close to the bias level and decay smoothly, thus causing no issues.

Using the bright star removal, we then constructed the following algorithm to extract cosmics from SM-SIF observations:

1. Read in the image and construct the bright star mask.
2. Subtract the AL-dependent bias and apply the gain-scale, as L.A. Cosmic requires an image in units of electrons to calculate the Poisson noise.
3. Apply L.A. Cosmic, which returns the cosmic ray mask and a cleaned image. The values of the cleaned image are calculated by taking the mean of the surrounding, non-masked pixels in a 5×5 pixel area, i.e. for a pixel located at (AL, AC), the cleaned value is

$$\text{Clean}\,(AL, AC) = \left(\sum_{\substack{AL-2 \leq i \geq AL+2 \\ AC-2 \leq j \geq AC+2}}^{\text{mask=False}} \text{Source}\,(i, j) \right) \Bigg/ \left(\sum_{\substack{AL-2 \leq i \geq AL+2 \\ AC-2 \leq j \geq AC+2}}^{\text{mask=False}} 1 \right) \tag{3.1}$$

4. Calculate the signal array as $\text{Signal}\,(AL, AC) = \text{Source}\,(AL, AC) - \text{Clean}\,(AL, AC)$
5. Calculate the uncertainty array as the square root of the variance of the signal array,

$$Var\,(AL, AC) = \text{Source}\,(AL, AC) + \sigma_{\text{rn}}^2 + \sum_{\substack{AL-2 \leq i \geq AL+2 \\ AC-2 \leq j \geq AC+2}}^{\text{mask=False}} \frac{\text{Source}\,(i, j) + \sigma_{\text{rn}}^2}{N_{\text{mean}}\,(AL, AC)}, \tag{3.2}$$

   with σ_{rn}^2 denoting the pixel read noise and $N_{\text{mean}}\,(AL, AC)$ denoting the number of pixels used to calculate the mean for cleaning this pixel. As one can see from the equation, the noise of the source image has been assumed to be Poissonian shot noise and a known read noise.
6. Extract tracks from the mask, signal and uncertainty images and save them as a TrackObs, as described above.

The parameters used for the L.A. Cosmic algorithm were first selected manually, by applying the extraction algorithm to individual images and viewing the output. Selection criteria were that no stars should be misidentified as cosmic ray tracks and that cosmic ray tracks should be complete, meaning that a single, long track should result in exactly one identified object.

To verify and further tune the extraction algorithm with regards to the detection efficiency and measurement accuracy, it was necessary to have known input data with which to compare the measured output. To that extent, we utilized a previously developed CCD cosmic ray events simulator called T.A.R.S. (Tools for Astronomical Radiation Simulations) developed at ESTEC (Garcia et al., 2018). The tool simulates the energy deposition of a cosmic ray in a CCD detector along with the charge collection to produce simulated CCD images. The first implementation of the tool was built to simulate *Gaia* images and was thus suited for this activity.

To test the extraction algorithm, we first prepared an SM observation by cleaning it with L.A. Cosmic, removing any existing cosmics that would be detected by our algorithm. For the source image, we selected a large image without any saturated stars, as these cosmics could not be detected there in any case and we were more interested in possible confusions wit 'normal' stars.

We then generated cosmic ray tracks on the image, saving the locations and deposited energies for every simulated cosmic. Afterwards, we ran the extraction algorithm from above and analyzed

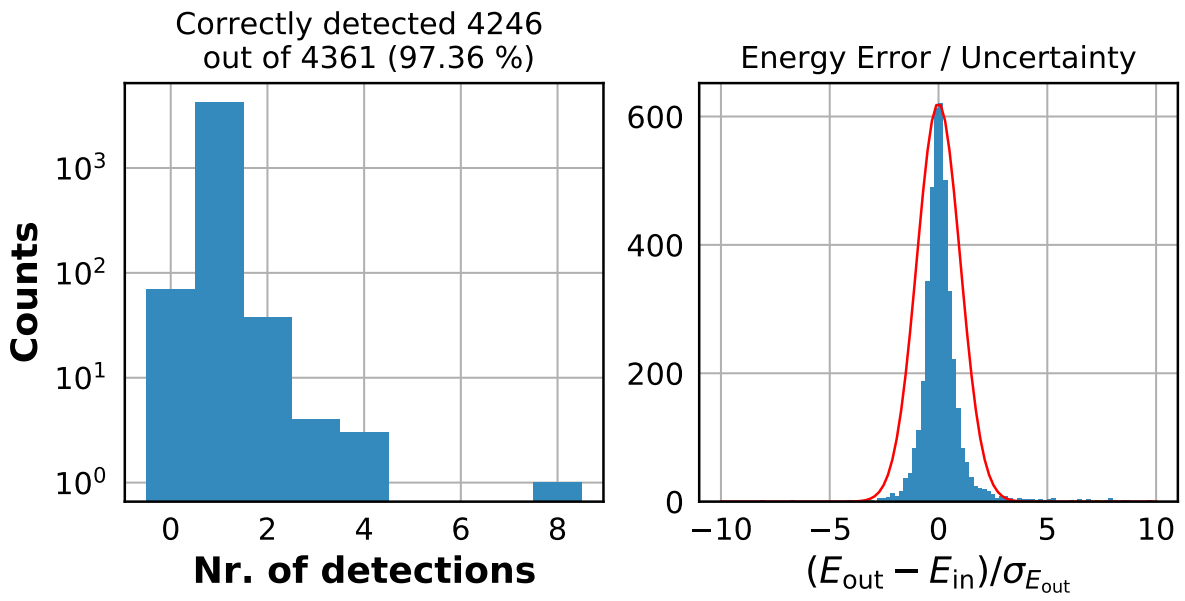

Figure 3.6: Figures of merit for the SM-SIF extraction. *Left:* Histogram of the number of associated track detections per input cosmic. A value of 0 is a non-detection, a value of 1 is a correct detection, a value of >1 means a single cosmic has resulted in multiple detections. *Right:* Histogram of the difference between measured and input track energy per cosmic, normalized by the calculated uncertainty. A Gaussian with a standard deviation of 1 is plotted in red.

the results by associating each simulated track with the tracks recovered in its image location. Figure 3.6 shows two figures of merit for the extraction algorithm: The detection efficiency and the error of the extracted energies with respect to the calculated uncertainty.

The detection efficiency (left panel of Fig. 3.6) shows the number of detected tracks per input track – a value of 1 being a correct detection, a value of 0 being a non-detection and a value greater than 1 implying that parts of the track could not be identified, leading to multiple detections. The overall number of correctly detected events is greater than 97 %.

The error in the extracted energies is shown in the left panel of Fig. 3.6, which plots the difference between the measured track energy and the ionizing energy dumped by the simulated cosmic on the detector. For each track, this value is normalized by the uncertainty of the measured energy. A comparison of the resulting histogram with a Gaussian with a standard deviation of 1 shows that the energy measurements are correct within their estimated errors.

3.3.2 BAM-OBS: Boxcar filtering / Stacking

Figure 3.7 shows a series of observations from FoV 1 of the BAM. The three images were recorded in series (left to right) with an exposure time of about 23 seconds each. It is visibly apparent that the BAM patterns do not significantly differ between single observations, yet all three images contain pixels deviating from the pattern that only exist in one given image. These spurious pixels are a clear sign of cosmic rays.

Figure 3.8 further demonstrates that the interference pattern does not vary aside from Poissonian noise between the three images. It also shows why a simple application of the L.A. Cosmic algorithm to this dataset will immediately fail: The interference patterns themselves are very

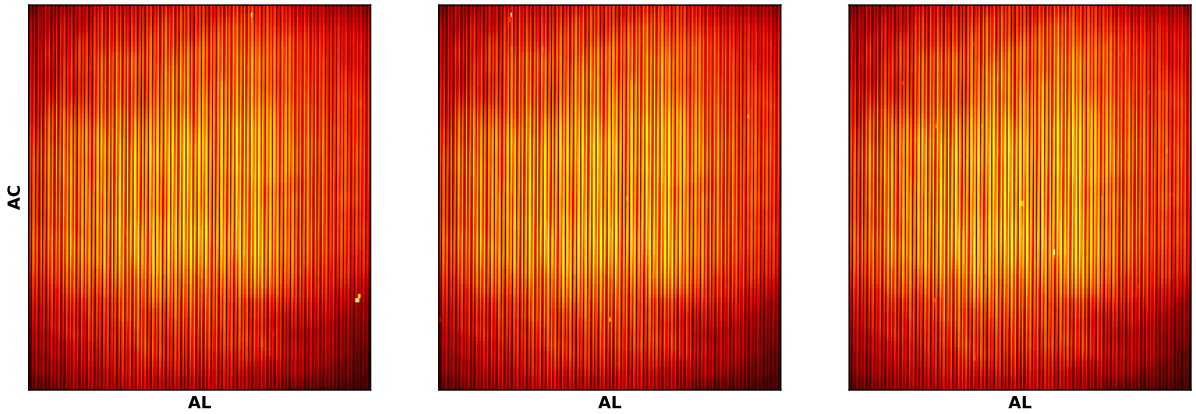

Figure 3.7: A series of three BamObservations from FoV 1. The dimensions have been rescaled to the physical dimension of the CCD – each image pixel represents a $10 \times 120\,\mu m$ (AL $\times$ AC) sample. Individual pixels that deviate from the patterns can be recognized as cosmic ray tracks.

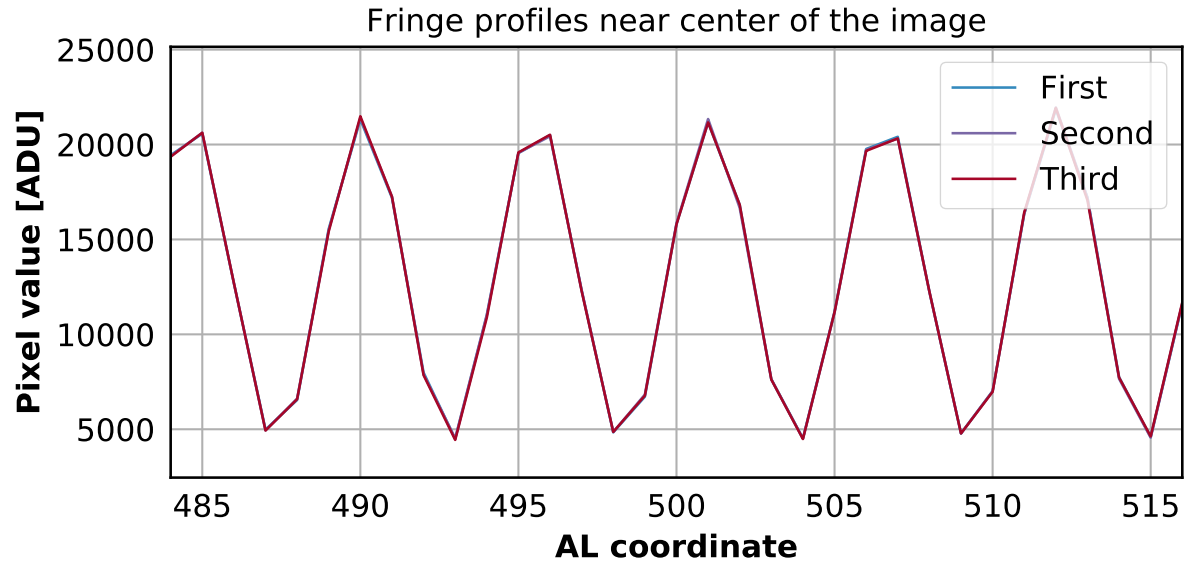

Figure 3.8: The ADU values of the three patterns in Fig. 3.7 plotted along the center of the images in AC across a narrow AL region in the center. The interference pattern is very sharp, with a period of about 5 pixels in AL. The fringes of all three images overlap very closely.

sharp, with a peak-to-trough distance of about 2 to 3 pixels. The algorithm thus triggers detects the patterns as cosmic ray tracks and can not separate it from real cosmics.

For our track extraction algorithm, we exploited the fact that the interference pattern is relatively static. In astronomy, multiple exposures of the same object (assuming constant luminosity) are often used to reject the spurious high pixel values caused by cosmic rays – a similar algorithm is used to reject cosmics in BamObservations when analyzing the pattern. In our case, we can simply do the reverse, and accept pixels that vary significantly stronger than the inherent counting and readout noise as the tracks of cosmic rays.

The concrete algorithm assumes as an input a time-ordered series of BamObservations from a

single FoV and operates on a range of observations, which we refer to as a BoxCar. To create a good estimate of the pattern across a period of time where it does not significantly vary, we chose to use a total of 7 images at once - a central image for cosmic ray extraction and the three images recorded immediately before and after. The extraction algorithm works as follows:

1. Construct the BoxCar: Read the first 7 BamObservations – applying the electron conversion gain – into a three dimensional array with the indices t, AL and AC - with $t \in [1, \cdots, 7]$ ($t = 4$ being the central observation), and AL and AC denoting the image dimensions.

2. Sigma-clipping: Compute the median and standard deviation across time for each pixel coordinate and mark all the pixels whose difference to the median exceeds a chosen threshold - these are likely cosmics, and will not be used to calculate the pattern.

3. Calculate a two-dimensional image array of the pattern, by taking the mean across time without using the sigma-clipped pixels, e.g.

$$\text{Pattern}\,(AL, AC) = \left(\sum_{t \text{ not clipped}} \text{BoxCar}\,(t, AL, AC) \right) \Big/ \left(\sum_{t \text{ not clipped}} 1 \right). \tag{3.3}$$

4. Calculate the signal array by subtracting the Pattern from the central array in the BoxCar, e.g.

$$\text{Signal}\,(AL, AC) = \text{BoxCar}\,(t = 4, AL, AC) - \text{Pattern}\,(AL, AC)\,. \tag{3.4}$$

5. Calculate the uncertainty array as the square root of the variance of the signal array via

$$Var\,(AL, AC) = \text{BoxCar}\,(t = 4, AL, AC) + \sigma_{\text{rn}}^2 + \sum_{t \text{ not clipped}} \frac{\text{Boxcar}\,(t, AL, AC) + \sigma_{\text{rn}}^2}{N_{\text{mean}}\,(AL, AC)}, \tag{3.5}$$

   with σ_{rn}^2 denoting the pixel read noise, and $N_{\text{mean}}\,(AL, AC)$ denoting the number of pixels in the BoxCar that have not been rejected by sigma clipping at this (AL, AC) coordinate. As one can see from the equation, the noise of the BamObservations has been assumed to be Poissonian noise and read noise.

6. Create the cosmic mask: Divide the signal array by the uncertainty array and create the boolean mask array, set to True where the signal/uncertainty ratio is greater than a threshold f. Due to the strong photon background, some cosmic pixels are missed in this step. We attempt to mitigate this by investigating all the pixels that neighbor the previously masked pixels, found via binary dilation, and applying for them a signal/uncertainty threshold of $r_{\text{Neighbor}} \cdot f$, adding the pixels that satisfy this condition to the mask as well.

7. Apply a track connection algorithm: Even after the previous step, visually apparent long cosmic ray tracks still remain separated - refer to the left panel of Figure 3.9 for an illustration. Tracks that are oriented in the AL direction see a strongly variable photon background, seen as fluctuations in the uncertainty array. Any cosmic ray signal on and inteference fringe peak is thus less likely to be detected by the thresholding of before. Especially towards the center of the image, where the pattern amplitude is very high, this leads to a single, long cosmic being detected as multiple short cosmics in the troughs of the interference pattern, which eventually leads to an overestimation of the cosmic ray rate.

   In an attempt to correct for this track separation, we implemented a track connection algorithm: We first apply to the mask an 8-connected binary dilation followed by a

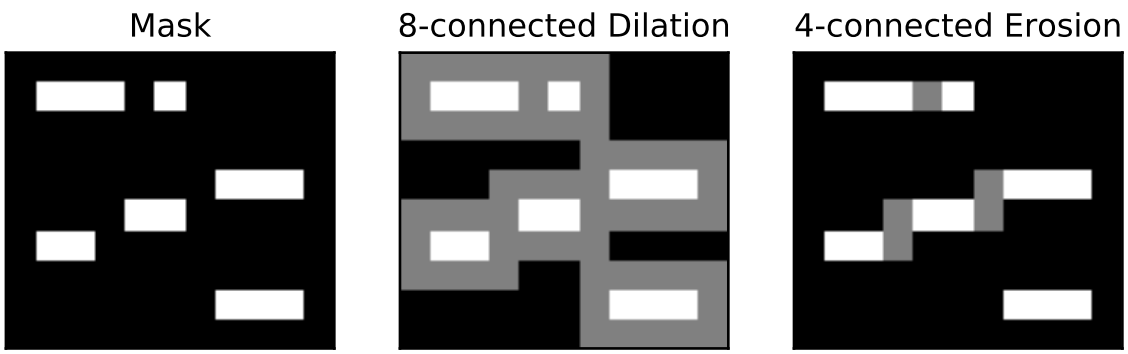

Figure 3.9: Illustration of the track connection algorithm used for the BAM dataset. *Left:* An example of a cosmic ray mask where tracks oriented in the AL direction have not been fully identified. *Middle:* Application of 8-connected binary dilation to the mask - the added pixels are shown in gray. *Right:* Additional application of 4-connected binary erosion, shown in the gray pixels, which are examined by the connection algorithm.

4-connected binary erosion (this is a variant on binary closing, which uses the same structuring elements for the dilation and erosion instead), illustrated in the middle and right panels of Fig. 3.9. As the figure shows, this marks several pixels of interest that may connect the separated objects.

We then examine each of the newly merged tracks, which are identified by the standard labeling algorithm. For each of the tracks, we first calculate the mean of the previously identified signal pixels of this track, m_{Object}. Assuming that a cosmic ray creating a long track should have a constant energy deposition per path length, we examine each of the candidate pixels (at the location (AL, AC)), checking for the condition

$$|Signal\,(AL, AC) - m_{\mathrm{Object}}| > cfac * \sqrt{Var\,(AL, AC)}, \tag{3.6}$$

with $cfac$ being an algorithm parameter. The above equation checks whether the signal value of the candidate pixel is sufficiently close to the value of the other pixels in this object. If a pixel satisfies the condition, it is added to the pixel mask.

8. Extract tracks from the mask, signal and uncertainty images and save them as a TrackObs, as in SM-SIF and described above.

9. Update the BoxCar: Read in the next BamObservation and replace the oldest pattern in the BoxCar with it – the BoxCar is utilized as a FIFO, in this case. We then update the central pixel index and repeat starting step 2 until all BamObservations have been processed.

As we did for the SM-SIF extraction, we also tested the BAM-OBS extraction algorithm using the T.A.R.S. package. In the case of BAM-OBS, we first created a series of fake BAM patterns by calculating a running median over a set of 100 successive BamObservations. Concretely, we took for every observation the four preceding and four next observation and calculated the median image of these observations. Afterwards, we added Poissonian counting noise to each image.

We then added simulated cosmic ray tracks to all images and ran the extraction algorithm over the list of observations. As in the SM-SIF verification, we associated each input track with the detected tracks in its image location. As before, Figure 3.10 shows the detection efficiency and

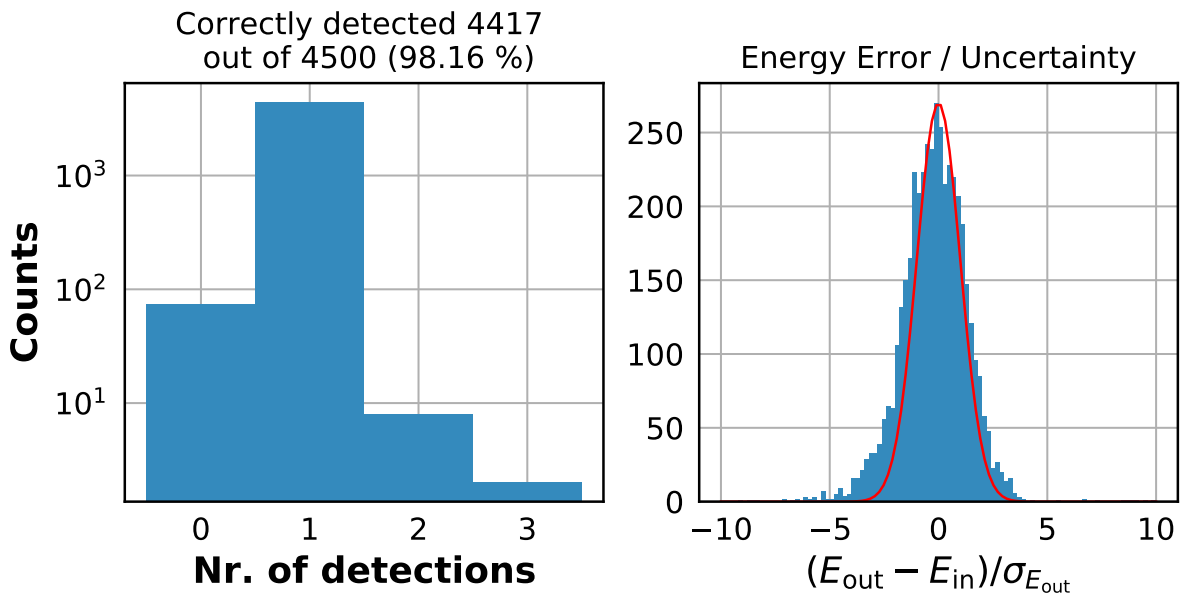

Figure 3.10: Figures of merit for the BAM-OBS extraction, as in Fig. 3.6.

normed energy error for the BAM-OBS extraction, once again returning consistent values for both. Note that these plots show results for FoV 2, whose interference pattern has a higher intensity and thus noise.

To justify the use of the connection algorithm (step 7 above), Fig. 3.11 shows the figures of merit for the same input data as Fig. 3.10 when the connection algorithm is not used. While the measured energies don't differ significantly, the number of input tracks recognized as multiple output tracks is lowered by the connection algorithm.

3.3.3 BAM-SIF: Thresholding

Figure 3.12 depicts an example of a BAM-SIF image used in this extraction. These images both contain the interference pattern in the BAM-OBS images as well as off-pattern regions showing the TDI footprint of the pattern, which is only AC-dependent. These images are much less frequently sampled than the BAM-OBS images – usually a handful of images twice per week – which is why they are not very useful for the purpose of particle monitoring. However, the off-pattern regions offer a good opportunity to extract cosmics from the BAM chip with a much lower and simpler background than that of BAM-OBS, allowing us to examine the effect the pattern has on the above extraction.

As this dataset is very attractive for cosmic ray extraction, it has been used before for cosmic ray studies (Kohley, 2015). This algorithm builds on this previous extraction, merging it into the TrackObs-based approach utilized in this thesis.

For the extraction of cosmics, we utilize the two regions outlined in blue and green boxes in Fig. 3.12. A smaller region in AC has been selected for the FoV 1 region - the ignored region has shown a high stray light contamination, which generates false positive cosmic ray track detections.

The extraction algorithm for this dataset is then (for each region separately):

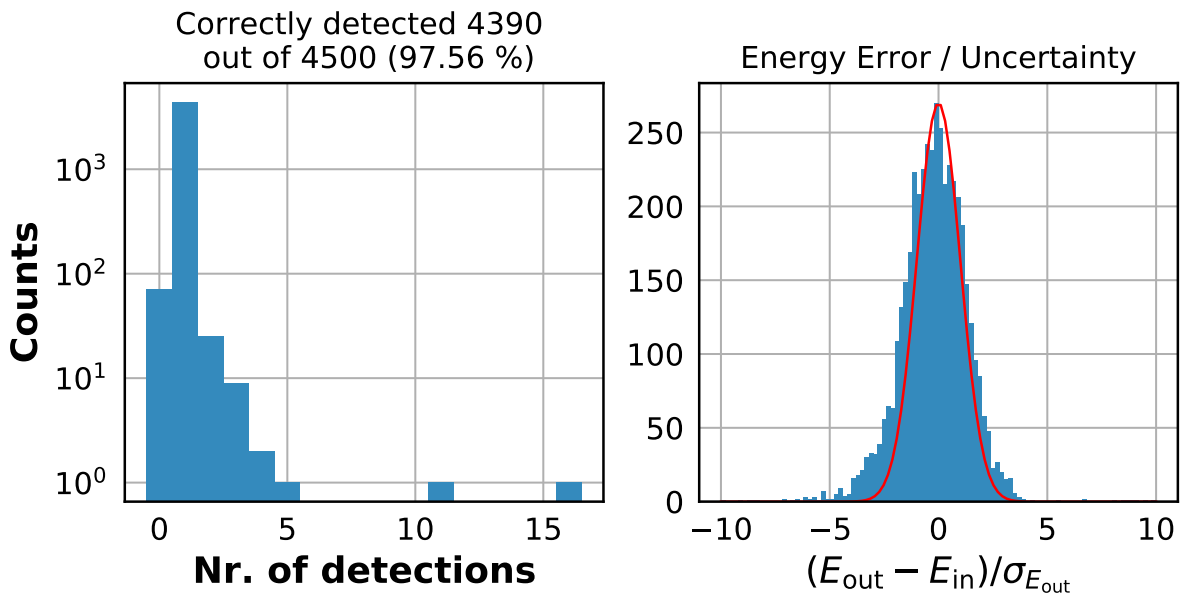

Figure 3.11: Figures of merit for the BAM-OBS extraction without the track connection algorithm. Compared to Fig. 3.10, individual cosmics are more likely to be identified as multiple tracks.

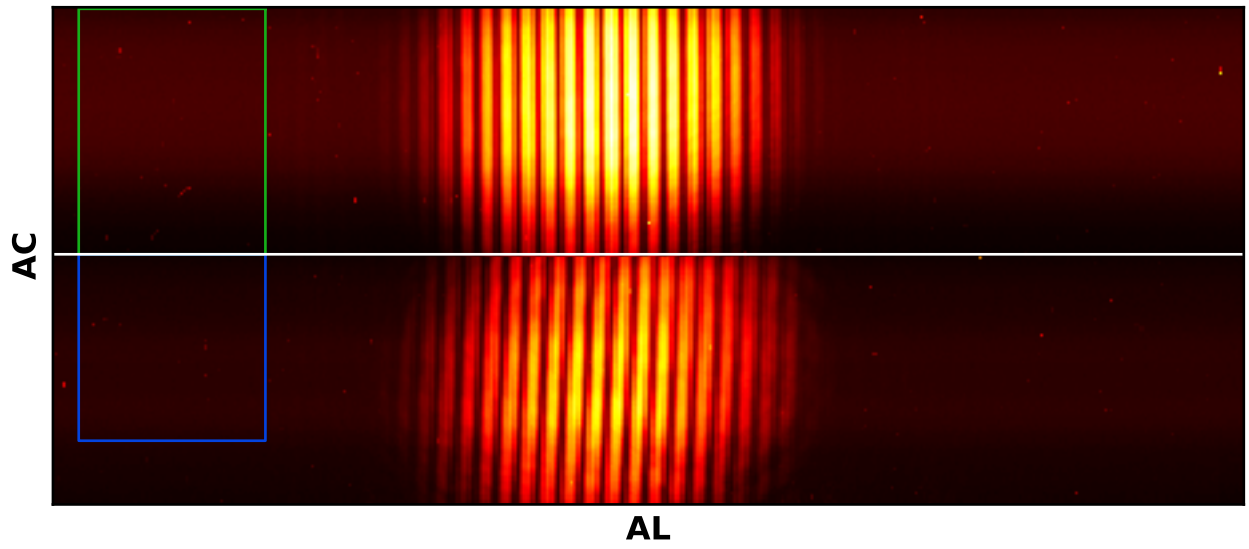

Figure 3.12: An example of a BAM-SIF source image, which has been rescaled to the physical CCD dimensions. The top half of the image shows the AC region of FoV 2, the bottom half that of FoV 1. The off-pattern regions in green and blue boxes are used for cosmic extraction.

1. Read in the image and apply the gain scale.

2. Determine the AC-dependent TDI background: Take the 99 columns at the highest AL coordinates (to the left in Fig. 3.12) and remove the outliers by discarding the highest and lowest 25 % of pixel values per column. Then, calculate the mean and standard deviation of the remaining image pixels for each line. The output are two one-dimensional arrays

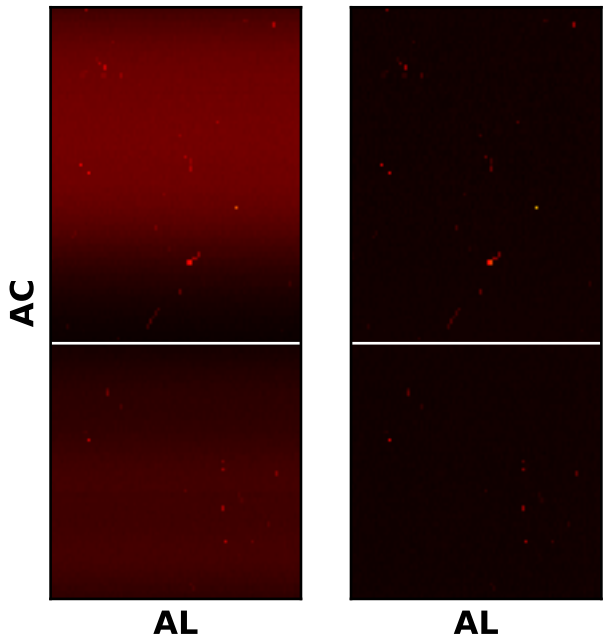

Figure 3.13: *Left:* The two extraction regions from Fig. 3.12. *Right:* The same image with the TDI background removed, leaving only cosmic ray tracks.

representing the AC-dependent TDI background and its standard deviation. The removal of the TDI background is demonstrated in Figure 3.13.

3. Calculate the signal and variance arrays as

$$Signal\,(AL, AC) = Source\,(AL, AC) - Background\,(AC) \tag{3.7}$$

and

$$Var\,(AL, AC) = Source\,(AL, AC) + \sigma^2_{\mathrm{rn}} + \sigma^2_{\mathrm{Background}}\,(AC)\,, \tag{3.8}$$

with σ_{rn} being the read noise and once again assuming Poisson noise in the source array. The uncertainty array is then the square root of the variance array.

4. Construct the mask array in exactly the same way as for BAM-OBS, including the track connection. While the latter should not be necessary here, we want to have as similar as possible algorithms for BAM-OBS and BAM-SIF, to see the effect of the pattern.

5. Extract tracks from the mask, signal and uncertainty images and save them as a TrackObs, as in the algorithms above.

All steps until the calculation of the variance are the same as those used by Kohley (2015), which only returned the signal images.

As in both previous algorithms, we once again verified the BAM-SIF extraction against simulated cosmics. In this case, a fake TDI background was obtained by removing outliers from a BAM-SIF observation. A background image is then randomly sampled line by line from the extracted background. Afterwards, simulated cosmic ray tracks are added on top of the produced image and extracted via the BAM-SIF algorithm. The figures of merit obtained in the same way as before are plotted in Figure 3.14, showing a very good detection efficiency and energy errors within the bounds expected from the calculated uncertainties.

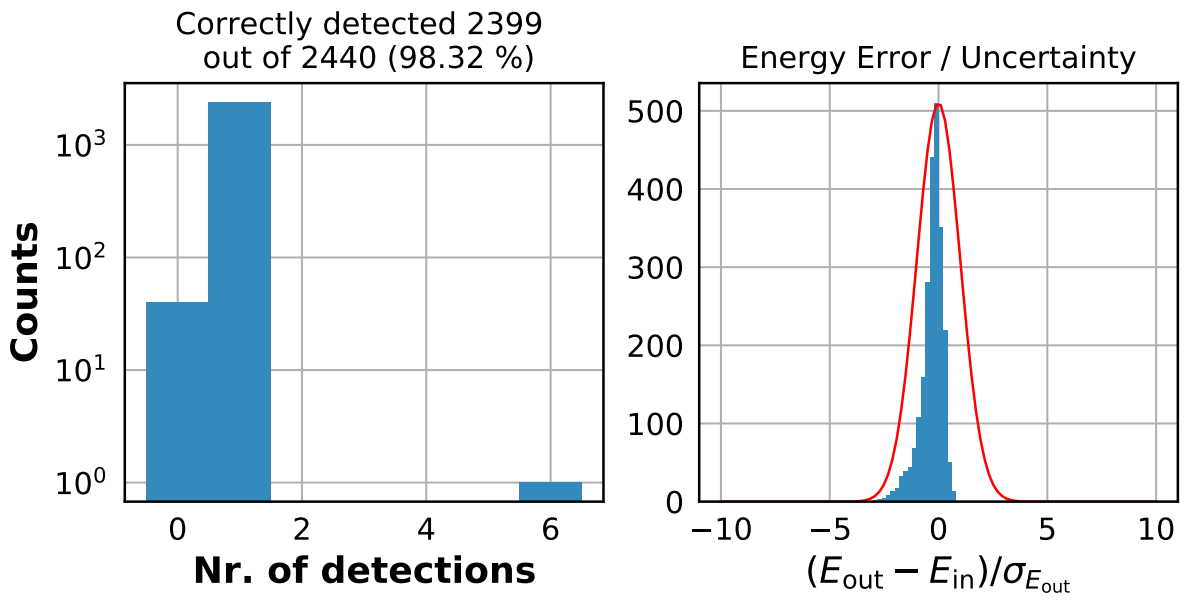

Figure 3.14: Figures of merit for the BAM-SIF extraction, as in Fig. 3.6.

3.3.4 Extraction Pipelines

Having specified the extraction of cosmic ray tracks from the images themselves, we now describe the extraction pipelines used to systematically retrieve the image data files from the *Gaia* Main Database in order to produce the respective TrackObs files.

While the pipeline is implemented in Apache Spark, we will describe the pipeline independently of the utilized software.

SM-SIF and BAM-SIF

Input data for the SM-SIF and BAM-SIF are both saved in in FITS files, each containing the data of a single observation. All input files are stored in a SIF directory, in individual folders sorted by date (format: yyyy-mm-dd). As the analysis of one observation is fully independent, this extraction is very easy to parallelize.

For the SM-SIF and BAM-SIF dataset respectively, we use the extraction algorithms listed above to obtain TrackObs from images. The steps of the extraction pipeline around the extraction are:

1. Group all files by their date
2. For each date `yyyy-mm-dd`:
   - 2.1. Create a buffer for the TrackObs
   - 2.2. For each file:
     - 2.2.1. Extract a TrackObs from the image using algorithms from Sec. 3.3.1/3.3.3
     - 2.2.2. Add the TrackObs to the buffer
   - 2.3. Write all the TrackObs in the buffer to a FITS file with the directory structure `yyyy/mm/dd/[source]_OBMT_START_[obmt of first TrackObs].fits`, with `[source]` being `SM-SIF` or `BAM-SIF`, respectively.

Step 2 and all sub steps within are completely independent for each day and can as such very easily be parallelized.

BAM-OBS

The input data for the BAM-OBS dataset is saved in compressed gbin files, each containing normally around 200 BamObservation objects of alternating FoV. The BAM-OBS extraction pipeline – see the flowchart in Fig. 3.15 – is designed to take into account that the algorithm requires the utilization of a BoxCar moving over a continuous list of BamObservations. Parallelization is achieved by sorting the gbin files by the acquisition time of their BamObservations and dividing this sequence into individual chunks, to be handled separately. The extracted TrackObs are saved once again in FITS files, in the same directory structure as in the SIF extraction above.

Note that for the processing of each file group, a small overlap to the next file group needs to be considered in order to process all the BamObservations: For two sequential groups of BamObservations A and B, the last observation in A needs to use the first three observations in B to fill the BoxCar for its extraction, and analogously for extracting the first observations in B.

3.4 Post-Processing

For the final data product described in Appendix B.1, we derive additional data from the raw extracted tracks in a TrackObs. The algorithms for deriving these are outlined in this section.

3.4.1 Observed Flux

One of the first – and most simple – data products that can be derived from a TrackObs is the on-chip rate of particles measured per observation. In order to provide a simple measure of this rate useful in estimating the resulting background signal, we restrict ourselves to a simple flux definition: Given an exposed CCD area A_{exp} and exposure time T_{exp}, the flux is simply calculated as

$$F = \frac{\text{Counts}}{A_{\text{exp}} \cdot T_{\text{exp}}}. \tag{3.9}$$

This is opposed to the more complex differential flux as used by Sullivan (1971) and most dedicated particle monitors. Another reason for restricting ourselves to this simple on-chip rate is the complexity of the shielding environment of *Gaia*'s FPA shown in Fig. 2.6, which would require extended modeling of the propagation of particles to the FPA to calculate the needed conversion factors.

In the following, we determine A_{exp} and T_{exp} for SM and BAM observations, which is not trivial due to the use of TDI (and in the latter case, staring) observations and the size of the used AL readout windows relative to the physical CCD size.

For our calculations: A *Gaia* CCD is segmented into 4500 pixels in AL direction and 1980 pixels in AC direction - of the latter, 14 pixels are in the pre-scan region and not used for observations. Pixels are $10 \times 30\,\mu$m (AL $\times$ AC) and the TDI transfer time is $T_{\text{TDI}} = 0.9828\,$ms/pixel, resulting in an effective CCD exposure time of $4.4226\,$s.

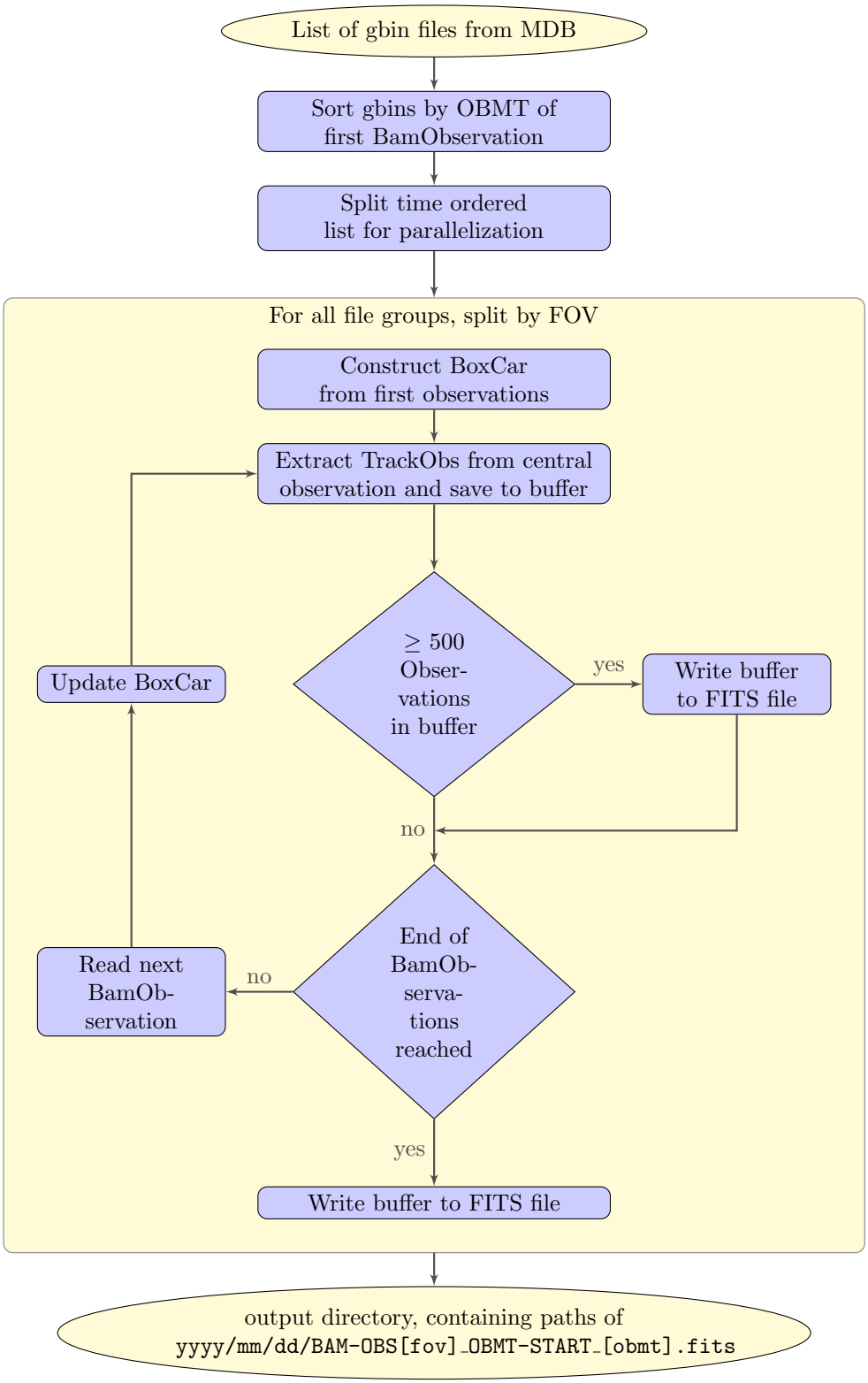

Figure 3.15: Flowchart for the extraction pipeline of the BAM-OBS dataset. The `[obmt]` in the last element refers to the acquisition time of the first BamObservation in the output file. The operations on each file group can be parallelized.

SM-SIF

SM-SIF images are recorded via the continuous readout of the signal acquired from TDI (see also Fig. 3.16). To avoid saturation from bright stars, Gate 12 is permanently activated, leading to a readout of only the last 2900 CCD lines in AL. Pixels are then binned to a factor of 2 in both AL and AC.

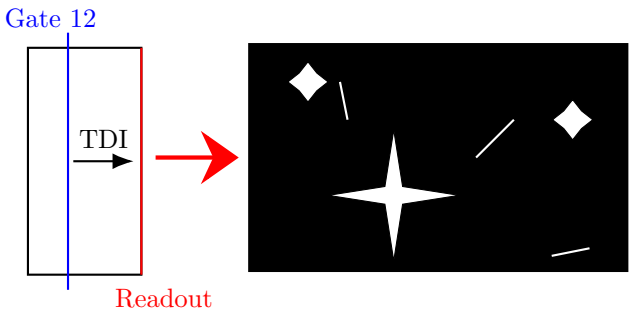

Figure 3.16: Scheme of an SM acquisition. The CCD area of each chip after Gate 12 is continuously read out via TDI (left). The resulting image (right) has the same dimension in AC but a dimension in AL dependent on the duration of the readout.

For clarity in notation, we will, from now on, use the following terms:

- A **CCD pixel** refers to a physical pixel on the actual CCD - i.e. one physical unit of $10 \times 30\,\mu$m
- An **image pixel** refers to a pixel in the image recorded after the TDI scan, including binning. While it still carries spatial information in AC, its AL information is a result of the integration over the sampled region in AL - it encodes both time and physical location. Thus, an image pixel does not correspond to a single physical pixel, but rather the history of an entire AL line during TDI.

The resulting image, then, consists of 983 image pixels in AC and a variable number N_{AL} of image pixels in AL - depending on the time over which data has been recorded (which is $T_{\mathrm{rec}} = T_{\mathrm{TDI}} \cdot 2N_{\mathrm{AL}}$).

From a physical pixel perspective, each CCD pixel has been exposed for the time T_{rec}, with the information of individual exposures spread over different image pixels in AL. The exposed area corresponds to that of 2900×1966 physical pixels.

From an image pixel perspective, each pixel has been exposed for exactly $T_{\mathrm{TDI}} \cdot 2900$, regardless of N_{AL}. The physical area of each image pixel corresponds to that of 4 physical pixels, due to binning.

As one can tell from the above, the physical perspective has a lower number of pixels, but a higher exposure time per pixel (assuming $2N_{\mathrm{AL}} > 2900$). The image perspective has more pixels, but lower exposure times. Irregardless of the perspective, the product $A_{\mathrm{exp}} \cdot T_{\mathrm{exp}}$ – which is of interest for computing fluxes – is always the same, being

$$\text{Physical}: A_{\text{exp}} \cdot T_{\text{exp}} = (2900 \cdot 1966 \cdot 10\,\mu\text{m} \cdot 30\,\mu\text{m}) \cdot (T_{\text{TDI}} \cdot 2N_{\text{AL}}) \tag{3.10}$$

$$\text{Image}: A_{\text{exp}} \cdot T_{\text{exp}} = (N_{\text{AL}} \cdot 893 \cdot 4 \cdot 10\,\mu\text{m} \cdot 30\,\mu\text{m}) \cdot (T_{\text{TDI}} \cdot 2900) \tag{3.11}$$

$$= 33.62 \left(\frac{N_{\text{AL}}}{1000}\right) \text{cm}^2\,\text{s} \tag{3.12}$$

Going forward, we will use the image perspective, as it is consistent with prior studies of the BAM image and more useful for the following sections. It is also, as we'll see later, easier to treat masked pixels. Nevertheless, both perspectives are equivalent for the calculation of fluxes.

SM-PPE

Aside from the cosmic ray data generated in this work, *Gaia*'s on-board processing provides a direct and instantaneous measurement cosmic ray hits in some of its CCDs in the form of a prompt-particle-event (PPE) counter.

These prompt-particle-events are detected on the SM chips by their so-called video processing units (VPUs). Each chip is equipped with its own VPU, which controls the chip, extracts and processes its science data and forwards it for further use. One of the tasks specific to the SM chips is that of object detection, in which astronomical objects are recognized in order to be tracked as they move over the remaining focal plane. These detection algorithms are described in detail by de Bruijne, J. H. J. et al. (2015).

As we have seen, cosmic rays also impact on the SM chips, with their tracks making up part of the features seen on SM images. Since the first step of the object detection by the video processing algorithms (VPAs) is the detection of local maxima, these tracks are also detected and must subsequently be rejected as non-astronomical objects. This is achieved via a twenty-parameter rejection algorithm based on the spatial shape of the local maximum in the image, rejecting objects with spatial frequencies below or above a certain cutoff, where the latter are the sharp particle tracks.

The number of objects rejected as PPEs in each SM chip is accumulated in an on-board counter and read out every 257.635 s, with the effective exposed chip area being the same as for SM-SIF observations. PPE count rates can as such be converted to the flux units used for the data products derived in this work via the factor

$$A_{\text{exp}} \cdot T_{\text{exp}} = (2900 \cdot 1966 \cdot 10\,\mu\text{m} \cdot 30\,\mu\text{m}) \cdot 257.635\,\text{s} \tag{3.13}$$

$$= 4405.5585\,\text{cm}^2\,\text{s}. \tag{3.14}$$

These PPE values have been used before as a way to track cosmic rays on *Gaia* by Crowley et al. (2016) and Abreu (2017). They will also be used in the analysis below, as their regular sampling distinguishes them from SM-SIF measurements.

BAM-OBS and BAM-SIF

For the BamObservations, pixels are binned by a factor of 4 in AC and not binned at all in AL. This choice was made in order to best measure the shift of the interference patterns in the AL direction.

The determination of an exposure time in both pictures for the BamObservations is complicated by the fact that it is not only a TDI observation, but also contains a period of staring. Normally,

the BAM CCD is operated in TDI mode, in the same way as the SM CCD. To record the interference pattern, an exception is made – for an integration time of 19 s, the shifting of charges is stopped and the chip operates in a kind of staring mode. In nominal BamObservations, data is then only aquired from sub-regions of the CCD that have been illuminated by the BAM pattern. BAM-SIF images use the entire CCD in AL direction along a restricted AC range.

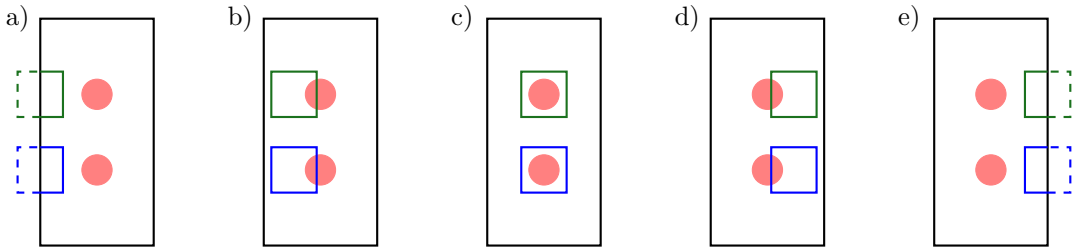

Figure 3.17: Readout scheme for the interference patterns in BAM-OBS. BAM fringe patterns are outlined as red circles. a) Create the readout windows. b) Move the readout windows via TDI. c) Stare observation – charges are not shifted for 19 s. d) Move readout windows via TDI. e) Readout, recording only contents of windows.

The observation principle and the effect on imaging particle tracks is shown in Fig. 3.17. Effectively, data is collected from two windows, outlined in green and blue. These two windows have an unbinned length of 1000 in AL and 320 in AC each, resulting in a physical area of about $1\,\mathrm{cm}^2$. They first move across the chip, stay in place during the staring, and then move again to the readout register.

In BAM-SIF observations, we can make a similar estimation of the readout window sizes, although the image dimensions are variable. We will from now on use two values N_{AL} and N_{AC} to refer to the binned image dimensions of the result image. The used unbinned lengths are then N_{AL} and $4\,N_{\mathrm{AC}}$, respectively – for reference, a nominal BamObservation has $N_{\mathrm{AL}} = 1000$ and $N_{\mathrm{AC}} = 80$

The exposure can once again be viewed in two pictures, the physical pixel and image pixel based ones. In the former, it is easy to see that the entire region both readout windows cross is exposed – the exposed area is $4500 \times 4\,N_{\mathrm{AC}}$ pixels (AL × AC) per pattern. The exposure time, however, is more complex: First, the entire exposed region is exposed for $N_{\mathrm{AL}} \times T_{\mathrm{TDI}}$, due to the movement of the readout windows across the chip. Additionally, the region used for staring is observed for a further 19 s. The exposure time is, as such, AL-dependent.

In the image picture, the calculation is much easier. Viewing each readout window as a physical unit, the exposed area per window is simply $N_{\mathrm{AL}} \times 4\,N_{\mathrm{AC}}$ pixels. The exposure time is simply the TDI transfer time across the whole chip plus the staring time.

The product of exposed area and exposure time, which is of interest for flux determination, is in both pictures (per readout window)

$$\begin{aligned}
\text{Physical}: A_{\mathrm{exp}} \cdot T_{\mathrm{exp}} &= (4500 \cdot 10\,\mu\mathrm{m} \cdot 4\,N_{\mathrm{AC}} \cdot 30\,\mu\mathrm{m}) \cdot (N_{\mathrm{AL}} \cdot T_{\mathrm{TDI}}) && (3.15)\\
&\quad + (N_{\mathrm{AL}} \cdot 10\,\mu\mathrm{m} \cdot 4\,N_{\mathrm{AC}} \cdot 30\,\mu\mathrm{m}) \cdot (19\,\mathrm{s}) && (3.16)\\
\text{Image}: A_{\mathrm{exp}} \cdot T_{\mathrm{exp}} &= (N_{\mathrm{AL}} \cdot 10\,\mu\mathrm{m} \cdot 4\,N_{\mathrm{AC}} \cdot 30\,\mu\mathrm{m}) \cdot (4500\,T_{\mathrm{TDI}} + 19\,\mathrm{s}) && (3.17)\\
&= 22.49\,\mathrm{cm}^2\,\mathrm{s} \quad (\text{for BAM–OBS}). && (3.18)
\end{aligned}$$

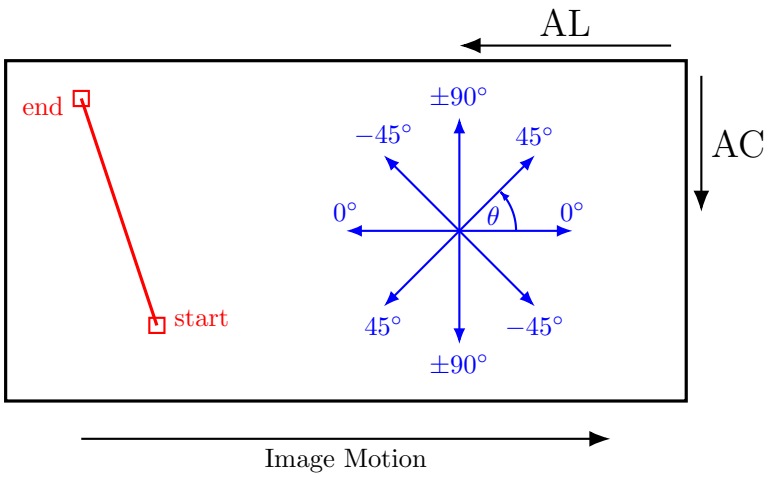

Figure 3.18: Definition of the track angle θ in the standard *Gaia* CCD reference system. The red line on the left shows an example track, whose start is always defined as the end-point at the lower AL-coordinate. The blue compass rose shows the angle corresponding to different cosmic ray trajectories.

Masked Pixels

In both SM and BAM images, some image pixels can not be used for the determination of cosmics. In the SM, these pixels are mostly caused by the bright star masking algorithm. For the BAM, charge overflow effects can be caused by a high energy cosmic coincident with an interference fringe, fully saturating the pixel and causing errors in the readout of several following pixels.

Correcting the exposed area for these masked pixels is very easy in the image picture, as we simply discard these pixels, meaning one can calculate the exposed area using

$$A_{\text{exp}} = (N_{\text{tot}} - N_{\text{mask}}) \cdot b_{\text{AL}} \cdot b_{\text{AC}} \cdot 10 \cdot 30\,\mu m^2, \tag{3.19}$$

with N_{tot} being the total number of image pixels, N_{mask} being the number of masked pixels and b_{AL} and b_{AC} being the binning factor in AL and AC, respectively.

3.4.2 Track Geometries

For particle tracks that pass through multiple pixels, it is possible to estimate the angle of a cosmic's path on a CCD with respect to the FPA and the length of the path of the particle through the chip. For a selected subset of tracks, this was attempted using either simple estimates or a fitting technique.

Figure 3.18 shows the definition of the track angle θ used in this analysis. It is obtained via the slope of a line describing the cosmic ray track in an (AL,AC) coordinate system, e.g.

$$\theta = \tan^{-1}\left(\frac{AC_{\text{end}} - AC_{\text{start}}}{AL_{\text{end}} - AL_{\text{start}}}\right)\,[^\circ], \tag{3.20}$$

where the starting point of a track is always defined to be its edge point at the lower AL value. We have made this choice because we cannot determine at which of the edge points of a track the cosmic entered and exited the CCD. As such, θ is defined in a range of $[-90^\circ, 90^\circ]$, with 0° corresponding to a track completely along the AL axis, $\pm 90^\circ$ being oriented in the AC direction.

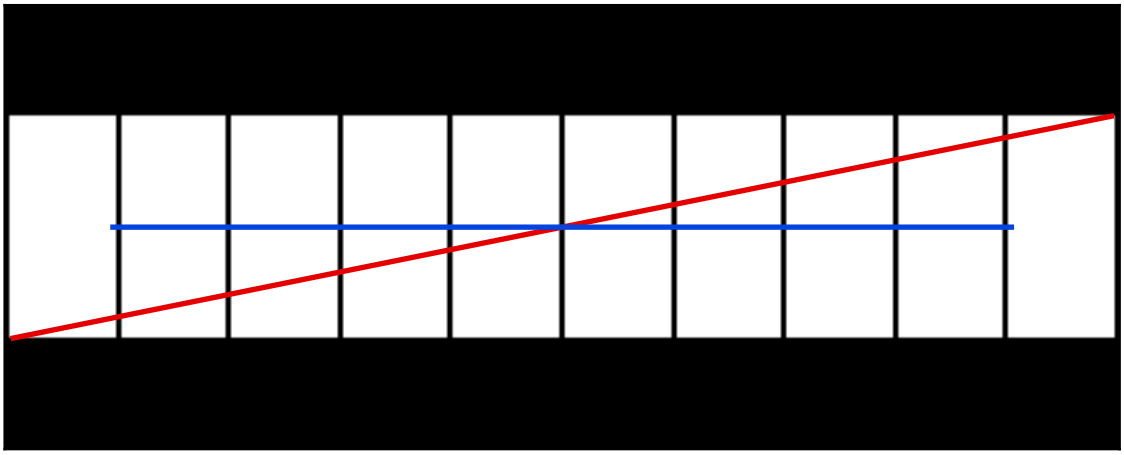

Figure 3.19: Possible track lengths and angles in a one-dimensional track in AL. The longest, steepest track in red passes through the corners of the most distant pixels, while the shortest, flattest track in blue starts and ends near the nearest edges of the outermost pixels.

For a track that is one-dimensional, meaning that all its signal pixels are in one line or column, the angle and track length are constrained and can be estimated with a simple algorithm, outlined in Figure 3.19. The particle trajectory can be between two extremes: either perfectly aligned to the AL/AC direction or running between the corners of the signal pixels at the edge of the track.

In formulas: A track along an AL line has an angle θ of

$$\theta = 0^\circ \pm \tan^{-1}\left(\frac{h_{\mathrm{AC}}}{w_{\mathrm{AL}} \times N_{\mathrm{AL}}}\right) \tag{3.21}$$

and a length l of

$$w_{\mathrm{AL}} \times (N_{\mathrm{AL}} - 2) \leq l \leq \sqrt{(w_{\mathrm{AL}} \times N_{\mathrm{AL}})^2 + (h_{\mathrm{AC}})^2}, \tag{3.22}$$

with

- N_{AL} being the number of binned pixels in AL,
- w_{AL} being the pixel width (i.e. in AL direction) after binning,
- h_{AC} being the pixel height after binning.

This can be calculated analogously for a track along an AC column. For such tracks, we define our output values for the track angle and length as the mean of Equations 3.21 and 3.22 respectively. The uncertainty is then half the absolute value of the difference between the two extreme values of these equations.

For tracks that are not aligned with the AL and AC direction, we use a fitting routine to determine θ, which we in turn use to determine l. The fitting routine is shown in Figure 3.20.

With each track image, we first determine the length of the bounding box in binned samples along the AL and AC direction. For each pixel coordinate in the longer axis, we determine the center of mass of the track image values along the shorter axis (e.g. if the image has more pixels in AL, we compute the center of mass along the AC axis for each line). The resulting pairs of

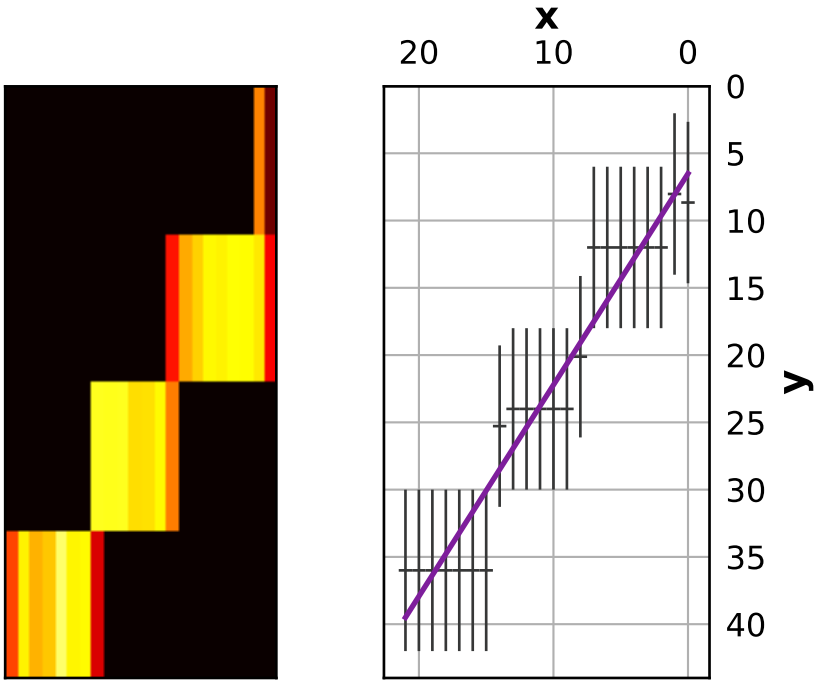

Figure 3.20: Fitting routine on two-dimensional tracks on the example of a BAM-OBS track. *Left:* Track image, with the pixels scaled to their physical dimension. *Right:* Best fit. The (x, y) pairs have been computed by calculating the center of mass along AC for each AL-line, with the error bars representing the pixel size. The purple line shows the best line fit as determined by orthogonal distance regression.

values are saved in an (x, y) array, with the x-value denoting the location in AL and the y-value denoting the location in AC multiplied by the factor $f_{\text{pix}} = 3 \times \frac{\text{AC binning}}{\text{AL binning}}$. x and y are, as such, in the unit of binned AL pixels.

The rationale for using the center of mass is that can better estimate the trajectory of a cosmic if it causes a signal in, for instance, two adjacent pixels in a column – see the Figure 3.20.

For each (x, y) pair, we set an uncertainty $(\sigma_x = 0.5, \sigma_y = 0.5 f_{\text{pix}})$, representing the uncertainty of the detection location due to pixelisation. We then perform a fit of a simple fit to a line equation,

$$y(x) = m \cdot x + y_0, \tag{3.23}$$

using the `scipy` implementation of the Orthogonal Distance Regression algorithm (Boggs et al., 1989). This algorithm takes into account the uncertainties of both x and y, providing best fit values and estimations on the standard deviations σ_m and σ_{y_o} of the slope and offset.

To determine the angle theta and its uncertainty, we utilize the inverse tangent and gaussian error propagation, yielding

$$\theta = \tan^{-1}(m), \quad \sigma_\theta = \frac{1}{m^2 + 1}\sigma_m \tag{3.24}$$

to determine the length of the cosmic, we define the distances d_x and d_y as the difference of x and y between the first and last (x, y) pairs – if the image has more pixels in AL ($N_{\text{AL}} \geq N_{\text{AC}}$), this would be the pairs at the lowest and highest AL, respectively.

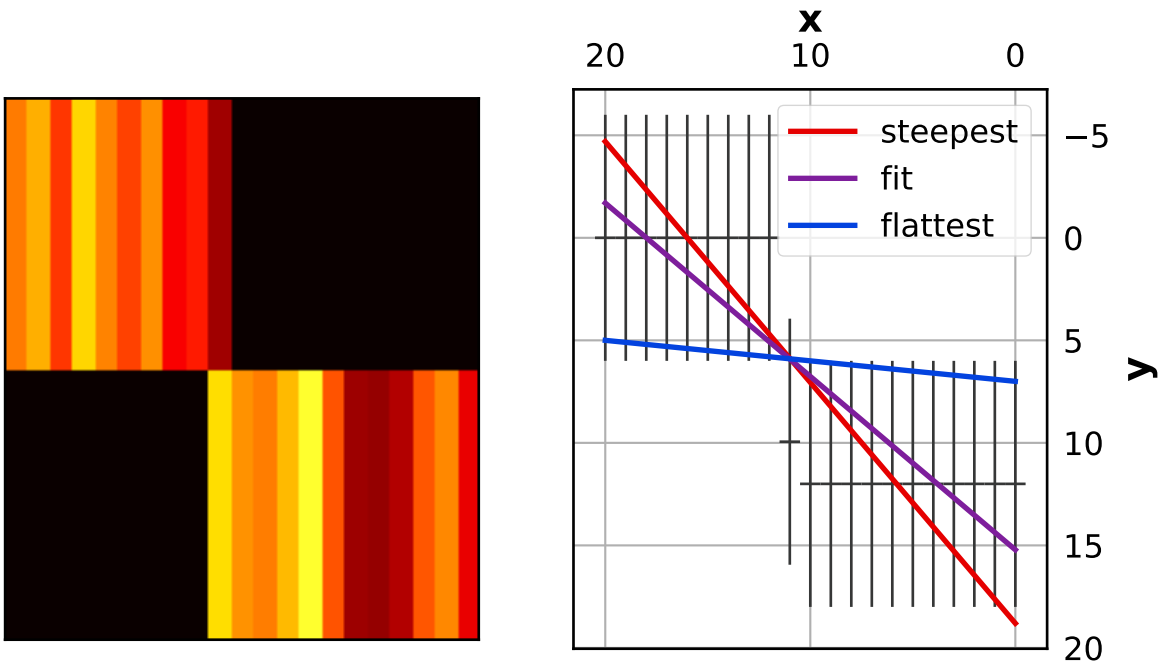

Figure 3.21: Issues with fitting tracks whose length in AC or AL is 2. *Left:* Track image, with the pixels scaled to their physical dimension. *Right:* Best line fit and the steepest and flattest plausible associated tracks.

To calculate the length, we separate into two cases:

1. If $N_{\mathrm{AL}} \geq N_{\mathrm{AC}}$, use $d_y = m \cdot d_x$. Then

$$l = \sqrt{d_x^2 + d_y^2} = \sqrt{m^2 + 1} \cdot |d_x|, \tag{3.25}$$

$$\sigma_l^2 = \left(m^2 + 1\right) \cdot 2\sigma_x^2 + \frac{m^2 d_x^2}{m^2 + 1} \cdot \sigma_m^2, \tag{3.26}$$

   using Gaussian error propagation for σ_l.

2. If $N_{\mathrm{AL}} < N_{\mathrm{AC}}$, use $d_x = m^{-1} \cdot d_y$. Then

$$l = \sqrt{d_x^2 + d_y^2} = \sqrt{m^{-2} + 1} \cdot |d_y|, \tag{3.27}$$

$$\sigma_l^2 = \left(m^{-2} + 1\right) \cdot 2\sigma_y^2 + \frac{d_y^2}{m^4 + m^6} \cdot \sigma_m^2, \tag{3.28}$$

   using Gaussian error propagation for σ_l.

the separation into two cases was chosen to avoid numerical instabilities, since d_y and m are very small in case 1, while d_x is very small in case 2, and m very large.

This fitting routine was then applied to a subset of all detected tracks in a TrackObs, namely those that

1. are two dimensional ($N_{\mathrm{AL}} > 1$ and $N_{\mathrm{AC}} > 1$) and
2. contain at least 5 pixels with a signal value.

In addition, tracks with $N_{\mathrm{AL}} = 2$ or $N_{\mathrm{AC}} = 2$ must also be significantly longer in their other dimension. This is due to the fact that, as Figure 3.21 outlines, there is a very high uncertainty in the distance crossed along the dimension whose length is two pixels.

To test these analysis routines, we once again used the T.A.R.S. simulator to provide input cosmic rays with known quantities - in this case, the true angle θ and projected path length l. We used the simulator to generate cosmic ray sub-images akin to those saved into a track observation. This was done for two cases - one being an SM-like thin chip with a binning of 2 in both AL in AC, the other being a BAM-like thick chip with a binning of 4 in AC and no binning in AL.

In this way, we could predominantly examine the effects of binning and the resulting pixel geometry on the retrieval of the track geometries.

In the case of the SM-like chip, Figure 3.22 plots the input angle of the source cosmic versus the measured angle for a long simulation run. Within their accuracies, the measured angles represent the input angles.

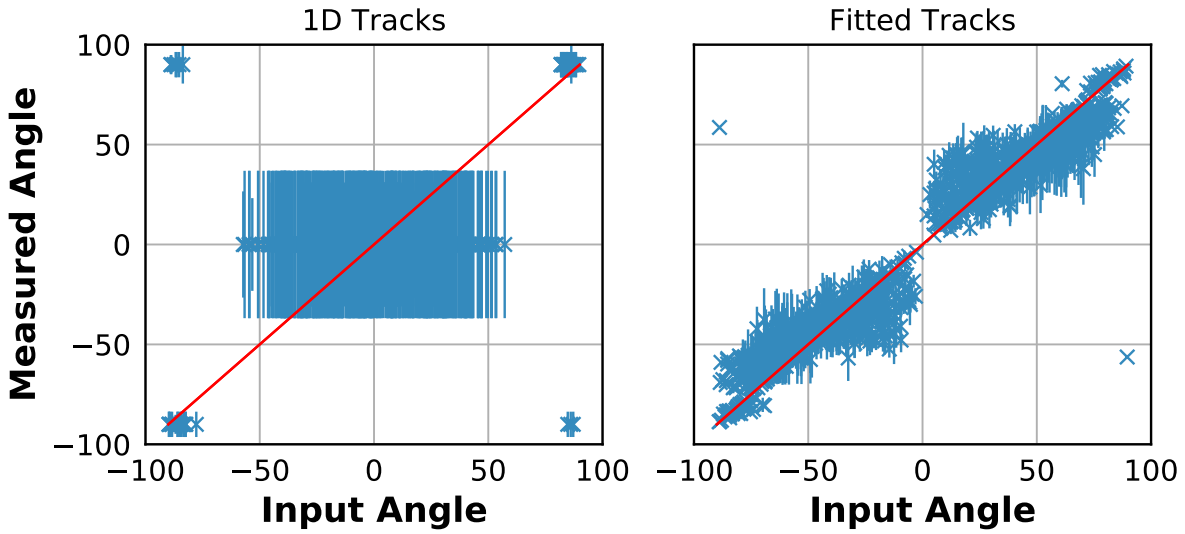

Figure 3.22: Input angle vs measured angle (in units of degrees) for SM-SIF observations. The error bars represent the uncertainty of the recovered angles, the red diagonal represents the optimal values. The results for one-dimensional and fitted tracks are in the left and right panel, respectively.

This is better illustrated in Fig. 3.23, which shows histograms of the difference between measured and input angles, normalized by the calculated uncertainties. Here we see that while the fitted cosmics fall well into a Gaussian, the one-dimensional tracks show a bi-modal distribution, where track angles are either systematically under- or over-estimated. Examining Fig. 3.22, these cosmics appear to be those with very large input angles that are nonetheless seen at $\theta = 0°$.

Figure 3.24 shows similar histograms for the error in the measured track length. These are within the ranges expected by their uncertainty, with a slight systematic overestimation in both indicated by the offset of the maximum from 0.

The same analysis for the BAM-like chip shows different systematics. As Figure 3.25 shows, a population of the fitted tracks with $|\theta| \leq 60°$ is redistributed to $|\theta| \approx \pm 60°$. This is most likely due to the 1×12 aspect ratio of the binned pixels making these tracks appear to have similar angles.

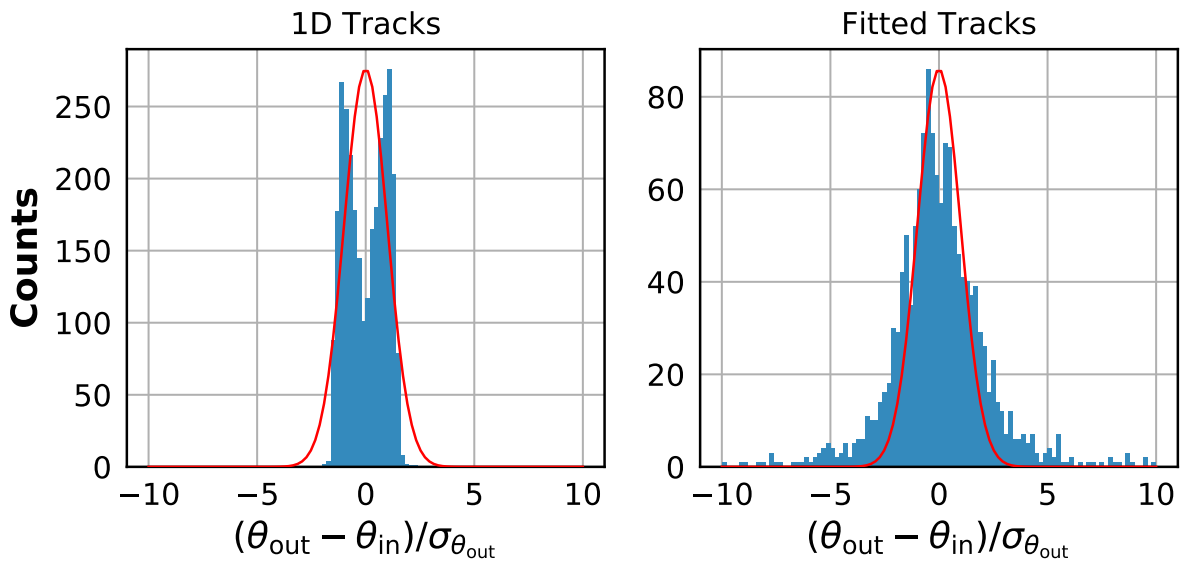

Figure 3.23: Histograms for the difference of the output angle to the input angle in SM-SIF observations, normalized by the calculated angle uncertainty. The left and right panel show the values for one-dimensional and fitted tracks, respectively. The red curves represent Gaussians with a standard deviation of 1.

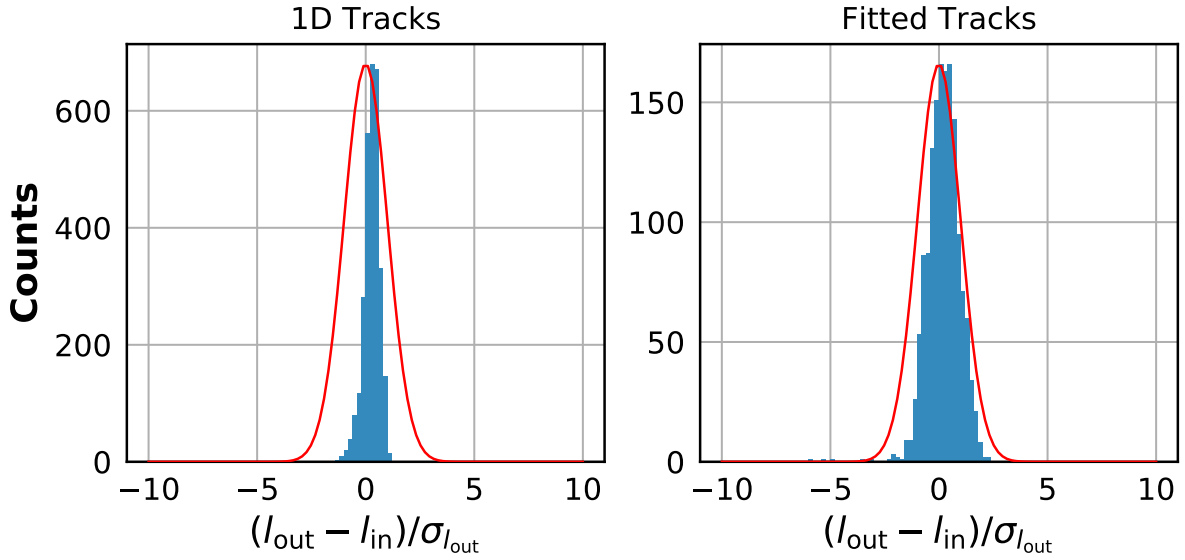

Figure 3.24: Histograms for the difference of the output track length to the input track length in SM-SIF observations, normalized by the calculated length uncertainty. The left and right panel show the values for one-dimensional and fitted tracks, respectively. The red curves represent Gaussians with a standard deviation of 1.

The error histograms of the measured angles (Fig 3.26) show that while the one-dimensional tracks are all correct within the limits of their uncertainty, the fitted tracks contain some outliers with respect to the bell curve - these are the same cosmics that are mistakenly redistributed to higher angles.

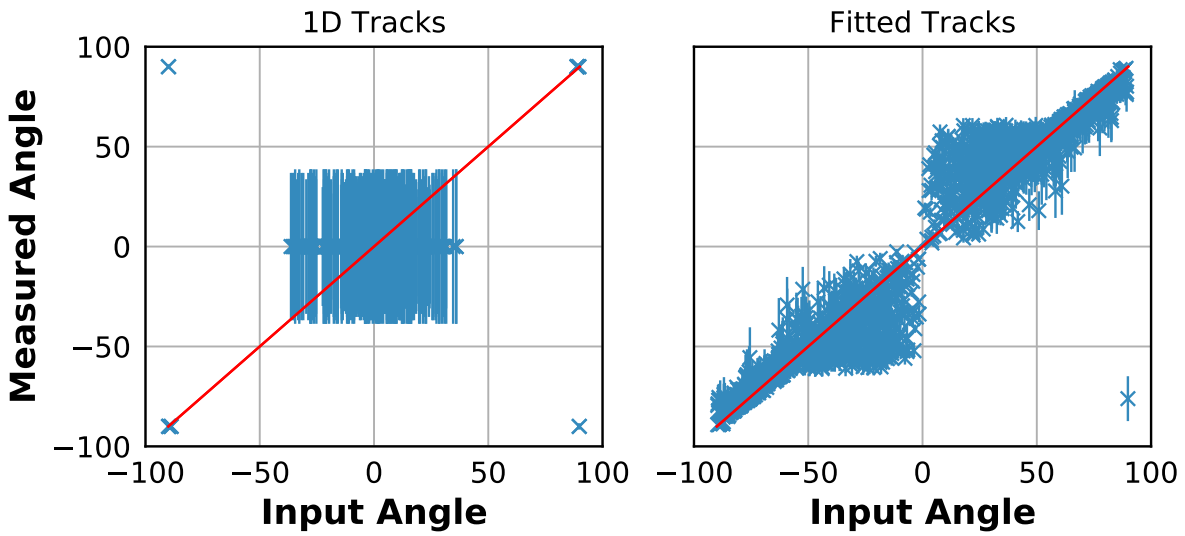

Figure 3.25: Input angle vs measured angle (in units of degrees) for BAM-OBS and BAM-SIF observations, as in Fig. 3.22.

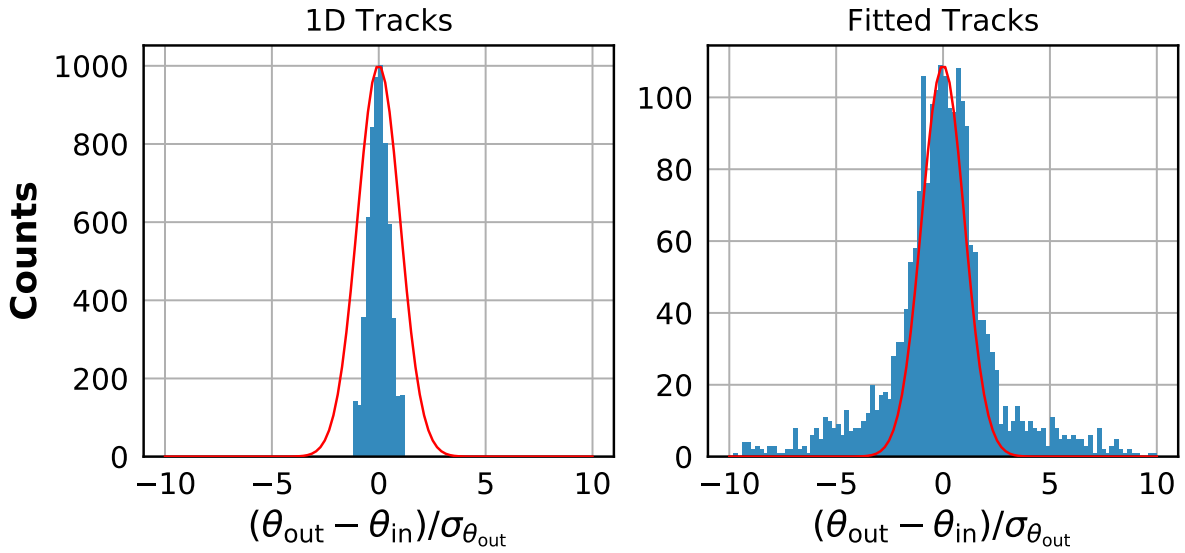

Figure 3.26: Histograms for the difference of the output angle to the input angle in BAM-OBS and BAM-SIF observations, as in Fig. 3.23.

The measured lengths, plotted for the BAM-like chip in Figure 3.27 are once again correctly estimated, with a trend towards an overestimation of the length.

3.4.3 Edge Tracks

Users may not want to use tracks that are located at the edges of a readout window, as the detection does not contain the full energy dumped by the cosmic on the CCD, leading to artificially low energies. We mark these tracks, applying a flag whenever one or more edges of

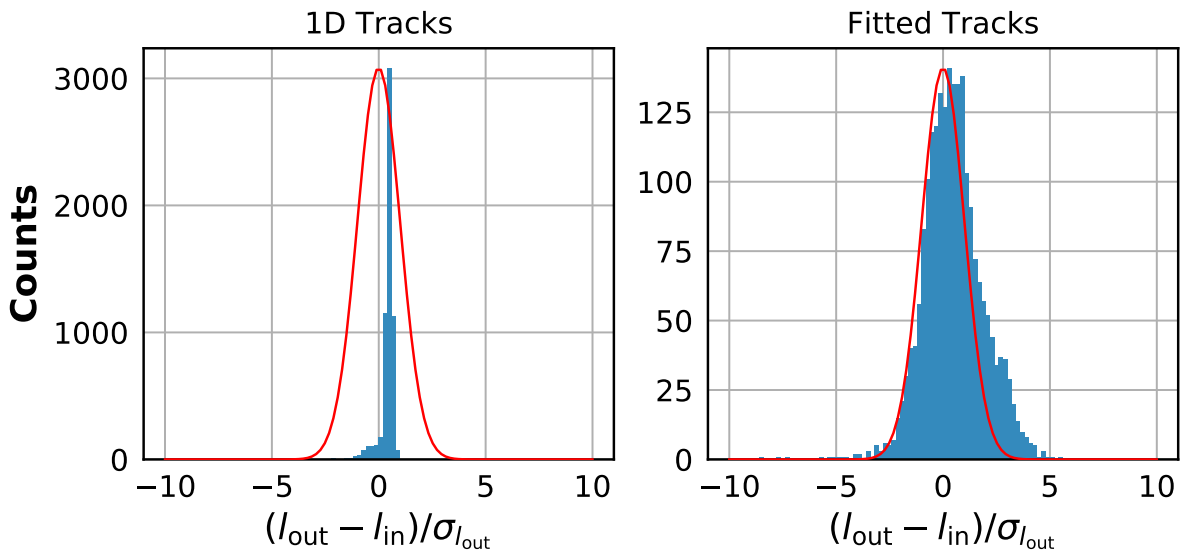

Figure 3.27: Histograms for the difference of the output track length to the input track length in BAM-OBS and BAM-SIF observations, as in Fig. 3.24.

the bounding box of a track is located on the edge of the input image.

3.4.4 Post-Processing Pipeline

Using the algorithms outlined in this subsection, we process the TrackObs FITS files into FITS files containing the final output product called *CosmicObservations*, defined in Appendix B.1. This dataset is essentially a modification of the TrackObs dataset, adding the calculated fluxes per observation and track geometries to individual tracks while removing the sub-image of the track to reduce file sizes.

Due to this definition of CosmicObservations, there is a 1:1 correspondence of each element of the latter dataset to the output dataset. The operations of the post-processing pipeline are:

1. For each TrackObs FITS file:
    1.1. Create a buffer for CosmicObservations
    1.2. For each TrackObs in the FITS file:
        1.2.1. Calculate the flux and its uncertainty (Sec. 3.4.1)
        1.2.2. Determine the track geometry, where applicable (Sec. 3.4.2)
        1.2.3. Determine which tracks are at the edge of the input image (Sec. 3.4.3)
        1.2.4. Create a CosmicObservation from the TrackObs and above data and save it to the buffer
    1.3. Write all the CosmicObservations in the buffer to a FITS file, replicating the directory structure that the TrackObs file has been read from.

As this algorithm acts independently on each input file, it is very easily parallelized. The output directory is then a direct replica of the input TrackObs directory, including sub-folders and filenames.

Chapter 4

Dataset Analysis

After extracting cosmic ray data from *Gaia* observations, we will now inspect the produced datasets. This section should not primarily be understood as an analysis with the goal of producing new scientific results regarding *Gaia*'s radiation environment, but rather as a validation of the extracted data.

In particular, we will first examine the distribution of track energies obtained from CosmicObservations (Sec. 4.2), comparing our data with both a simple model distribution as well as between chips. We will find that both are consistent, with some systematic differences in the track energies recovered from different source observations, hinting at possible sensitivity differences.

After the track energies, we will compare the particle rates measured on the same chips using different algorithms, where we will find small systematic deviations between regularly sampled datasets and irregular or sparse datasets. These deviations will be small enough that we can use the regularly sampled data for particle monitoring.

As an external validation, we will then compare particle rates as a function of time from *Gaia* with space weather data from dedicated particle instruments on other satellites. We will find that our data reproduces these external particle fluxes rather well in both galactic cosmic ray and solar energetic particle behavior, with some additional signatures in our data due to *Gaia*'s shielding and orbit around L_2.

Finally, we will attempt to use CosmicObservations to measure the ionizing energy loss rates of cosmics in *Gaia*'s CCDs, which we will find to be consistent with minimum ionizing particles making up the GCR background and additional less energetic particles produced by solar events.

The data considered from this section has been extracted from January 3, 2014 to January 20, 2018, thus covering roughly four years.

4.1 Sampling

Before looking at the produced cosmic ray data itself, it is instructive to consider the sampling of our individual datasets.

This is very simple for the BAM-OBS and SM-PPE datasets – barring small data gaps, their sampling is completely regular, generated for each chip and FoV every 23.4 s and 257.6 s, respectively.

BAM-SIF observations, on the other hand, are taken on a semi-regular basis, shown in the top

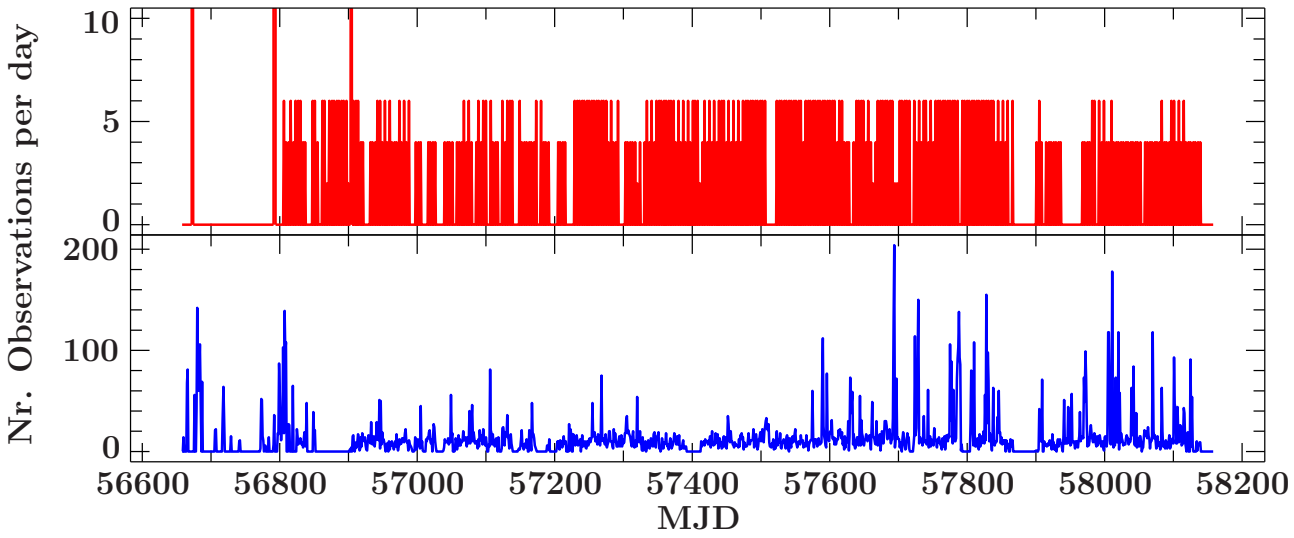

Figure 4.1: Sampling of the BAM-SIF and SM-SIF datasets.

Table 4.1: Number of observations per SIF dataset from Jan 2014 to Jan 2018. Observations in SM-SIF are summed over all chips, as for this dataset, images are taken independently in individual chips.

Source	Total Nr. Observations	Comment
BAM-OBS	5133457	Per FoV (2 total)
SM-PPE	458718	Per Chip (14 total)
BAM-SIF	1561	Per FoV (2 total)
SM-SIF	18881	Sum over Chips (14 total)

panel of Fig. 4.1. Twice a week, two to three observations are taken sequentially, resulting in four to six CosmicObservations – one per FoV. Some data-gaps exist, however, as seen in the figure.

The sampling of SM-SIF observations is the least regular out of all, being triggered only when objects of interest are in view. This can be seen in the bottom panel of Fig. 4.1, which shows the number of observations per day summed over all chips. One can see some periods with no observations, due to downlink constraints when *Gaia*'s rotation was aligned with the galactic plane and large amounts of stars were detected in the AF. Later on in the mission there are more manually triggered observations. The number of observations is approximately equally split over all chips.

Table 4.1 also lists the total number of observations per dataset within the considered time frame of January 2014 to January 2018.

4.2 Deposited Energies

As a CosmicObservation records the total deposited energy of every detected particle track, we can examine the distributions of these track energies. After motivating an expected energy distribution from first principles and comparing it to a measured distribution, we will compare the energy distributions measured in different datasets with each other, showing possible sensitivity differences.

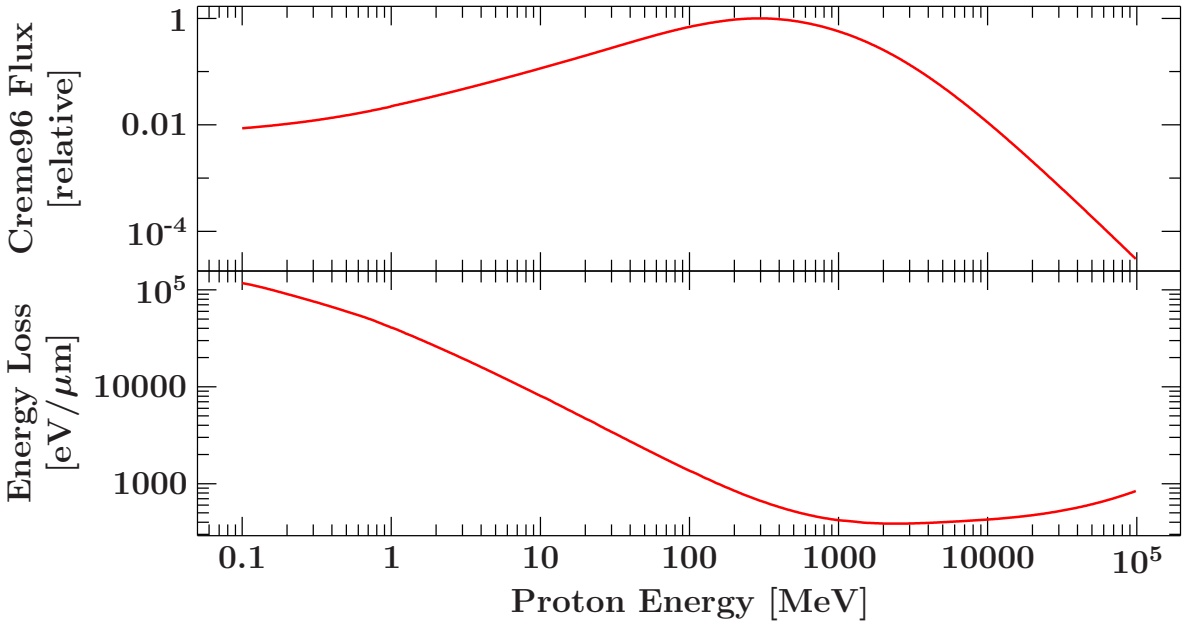

Figure 4.2: *Top:* Differential proton flux as estimated by Creme96 at the L_2 point with 1.1 cm of Aluminum shielding. *Bottom:* Mean energy loss of protons as a function of energy in crystalline Si as calculated by the PSTAR program. After shielding, the proton flux is highest for minimum ionizing particles.

4.2.1 Distribution of track energies

The measured total deposited energy of a particle will be determined by two factors: Its energy loss per unit length dE/dx, as well as its path length through the detector's depletion zone, p_{dep}.

Neglecting small-angle scattering, p_{dep} is only a factor of the particle's entrance angle α into the chip. Defining $\alpha = 0°$ as perpendicular to the chip's surface and d_{dep} as the detector's depletion zone depth, we can write

$$p_{\mathrm{dep}} = d_{\mathrm{dep}} / \cos\alpha. \tag{4.1}$$

Further assuming that a particle's mean energy loss stays constant even as it loses kinetic energy via ionization (justified by the relatively thin *Gaia* CCDs), the deposited energy dE of a particle with kinetic energy E_{k} is

$$dE(E_{\mathrm{k}}, \alpha) = p_{\mathrm{dep}}(\alpha) \cdot \left\langle -\frac{dE}{dx}(E_{\mathrm{k}}) \right\rangle, \tag{4.2}$$

where $\langle -dE/dx \rangle$ can be taken from Eq. 1.1 or tabulated values. For a monoenergetic particle distribution, the distribution of dE would as such only be a function of its angular distribution.

To construct an expected track energy distribution for *Gaia* measurements, we utilized tabulated values of both the expected proton flux at *Gaia*'s CCDs as a function of energy and their corresponding mean energy loss in crystalline silicon. Relative proton fluxes were calculated by Creme96 (Tylka et al., 1997) at L_2 assuming 1.1 cm of aluminum shielding (a simplification of the FPA's shielding), while mean electronic energy losses in crystalline silicon for protons were taken from the PSTAR database (Berger et al., 2005). Both are shown in Fig. 4.2.

For all energies shown in Fig. 4.2, we generated an expected distribution of dE by uniformly

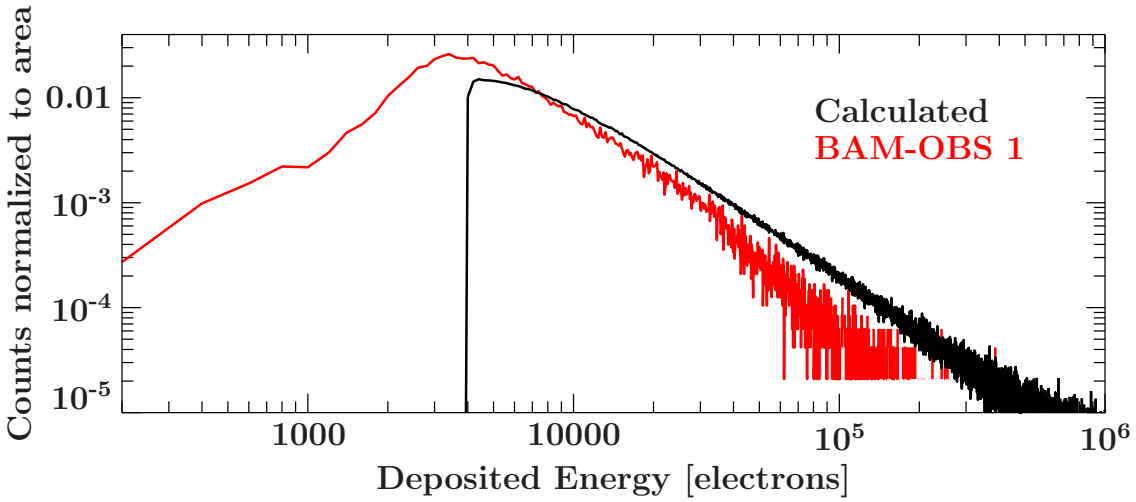

Figure 4.3: Calculated and measured distributions of deposited energies by cosmic rays in a BAM chip. The black line has been calculated from Fig. 4.2 assuming isotropic particle entrance angles, while the red distribution is measured from BAM-OBS FoV 1. While the curve shapes generally match, simplifications in the assumed energy depositions lead to different most frequent energies.

sampling angles $0° \leq \alpha < 90°$ (to avoid infinite path lengths) and applying Eq. 4.2. To get the deposited energy in our measured units (electrons), we divided dE by the mean ionization energy in silicon, 3.6 eV. The individual distributions were then summed up after weighing them by the relative flux corresponding to the particle energy taken from Creme96.

Fig. 4.3 plots this calculated distribution along a measured distribution from a quiescent day of BAM-OBS (FoV 1) data. The depletion zone depth in Eq. 4.1 was set to 38 μm, matching the BAM chip. Both histograms were normalized to the same area for comparison. From this figure, we can see that the measured and calculated distributions roughly match, showing a low-energy maximum followed by a similar slope. However, the most frequent deposited energies do differ, with no signal below about 4000 e^- (corresponding to MIPs with $\alpha = 0°$) in the calculated distribution, while the measured distribution shows many particles below that energy.

This is not unexpected, due to the simplifying assumptions made when constructing our calculated energy distribution – similar differences were seen by (Garcia et al., 2018) using the same assumptions in their Monte Carlo simulations compared to BAM-SIF data. In their case, the above discrepancies were fixed when using a cosmic hit list generated via Geant4 simulations, using more sophisticated incident particle distributions (both in particle species and entrance angles) and energy deposition (simulating small-angle scattering, escape processes and proper energy deposition statistics as opposed to just taking the mean).

Altogether, the considerations in this subsection show that the measured track energy distributions can be explained by simple models, although a detailed analysis would require a much more sophisticated treatment of the physics of energy loss mechanisms.

4.2.2 Differences between datasets

In order to reveal and understand possible systematic differences in CosmicObservations extracted from different sources, we will now compare deposited energy histograms for BAM-OBS, BAM-SIF and SM-SIF datasets with each other.

To get sufficient statistics, we will consider dE-histograms averaged over multiple days and thus

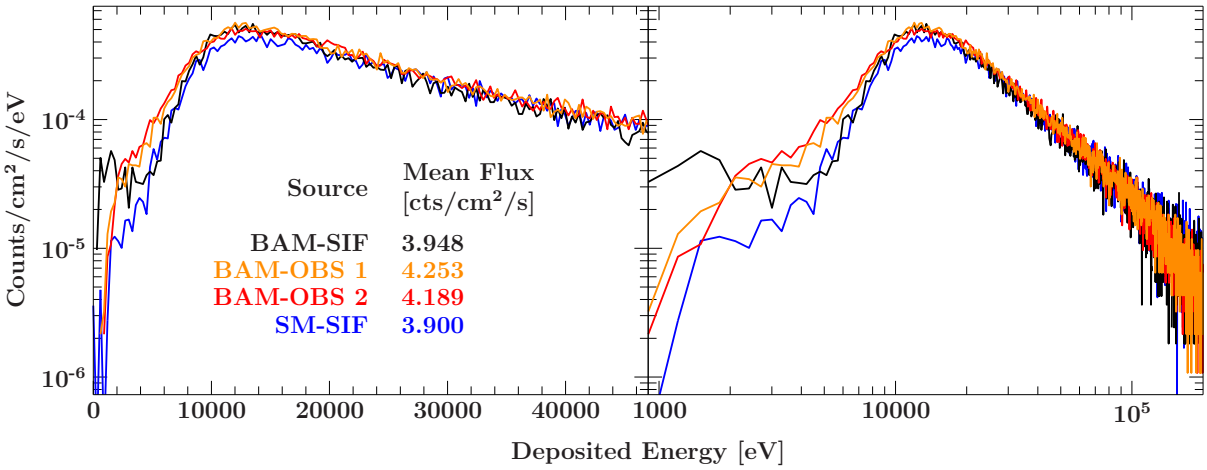

Figure 4.4: Differential deposited energy histograms for BAM-OBS FoV 1 and 2, BAM-SIF and SM-SIF data. SM-SIF track energies were scaled up by a factor of 38/12 to account for different depletion zone thicknesses. SIF data have been averaged between different chips and FoV. BAM-OBS and SM-SIF data were taken from June 6 to 22, 2017, while BAM-SIF data were averaged over the entire year 2017. The right panel shows a larger energy range on a logarithmic energy axis.

CosmicObservations. For each CosmicObservation separately, we first generate a raw differential counts-per-dE-bin histogram. These histograms are then summed up per bin, with each histogram weighted by its measured flux. For comparison between datasets, we then normalize all histograms such that their integral over dE equals the mean flux of all CosmicObservations used in their generation.

Fig. 4.4 shows these dE-histograms for BAM-SIF, SM-SIF and BAM-OBS data. While both FoVs of BAM-OBS are plotted separately, SM-SIF and BAM-SIF use observations from all chips and fields of view. Deposited energies were converted to units of eV from the raw electron values using the mean ionization energy of Si (3.6 eV), with energies in SM scaled up by a factor of 38/12 to account for the thinner depletion zone of its chips (12 μm as opposed to 38 μm in BAM). BAM-OBS and SM-SIF use data with no solar activity (June 6 to June 22, 2017), while BAM-SIF uses the whole year 2017 due to worse sampling. The ratios of all other distributions to BAM-OBS FoV 1 are also shown in Fig. 4.5.

Examining the distributions, we see several differences: For one, BAM-SIF measures an excess of tracks with energies below 2000 eV – these are most likely not actual particle tracks, but rather stray light which is also picked up by the simple thresholding algorithm used for this dataset.

Above this possible stray light, here is an excess in tracks with energies between about 2000 eV to 10000 eV in BAM-OBS data compared to BAM-SIF data. These energies are rather far below what one would expect of a minimum ionizing particle, and may actually be false positives, meaning shot noise in the BAM interference pattern misidentified as cosmics. As BAM-SIF observations do not search for cosmics on the interference pattern, such false positives would only be expected in BAM-OBS data.

At energies higher than the most frequent track energy, however, the BAM-OBS distributions show a slight excess with respect to BAM-SIF, as can also be seen in the mean flux given in Fig. 4.4. As we will see in Sec. 4.3, however, this is most likely due to the non-linear increase in overall cosmic ray rates over time and the fact that we averaged BAM-SIF data over a longer period of time than BAM-OBS data.

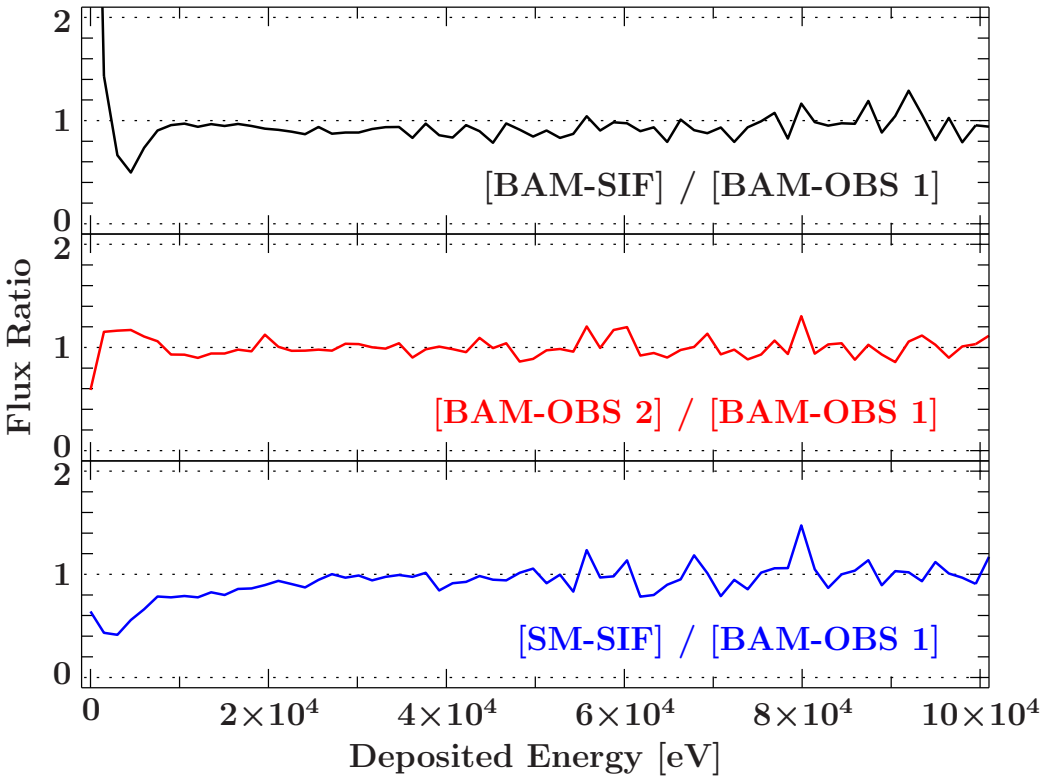

Figure 4.5: Ratios of the deposited energy histograms in Fig. 4.4 to BAM-OBS FoV 1.

Comparing BAM-OBS data in both FoVs, there don't appear to be any significant excesses in either dataset relative to the other.

Looking at SM-SIF data, we mostly see a lack of tracks with (rescaled) energies below about 40000 eV compared to BAM data. This is most easily explained by the thinner AF-type chips used by the SM, leading to a lower signal of these tracks in SM observations. Coupled to the fact that the varying sky-background in SM observations is less well-modeled during extraction than the consistent pattern BAM images, this may very well be a sensitivity issue.

Aside from these systematic differences, we can see that the general shape of the track energy histograms mostly match, especially towards higher energies. Given that the images these tracks are taken from should observe the same radiation environment, this is a good indicator of the quality of the extraction algorithms developed above. Most notably, the the strong interference pattern in BAM observations does not appear to significantly impede the detection of cosmics.

4.3 Fluxes

The particle flux measured by a CosmicObservation (as defined in Sec. 3.4.1) is a very useful high-level output of this study, giving a simple and frequent measure of *Gaia*'s radiation field, as opposed to the more long-term studies of radiation damage. Most notably, it can easily be compared with particle rates measured by other satellites at other locations in the solar system. Before making these external comparisons, we will however first examine the consistency of CosmicObservation fluxes with each other and with an existing radiation monitoring data product of *Gaia*, the prompt-particle-event counters in the Sky Mapper.

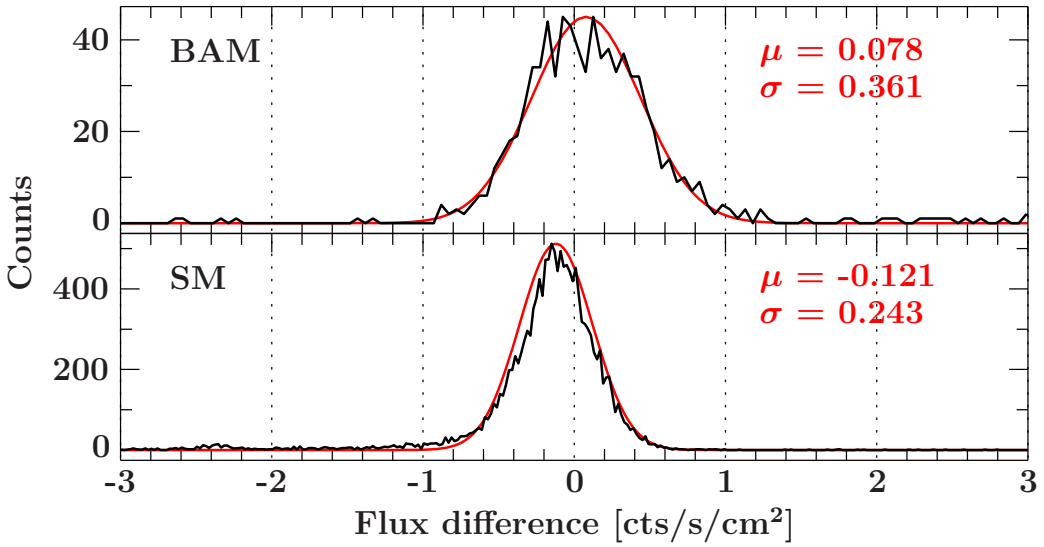

Figure 4.6: Excess flux of regularly sampled data to SIF data for both BAM and SM data. Gaussians were fitted to the peaks of both distributions, with their mean μ and standard deviation σ shown in the plot. While BAM-OBS measures a slight flux excess with respect to BAM-SIF, the PPEs appear to measure less tracks then the corresponding SIF observations.

4.3.1 Internal Comparisons

For the flux comparisons in this section, we will focus on comparing flux data derived from the same chips via different algorithms, as we will see in Sec. 4.3.2 that the different chips on *Gaia* actually see a different radiation environment. Concretely, this will mean that we compare fluxes from nominal BAM observations to BAM-SIF observations, and fluxes derived from PPE counters to fluxes from SM-SIF observations. This should once again trace systematics in the different extraction algorithms.

This choice means that for each source instrument, we have a regularly sampled dataset – BAM-OBS and SM-PPE – as well as an irregularly sampled dataset – BAM-SIF and SM-SIF. We will here examine the excess flux measured in the former compared to the latter.

In order to make this comparison, we first divide the entire time interval with available data (see Sec. 4.1) into five-minute intervals. We then calculate for each chip and FoV the mean flux for each time bin, by simply calculating the arithmetic mean of all CosmicObservation or PPE fluxes taken within that time bin, where available.

Keeping each chip and FoV separate, we then consider only time bins which have flux measurements in both the regularly sampled data and SIF data. For example, for the SM1 row 5 chip, we only consider PPE values when there is a CosmicObservation from that SM chip in the same time bin. For all these values, we calculate an excess flux by subtracting the SIF flux from the regularly sampled flux.

Figure 4.6 shows two histograms for this excess flux measured in both BAM and SM. As the distributions appeared to be the same for each FoV and chip, the plotted histograms are the sums of the individual histograms in the respective chips in order to get better statistics. This is especially important for BAM, as the BAM-SIF observations are poorly sampled.

As we can see in the plots, there are small systematic differences in the fluxes measured regularly and from SIF observations. These are also shown by the mean and standard deviations of Gaussians fitted to both distributions, motivated by the assumption that the statistical variations

are dominated by counting noise. Altogether, fluxes in BAM-OBS slightly exceed BAM-SIF fluxes, while PPE fluxes are slightly below SM-SIF fluxes. The broader fit in the BAM data is most likely explained by the lower effective area of a BAM readout window compared to the chip area read out on the SM chips (see Sec. 3.4.1), leading to a lower signal-to-noise ratio in BAM when both data are rebinned in time to the same sampling rate.

The causes behind these systematic offsets can only be guessed at without further examination – in the case of BAM data, it is possible that the slight excess in BAM-OBS fluxes come from the false positive detections due to shot noise of the interference pattern mentioned in Sec. 4.2.2. The differences in SM may be either due to false positive tracks detected in SIF observations or lower sensitivity in the PPE rejection algorithm.

In any case, these systematic offsets are small compared to typical solar quiet flux values measured in both SM and PPE data, which are between 2 to 4 $\mathrm{cts/s/cm^2}$, as seen in Sec. 4.3.2. As such, we can use the regularly sampled datasets BAM-OBS and SM-PPE in comparisons to rates from external particle detectors without losing significant signal compared to SIF data.

4.3.2 External Comparison and Solar Particle Events

After the internal validation, we will now compare the particle rates measured on *Gaia*'s FPA to the direct flux measurements of by dedicated particle instruments on other satellites. Unfortunately, as *Gaia* has been the only active spacecraft at L_2 since the start of its operations, we do not have a direct measurement of the L_2 particle environment to compare our data to. Instead, we will utilize data from satellites at L_1 and geostationary orbit. A similar analysis using just PPE data from the start of operations to mid-2015 has already been carried out by Abreu (2017).

The external particle data used here comes from live space weather data from the geostationary *GOES* satellites (Rodriguez et al., 2010) and the Solar Isotope Spectrometer (Stone et al., 1998) on the *Advanced Composition Explorer* orbiting L_1 (Zwickl et al., 1998). Data are provided as five-minute averaged differential fluxes in text files by the Space Weather Prediction Center of the U.S. National Oceanic and Atmospheric Administration and are archived at `ftp://sohoftp.nascom.nasa.gov/sdb/goes/particle/` and `ftp://sohoftp.nascom.nasa.gov/sdb/ace/daily/` for *GOES* and *ACE* respectively.

GOES and *ACE* proton fluxes are provided for particles above selected kinetic energies (5, 10, 30, 50 and 100 MeV for *GOES*, 10 and 30 MeV for *ACE*). For *Gaia* data, we use fluxes from BAM-OBS FoV 1 and PPE fluxes from the SM1 row 1 chip. We have decided to use a single FoV/chip for *Gaia* data in order to not crowd our plots.

Long term behavior

Fig. 4.7 plots these fluxes from January 2014 to January 2018. The panels separate data from different spacecraft, with source observations and energy thresholds being color coded. For this long-term plot, we utilized the Douglas-Peucker algorithm (Douglas & Peucker, 1973) in order to reduce the number of points plotted as seen especially in the > 100 MeV channel of *GOES*.

The two main features seen in this long term plot are a baseline flux level existing at all times and simultaneous, discrete events of increased flux in all detectors. It is easy to see that the baseline flux corresponds to galactic cosmic rays and that the increased flux events are solar particle events, both described in Chapter 1.

Upon closer examination, the baseline flux associated with GCRs evolves with time, as better

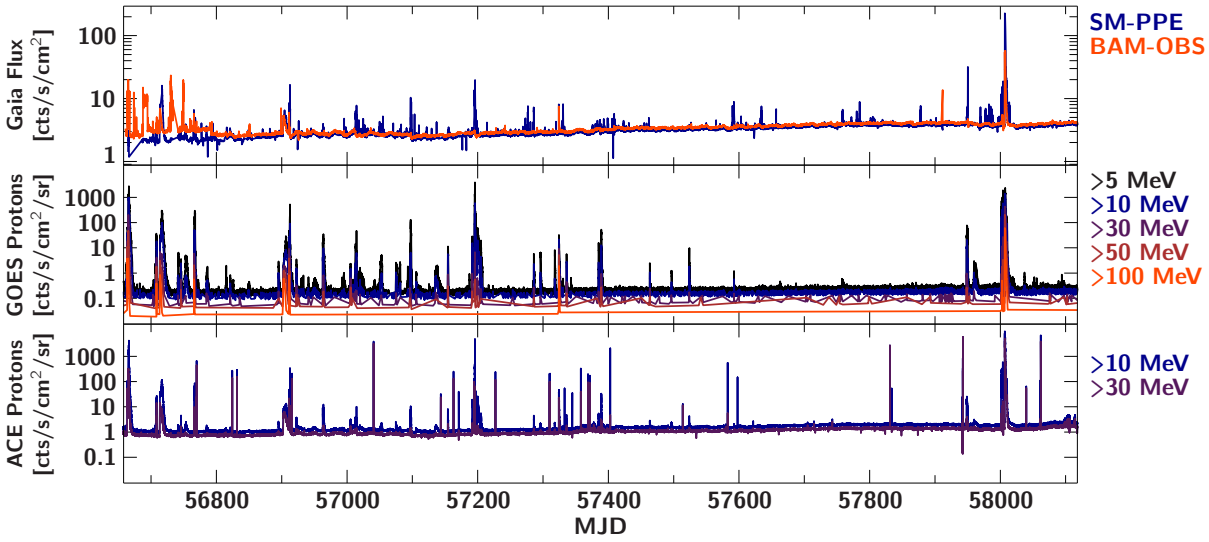

Figure 4.7: A comparison of particle fluxes measured by *Gaia* (top panel) to those measured by the *GOES-13* (middle panel) and *ACE* (bottom panel) satellites over four years. BAM data is taken from FoV 1, while PPE data is taken from row 1, FoV 1. *Gaia* and *GOES* fluxes were rebinned to one-hour intervals.

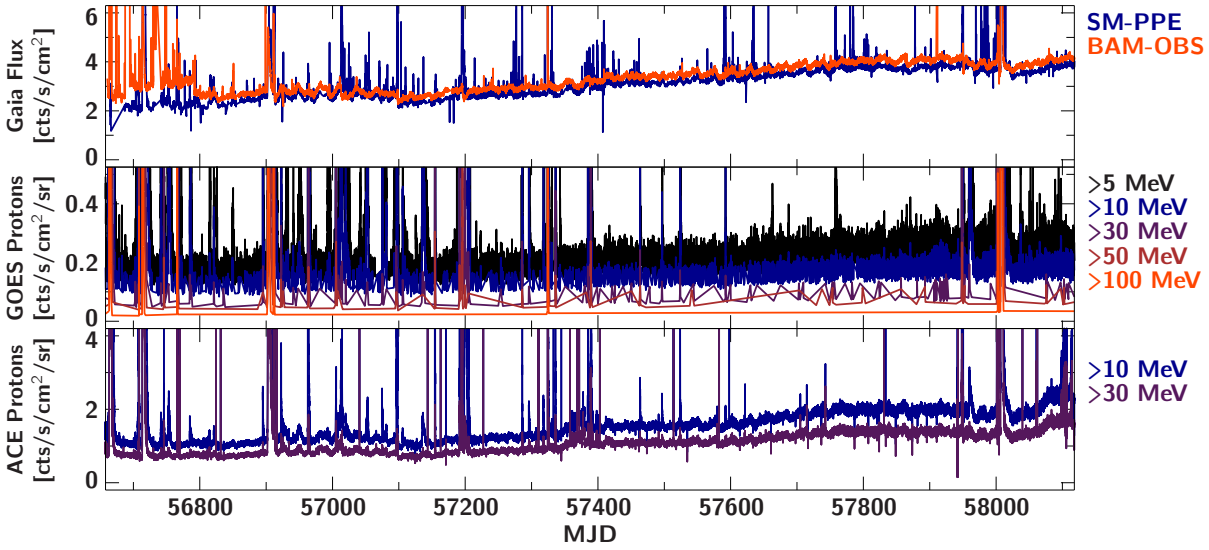

Figure 4.8: Particle fluxes as in Fig. 4.7, with linear scaling in flux focussing on the galactic cosmic ray background component. Over four years, this increases from roughly 2 to 4 cts/s/cm^2 in *Gaia*'s detectors.

seen in Fig. 4.8, which plots the same time range at a linear flux scale. As discussed in their introduction, the flux of galactic cosmic rays entering the extended heliosphere is modulated the 11 year solar cycle (Potgieter, 2013), being anticorrelated with solar activity. As *Gaia* operations started during solar maximum, we would expect an increase in the GCR rate with mission time, as we see here.

Visually, this non-linear modulation of GCR fluxes is very well-correlated in *Gaia* and *ACE* data. In *Gaia*, this flux increased from roughly 2 to 4 cts/s/cm^2 over the four years examined.

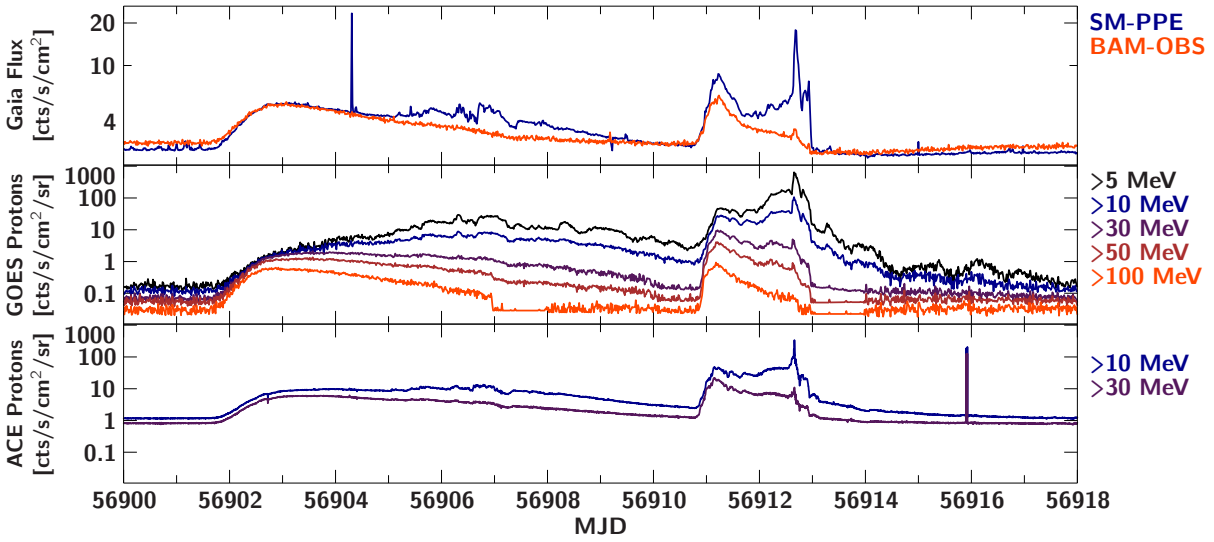

Figure 4.9: Two particle events around September 2014. Especially the second, double peaked burst shows a very interesting structure – namely, that the second peak is missing in BAM data. Comparing with the different energy bands in other satellites, it appears that the energy threshold to reach the BAM chip is higher than for the SM chips.

Before examining solar particle events in *Gaia*, there are two features of the GCR-induced fluxes to note in *Gaia*. First, one can see that BAM fluxes before MJD $\sim$ 56800 (mid 2014) are enhanced relative to the PPE fluxes and show frequent flaring. This time interval falls into *Gaia*'s commissioning phase, were BAM parameters changed more rapidly than during science operations, such that the BAM-OBS extraction algorithm relying on a stable pattern fails and detects false positives. This range of time also has many gaps in both BAM-OBS and PPE data and will not be further considered.

Aside from this early period, we still see a relative enhancement of the GCR background in BAM-OBS data relative to PPEs. This is most likely due to the reduced sensitivity of the SM chips to the minimum ionizing particles dominating the GCR background as discussed in Sec. 4.2.2, where we saw the same enhancement of BAM-OBS fluxes relative to SM-SIF fluxes.

Solar Particle Events

In the following, we will examine several solar particle events as observed by *Gaia*, *GOES* and *ACE*. As their temporal behavior shows very pronounced features, they will be a useful tool to examine the energy range of the particles seen on *Gaia*'s chips as well as differences of the radiation environment around the L_2 point compared to L_1 and geostationary orbit.

To start, Fig. 4.9 shows two particle events around September 2014. Surprisingly, these events look very different in BAM-OBS and SM-PPE data – while the first, more gradual event shows a modulation on top of its decay curve only SM, the second event shows an even stronger deviation, with a sharp secondary peak in flux that is missing in BAM-OBS data.

Comparing with flux profiles from other satellites, we see that this secondary peak appears to exist only for protons with lower energies – visually, the PPE data best matches the >10 MeV-flux in *ACE* data, while the BAM-OBS rates are closest to the highest energy protons seen by *GOES*.

This behavior is also seen in two particle events around October 2015, shown in Fig. 4.10. The

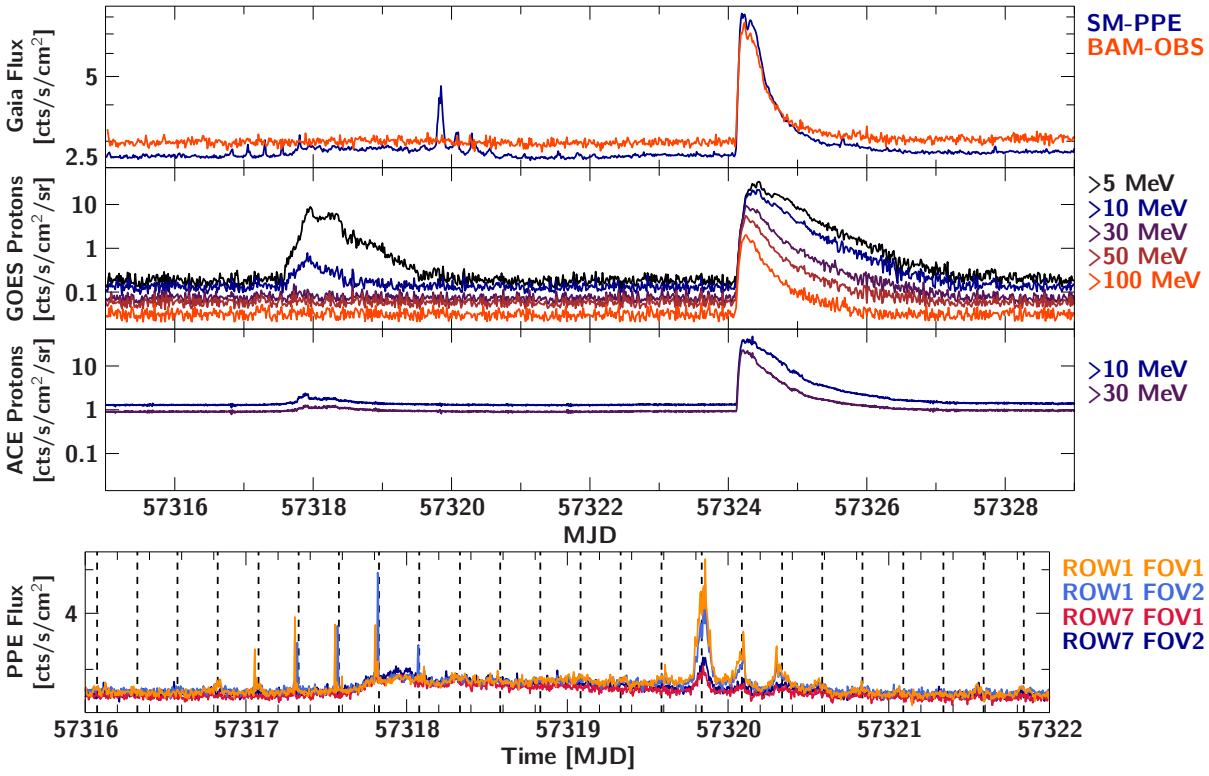

Figure 4.10: Two particle events around October 2015. The former event is not detected at all in BAM and barely in SM, while the latter event is almost identical in flux for both.
The lower plot shows the first outburst in different SM chips. Horizontal lines indicate times when the focal plane is facing the Sun during *Gaia*'s rotation and indicates a varying particle shielding as a function of the spacecraft spin phase.

first event, containing much relatively low-energy protons, is not at all seen in BAM-OBS data, while it is rather distorted in PPEs. In contrast, the second event, having a much harder proton energy distribution, appears almost identical in BAM and SM data.

The periodic modulations seen in the PPE rates of the first October 2015 event deserve further investigation and are shown for four different SM chips in the bottom plot of Fig. 4.10. We also show the spacecraft's rotation here, plotting in vertical dashed lines the times when the illuminated side of the FPA is directly facing the Sun. As Figure 2.2 indicates, this means that the telescopes' entrance windows are actually both facing away from the Sun and that, relative to the Sun, the cold radiator of the FPA is behind *Gaia*'s CCDs.

PPE modulations of this periodicity have been studied before by Abreu (2017). In that study, they were often found to be related to enhanced stray light from either the Sun or the Galaxy being rejected as particles by the VPAs. For galactic stray light, one would here expect an earlier peak in the FoV first passing over the galactic disk. While the sharp peaks before the event onset show such a tendency, the much broader peaks at the end of the event are simultaneous in all chips. Additionally, these peaks are much more pronounced in the first chip row of both fields of view, while stray light levels have been noted to be higher in FoV 2.

Altogether, such modulations in the observed particles in energetically soft solar particle events hint at a more complex shielding from solar events, depending both strongly on the spacecraft spin phase and location on the FPA. Due to their high mean energy loss, soft protons should be

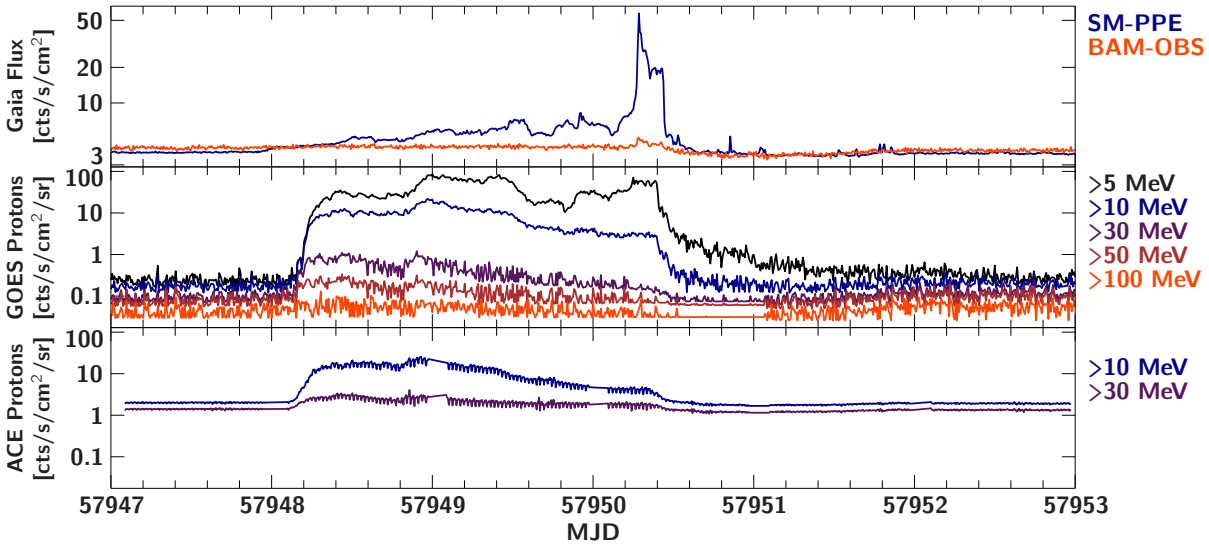

Figure 4.11: A particle event around July 2017. This event is only very weakly detected in BAM and strongly distorted in SM. Across all detectors, the time of peak flux appears to shift further back in time with increasing distance to the Sun.

most strongly affected by this shielding.

Figure 4.11 shows a further solar particle event in July 2017 with a very different appearance in *Gaia* data compared to other particle monitors. In both SM and BAM data, the strongest feature of this event is a sharp peak around early MJD 57950, seen as a very slight enhancement in the BAM flux. At this time, the event as seen in *ACE* is already strongly reduced in flux, while *GOES* sees an almost plateu-like event spanning as long as the event seen in both *Gaia* and *ACE*.

For CME events, such differences have been seen in spacecraft observing the same event at different solar longitudes (Reames, 1999), where the onsets of the sharper peaks are associated with the CME shock front passing by the relative spacecraft location. This event appears to trace a similar difference in the shock arrival along the Sun-Earth axis.

The last events discussed here demonstrate the limits of *Gaia*'s particle measurements, being the largest solar event seen in the current solar cycle so far, which we will refer to as the September 2017 event. This event, whose effect on ESA's satellites was described in a press-release by the ESA Space Environments & Effects Section (2017), was caused by a X9.3 class solar event on September 6, followed by an X8.2 flare on September 10, both accompanied by two strong CMEs. These events caused significant disturbances in satellite operations, for instance putting ESA's *Integral* observatory into safe mode. Both solar particle events as seen by the monitors used here are shown in Fig. 4.12.

While the sampling in *ACE* SIS for the first event is unfortunately sparse, comparing the fluxes from *GOES* with *Gaia* data once again demonstrates the different entrance energies for the BAM and SIF chips, with very little activity in BAM before mid MJD 58002. Compared to the latter event, the peak intensities of this softer event are also rather low in *Gaia*.

The second event, starting September 10, peaks at rates an order of magnitude above all other events observed in *Gaia* (see Fig. 4.7). The intensity curve in BAM-OBS shows an interesting feature here, decreasing suddenly after a sharp rise in flux. Examining the source

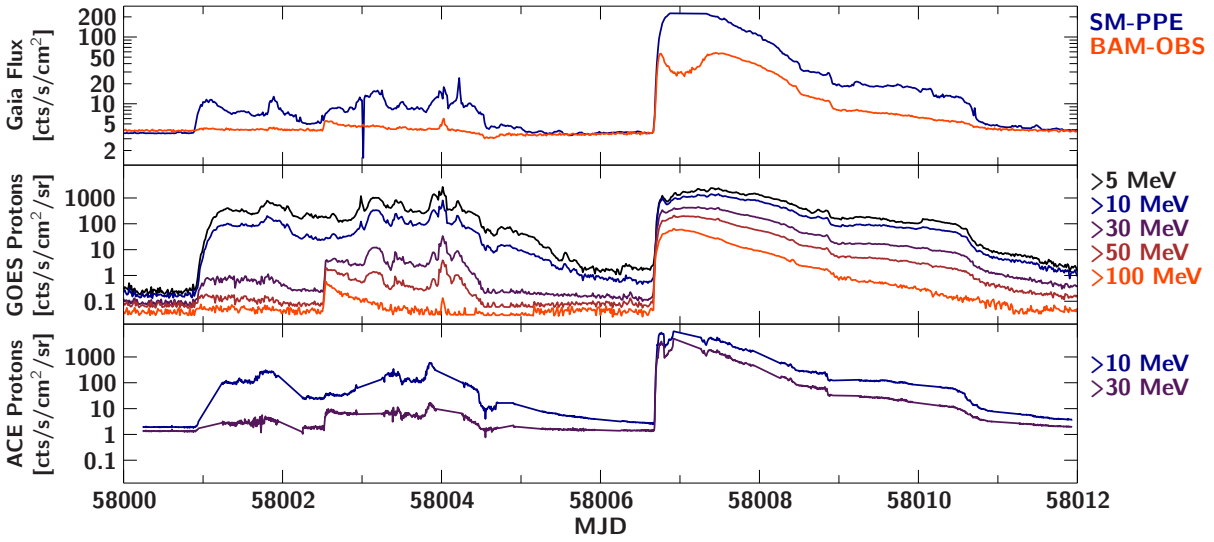

Figure 4.12: The particle event of early September 2017, which is the strongest event within *Gaia*'s mission time. The gradual event up to MJD 58006 (Sept 10) nicely demonstrates the different energy ranges of BAM and SM, while second event appears to bring all detectors to their limits – while the SM-PPE data peak at a fixed value, the BAM-OBS data decreases towards during the peak of flux in other detectors.

CosmicObservations, this appears to be the result of pile-up; There are so many individual tracks on the BAM image that they start overlapping and can not be separated from each other, leading to a lower amount of individual events. When observed closely, the PPE counters also run into their own limits, plateauing to a flat value during the time of peak flux, implying that the counters were saturated during this event.

Observing the long decay of the second particle event, we once again see nice correlations between measurements in *Gaia* and other satellites, showing relatively sharp features at roughly the same times.

Having examined the signature of several solar particle events, we see that Gaia detects the solar particle events seen by other satellites rather well. The main remaining uncertainty is the cause behind the different energy cutoffs for particles measured on the BAM and SM chips. As we see a higher energy cutoff in the BAM chips, this is most likely due to some additional shielding for this chip. Without detailed modeling, there are two possible effects that come to mind.

The first possible reason may simply be the positioning of the BAM chips in the FPA. As seen in Figs. 2.3 and 2.6, the BAM chips are located near one of the corners of the FPA and thus very close to the walls of the cold radiator. They are forther walled of from the SM chips by an additional vertical vane. As shown in a previous sector analysis (Fig. 2.5), the BAM chips are indeed expected to be exposed to less protons over the whole mission. Given that we see approximately the same on-chip rate from GCRs on the BAM and SM chips, these extra irradiance on the SM chips should come from solar events.

A second shielding factor may be an additional optical component installed in front of the BAM chips, namely the *BAM optical density assembly* (BDA in Fig. 2.6). This component places an ND filter in front of the BAM chips. While an ND filter would most likely not completely stop these cosmics, given that they reach the SM through all of *Gaia*'s shielding, this component most likely does contribute to some aspect of the BAM CCD's additional shielding.

Since a confirmation of either scenario would require particle transport simulations with detailed models of the whole spacecraft and FPA, we will leave this discrepancy as an aspect of future work.

4.4 Measurements of Energy Loss

As the post-processing pipeline used to produce CosmicObservations estimates the length of a particle's path through the detector for a subset of observed tracks, we can measure one of the most important kinematic variables for charged particle detections, the energy loss per unit length of a particle dE/dx. This variable, as discussed in Chapter 1, is a measure of a particle's kinetic energy.

Given a CosmicObservation, making such a histogram is simple – for every track with a measured length, one only needs to divide the total track energy by the track length. The track energy in eV can once again be obtained from the measured value in signal electrons by the mean ionization energy of silicon, 3.6 eV.

As only a fraction of the tracks in a CosmicObservation have an estimated length, proper statistics require a combination of multiple observations. Like in Sec. 4.2, we can generate a differential counts-per-dE/dx-bin histogram for every used observation and sum up all histograms per bin, weighting by the flux measured in each individual observations. The combined differential histogram can then be normalized such that the integral over the energy loss equals the mean flux of all CosmicObservations used in their generation, such that we can search for flux excesses in at different energy losses.

Fig. 4.13 shows two such histograms using each a full day of data from BAM-OBS FoV 1. The chosen time intervals are before and during the September 2017 particle event discussed in Section 4.3.2. Both distributions have a broad peak between 200 and 300 eV/μm. For the solar quiet day, the number of particles with higher energy losses then decays nearly exponentially – as one would expect given the Creme96 particle background in Fig. 4.2.

During the solar particle event, we detect an excess flux at all energy losses, with the largest relative excess at energy losses higher than the most probable energy loss. This makes sense if we assume that the quiescent peak represents MIPs, as we see in Fig. 4.12 a significant excess of particles below MIP energies from the solar particle event.

The assumption that the most probable energy loss measured by CosmicObservations corresponds to that of minimum ionizing particles is not straightforward to confirm, as the most probable energy loss in a detector is itself a function of the path length through the detector (Tanabashi et al., 2018). The relation between most probable energy loss and detector thickness for silicon is shown in Figure 4.14.

Given that the particle entrance angles and thus track lengths strongly vary in our data, this means that we cannot determine one most probable energy loss. To make an estimate nonetheless, we may assume that the shortest tracks have lengths around or above the 80 μm given in Fig. 4.14, as particles with an assigned track length must pass through several pixels. Taking the values for minimum ionizing particles from the Fig. 4.14, we would expect most probable energy losses between 60% and 70% of the mean MIP energy loss, meaning values between 230 and 270 eV/μm. This roughly matches the peak in Fig. 4.13.

As we expect a MIP-dominated particle background outside of solar particle events, this admittedly rough estimation implies that it is possible to measure energy losses using CosmicObservations to some accuracy. Fully reproducing the measured distributions from theory

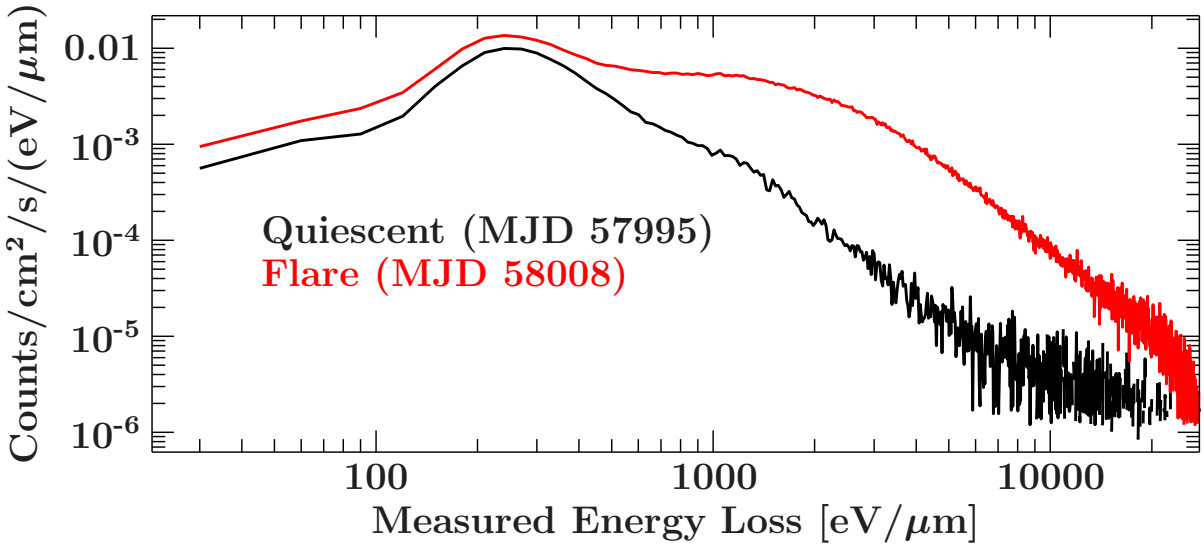

Figure 4.13: Differential energy loss histogram for BAM-OBS data before and during the September 2017 event (see Fig. 4.12 for fluxes). The quiescent spectrum shows a maximum between 200 and 300 eV/μm, followed by a monotonic decrease, while the outburst shows the strongest relative excess of particles with higher energy losses.

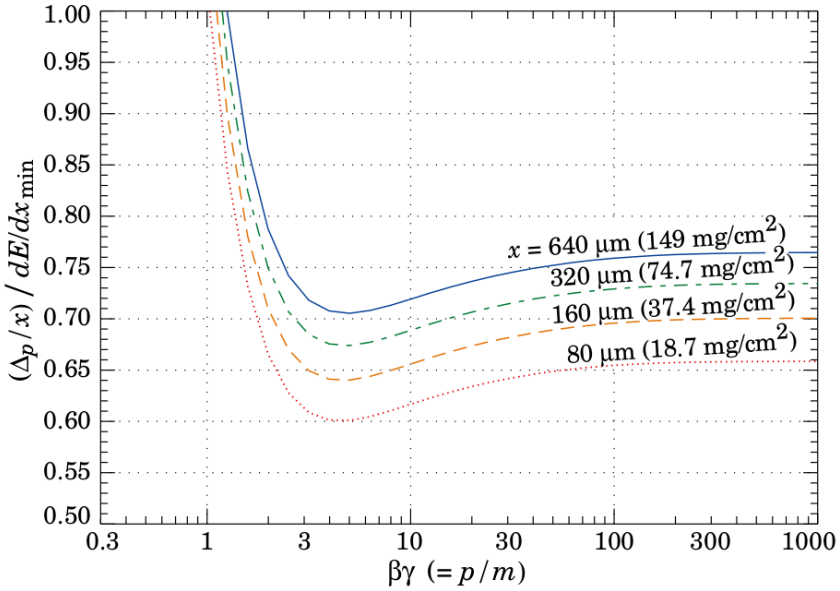

Figure 4.14: Most probable energy loss in silicon for several detector thicknesses, scaled to the mean loss of a minimum ionizing particle, 388 $eV/\mu m$. Figure and caption taken from Tanabashi et al. (2018)

would however require a significantly more thorough treatment, taking into account the full expected particle energy distribution, an incident angle distribution used to calculate path lengths and proper modeling of the energy deposition process. Most likely, such a distribution is best generated by a Monte Carlo simulation using for instance a Geant4-based tool. As this lies far outside the scope of this thesis, it is left for future work.

Chapter 5

Summary and Outlook

Within this work, I have successfully developed a suite of algorithms to extract the cosmic ray background signal from raw *Gaia* images, producing a large catalog of cosmic ray tracks in those images via custom software pipelines. This dataset improves on the *Gaia*'s existing cosmic ray data, which provided only particle count statistics, by extracting individual event properties such as the ionizing energy deposited on the chip. The most regularly sampled dataset provides two separate measurements of *Gaia*'s cosmic ray background every 24 seconds. When possible, the length and orientation of cosmics are also estimated.

Following the catalog generation, I inspected the produced dataset, comparing measurements of the same particle background from different observations with each other. While there are slight systematic deviations between the datasets, they are mostly consistent in both the rate of detected cosmics and their deposited energies.

Comparing the on-chip particle rates with data from satellites at the Sun-Earth L_1 point and geostationary orbit, we find that the cosmic rays producing *Gaia*'s background signal consist of galactic cosmic rays modulated by the solar cycle as well as energetic particles ejected in solar particle events. The evolution and modulations of galactic cosmic rays match the same modulations at L_1 rather well, while solar particle events observed in the other satellites are also observed in *Gaia*, provided they contain particles with sufficiently high energies to penetrate the spacecraft shielding. Data from different chips reveals strong differences in radiation shielding across *Gaia*'s focal plane, as known from previous particle transport modeling.

For tracks with a measured track length, the newly produced data also provide a rough measurement of the energy loss per unit length of the observed particles, which are consistent with a GCR background dominated by minimum ionizing particles and lower energy particles in solar particle events.

This dataset, along with the existing cosmic ray count statistics, closes a time gap of measurements of the radiation environment at the Sun-Earth L_2 point, as *Gaia* is the only active spacecraft orbiting this point since the start of its operations in early 2014. It further provides excellent measurements of the cosmic ray signal background of silicon-based detectors at L_2, which is especially relevant given that the majority of future observatories planning to orbit L_2 will carry such detectors. As such, this dataset provides an excellent tool for planning future space observatories, especially if their radiation shielding is expected to be similar to that of *Gaia*.

Another possibility for the use of this dataset is the study of the radiation environment at L_2 itself, especially with respect to the propagation of solar particle events along the Sun-Earth axis. Some concrete applications would be measurements of the arrival time differences of solar

particle events as a function of the distance to the Sun and the evolution of CME shocks while passing by Earth. While not used in the thesis proper, there also exist tracking data of *Gaia*'s position around the L_2 point (see Appendix B.3), which can be used to correlate *Gaia*'s particle background with its position relative to Earth's magnetotail.

In order to improve the quality of this dataset, detailed modeling of the transport of cosmic rays through the *Gaia* spacecraft can be used to "calibrate" this dataset, in order to calculate geometry factors to convert raw on-chip count rates to actual differential particle fluxes. Outside the spacecraft. Existing Geant4-based tools could be utilized for such efforts. This would vastly improve *Gaia*'s capabilities as a radiation monitor for the L_2 environment.

Lastly, the measurement of the energy deposited on *Gaia*'s chips via ionization added by this dataset can be correlated with existing measurements of the radiation damage sustained by its CCDs in order to further improve the understanding of their degradation by cosmic rays.

Acknowledgements

The majority of this project, including the entire dataset generation, was carried out within the framework of the European Space Astronomy Center's Trainee Project, specifically the 2017 project "Radiation in L_2: *Gaia* Data Analysis". My thanks go to the project tutors, Asier Abreu, Cian Crowley, Juan Martin-Fleitas, Alcione Mora and Uwe Lammers, without whom none of this would have been possible. Special thanks go to Asier Abreu, the primary tutor for this project, who has supported me in any possible way during my work. Cian Crowley, Alcione Mora and Ralf Kohley also provided extremely valuable input to the specifics of the datasets used in this project. In general, I would like to thank all members of the *Gaia* team at ESAC for providing a great working environment.

I would also like to thank all Student and Young Graduate Trainees I've met at ESAC for many hours spent together in offices, at lunch, in the evenings and lazing about in ESAC's social club. Special mentions go to Markus Grass for sharing a large and otherwise empty office with me during the not-so-cold Spanish winter months.

Lastly, as far as ESAC goes, I want to thank what feels like at least half the staff of ESAC commuting by car for letting me ride with them on the last two kilometers to and from the nearest bus stop and allowing me to practice my self-introduction and the elevator-pitch for this project.

My heartfelt thanks go to Paola Perego and Carlos Gonzalez for letting me live with them during my stay in Madrid and for generally helping me get used to life in Spain.

As for my Bachelor's thesis, my work on this project after returning from ESAC was done at the Remeis observatory in Bamberg under the supervision of Jörn Wilms. I would like to thank him for allowing me to continue this analysis and his input therein, as well as all observatory members for the great working atmosphere after coming back and for sharing cake. Many thanks as always to the administrators at the observatory for their daily work keeping everything running.

Finally, I'd like to thank my family at home for everything outside of work.

My stay in Madrid was financially supported both by ESAC and the Studienstiftung des Deutschen Volkes e.V. Both the latter and the Max Weber-Program of the Free State of Bavaria supported my studies via their scholarships.

Particularly in the analysis of the produced dataset, this thesis has made use of a collection of ISIS functions (ISISscripts) provided by ECAP/Remeis observatory and MIT (`http://www.sternwarte.uni-erlangen.de/isis/`).

Bibliography

Abreu A., 2017, Radiation Environment and Cosmics from Gaia at L2, Gaia TN GAIA-CA-TN-ESAC-AAA-035-1

Ackermann M., Ajello M., Allafort A., et al., 2013, Science 339, 807

Adams L., 1985, Microelectronics Journal 16, 17

Anchordoqui L.A., 2018, ArXiv e-prints

Bastian U., 2004, Reference Systems, Conventions And Notations for Gaia, Gaia TN GAIA-CA-SP-ARI-BAS-003

Battarbee M., Guo J., Dalla S., et al., 2018, Astronomy & Astrophysics 612, A116

Bennett C.L., Bay M., Halpern M., et al., 2003, The Astrophysical Journal 583, 1

Berger M., Coursey J., Zucker M., Chang J., 2005, ESTAR, PSTAR, and ASTAR: Computer Programs for Calculating Stopping-Power and Range Tables for Electrons, Protons, and Helium Ions (version 1.2.3), `http://physics.nist.gov/Star`, accessed 2018-10-15

Blasi P., 2013, The Astronomy and Astrophysics Review 21, 70

Boggs P.T., Donaldson J.R., Byrd R.H., Schnabel B., 1989, ACM Trans. Math. Softw. 15, 348

Crowley C., Kohley R., Hambly N.C., et al., 2016, Astronomy & Astrophysics 595, A6

de Bruijne, J. H. J.Allen, M.Azaz, S.et al., 2015, Astronomy & Astrophysics 576, A74

Desai M., Giacalone J., 2016, Living Reviews in Solar Physics 13, 3

Douglas D.H., Peucker T.K., 1973, Cartographica: The International Journal for Geographic Information and Geovisualization 10, 112

Eckart M.E., Adams J.S., Boyce K.R., et al., 2018, Journal of Astronomical Telescopes, Instruments, and Systems 4, 021406

ESA Space Environments & Effects Section 2017, X-class Flares and Solar Particle Event of September 2017, `http://space-env.esa.int/index.php/ESA-ESTEC-Space-Environment-TEC-EPS/articles/SEP092017.html` [Online; accessed 28-10-2018]

Fitzpatrick R., 2012, An Introduction to Celestial Mechanics, Cambridge University Press

Gaia CollaborationBrown, A. G. A.Vallenari, A.et al., 2018, Astronomy & Astrophysics 616, A1

Gaia CollaborationPrusti, T.de Bruijne, J. H. J.et al., 2016, Astronomy & Astrophysics 595, A1

Garcia L., Prod'homme T., Lucsanyi D., et al., 2018, In: Society of Photo-Optical Instrumentation Engineers (SPIE) Conference Series, Vol. 10709. Society of Photo-Optical Instrumentation Engineers (SPIE) Conference Series, p. 1070919

Gardner J.P., Mather J.C., Clampin M., et al., 2006, Space Science Reviews 123, 485

Gastaldello F., Ghizzardi S., Marelli M., et al., 2017, Experimental Astronomy 44, 321

Harwit M., 2004, Advances in Space Research 34, 568

Hathaway D.H., 2015, Living Reviews in Solar Physics 12, 4

Hess V.F., 1912, Physikalische Zeitschrift 13, 1084

Horne R.B., Glauert S.A., Meredith N.P., et al., 2013, Space Weather 11, 169

Klein K.L., Dalla S., 2017, Space Science Reviews 212, 1107

Kohley R., 2015, Cosmic Rays on BAM CCDs data delivery note, Gaia TN GAIA-DE-TN-ESAC-RKO-033

Kohley R., Garé P., Vétel C., et al., 2012, In: Space Telescopes and Instrumentation 2012: Optical, Infrared, and Millimeter Wave, Vol. 8442. Proceedings of the SPIE, p. 84421P

Landau L., 1944, J. Phys.(USSR) 8, 201

Lindegren L., Hernández J., Bombrun A., et al., 2018, Astronomy & Astrophysics 616, A2

McCully C., 2015, Astro-SCRAPPY: The Speedy Cosmic Ray Annihilation Package in Python, `https://github.com/astropy/astroscrappy`

Miniussi A., Puget J.L., Holmes W., et al., 2014, Journal of Low Temperature Physics 176, 815

Mohammadzadeh A., Evans H., Nieminen P., et al., 2003, IEEE Transactions on Nuclear Science 50, 2272

Molendi S., 2017, Experimental Astronomy 44, 263

Mora A., Biermann M., Bombrun A., et al., 2016,

In: Space Telescopes and Instrumentation 2016: Optical, Infrared, and Millimeter Wave, Vol. 9904. Proceedings of the SPIE, p. 99042D
Nandra K., Barret D., Barcons X., et al., 2013, ArXiv e-prints
Pavlinsky M., Sunyaev R., Churazov E., et al., 2008, In: Space Telescopes and Instrumentation 2008: Ultraviolet to Gamma Ray, Vol. 7011. Proceedings of the SPIE, p. 70110H
Potgieter M.S., 2013, Living Reviews in Solar Physics 10, 3
Reames D.V., 1999, Space Science Reviews 90, 413
Rodriguez J.V., Onsager T.G., Mazur J.E., 2010, Geophysical Research Letters 37, L07109
Salzberg S., Chandar R., Ford H., et al., 1995, Publications of the Astronomical Society of the Pacific 107, 279
Schwenn R., 2006, Living Reviews in Solar Physics 3, 2
Spieler H., 2005, Semiconductor detector systems, Vol. 12, Oxford university press
Stone E., Frandsen A., Mewaldt R., et al., 1998, Space Science Reviews 86, 1
Stone E.C., Cohen C.M.S., Cook W.R., et al., 1998, Space Science Reviews 86, 357
Sullivan J., 1971, Nuclear Instruments and Methods 95, 5
Tanabashi M., Hagiwara K., Hikasa K., et al., 2018, Phys. Rev. D 98, 030001
Tauber, J. A.Mandolesi, N.Puget, J.-L.et al., 2010, Astronomy & Astrophysics 520, A1
Tylka A., Adams J.J., Boberg P., 1997, IEEE Transactions on Nuclear Science 44
van Dokkum P.G., 2001, Publications of the Astronomical Society of the Pacific 113, 1420
Walsh B.M., Kuntz K.D., Collier M.R., et al., 2014, Space Weather 12, 387
Zwickl R., Doggett K., Sahm S., et al., 1998, Space Science Reviews 86, 633

Appendix A

Gaia Acronyms

AC	Across Scan
AL	Along Scan
AF	Astrometric Field
SM	Sky Mapper
BAM	Basic-Angle Monitoring device
CCD	Charge-Coupled Device
TDI	Time Delay Integration
SIF	Service Interface Function
FITS	Flexible Image Transport System
FoV	Field of View
FPA	Focal-Plane Assembly
OBMT	On-Board Mission Time
UTC	Coordinated Universal Time
°	degree; unit of angle
’	arcminute, minute of arc; unit of angle
”	arcsecond, second of arc; unit of angle

Appendix B

Data Models

This appendix summarizes the data model chosen for storing the main dataset of *CosmicObservations*, as well as the data model for flux tables and auxillary data of the spacecraft spin phase and (so far unused) spacecraft location.

B.1 Main Dataset Description

Entity Name: *CosmicObservation*

Entity Description: A table of cosmic ray (prompt particle event) detections from any of the analyzed *Gaia* CCDs

Entity Header:

Table B.1: CosmicObservation table header version v1.0

Name	***Description***	***Unit***	***Type***
SOURCE	Descriptor of the type of source observation	NA	String
CCD_ROW	CCD row of the source chip	NA	Short
FOV	FoV of the source chip	NA	Short
ACQTIME	Source acquisition time	OBMT	Integer
ACQDATE	Source acquisition time	UTC	String
SRC_AL	AL-dimension of the source image	pixels	Short
SRC_AC	AC-dimension of the source image	pixels	Short
MASKPIX	Number of masked pixels in the source image	pixels	Short
FLUX	Estimated particle flux	$\mathrm{particles\,cm^{-2}\,s^{-1}}$	Float
FLUX_ERR	Poisson Uncertainty of estimated particle flux	$\mathrm{particles\,cm^{-2}\,s^{-1}}$	Float

Entity Columns:

B.2 Flux Dataset Description

We provide additional files listing just the measured flux per observation, sorted by the source observation type and chip. A file has been generated for each source type whose extraction has been defined above, as well as for the PPE counters (named SM-PPE).

Entity Name: *FluxTable* **Entity Description**: A table of cosmic ray fluxes from any of the analyzed *Gaia* CCDs

Table B.2: CosmicObservation table version v1.0

Name	***Description***	***Unit***	***Type***
LOC_AL	The start position of the event in the AL direction	pixels	Short
LOC_AC	The start position of the event in the AC direction	pixels	Short
DIM_AL	Event track dimension in AL	pixels	Short
DIM_AC	Event track dimension in AC	pixels	Short
TRACK_NPIX	Number of detected pixels	pixels	Short
TRACK_EN	Event track total energy	electrons	Integer
TRACK_EN_ERR	Uncertainty in the event track total energy	electrons	Integer
TRACK_TRUNCATED	Is the event truncated by start/end of CCD physical area	NA	Boolean
GEOMETRY_VALID	Is the track geometry (following rows LEN, THETA) applicable?	NA	Boolean
TRACK_LEN	Estimated incident particle track length	μm	Float
TRACK_LEN_ERR	Uncertainty in the estimated incident particle track length	μm	Float
TRACK_THETA	Estimated incident particle impact angle	deg	Float
TRACK_THETA_ERR	Uncertainty in the estimated incident particle impact angle	deg	Float

Entity Header:

Table B.3: Flux table header version v1.0

Name	***Description***	***Unit***	***Type***
SOURCE	Descriptor of the type of the source	NA	String
CCD_ROW	CCD row of the source chip	NA	Short
FOV	FoV of the source chip	NA	Short

Entity Columns:

Table B.4: Flux table version v1.0

Name	***Description***	***Unit***	***Type***
COUNTS	Number of particles in the corresponding observation	NA	Integer
FLUX	Estimated particle flux	$\mathrm{particles\,cm^{-2}\,s^{-1}}$	Float
FLUX_ERR	Poisson Uncertainty of estimated particle flux	$\mathrm{particles\,cm^{-2}\,s^{-1}}$	Float
TIME	Source acquisition time	MJD	Float
DATE	Source acquisition time	UTC	String

B.3 Auxillary Datasets Description

The auxillary datasets are composed of the spin phase of the spacecraft as well as the location of the spacecraft in a co-rotating geocentric coordinate system.

B.3.1 Spacecraft Spin Phase

The spin phase of the spacecraft yields information on the orientation of the FPA to the Sun. It is saved in a FITS file with a single table extension, listing

- A time coordinate in units of MJD
- The spacecraft spin phase in units of degrees

The spin phase is defined such that an angle of 180°, the FPA is facing towards the Sun. This has been further analyzed in the context of cosmic rays in Abreu (2017).

B.3.2 Spacecraft Location

A low-resolution table of the spacecraft location as a function of time has been calculated and is provided in a FITS file.

The coordinate system used is a geocentric ecliptic coordinate system. The X axis points away from the Sun along the Sun-Earth line, while the Y axis is perpendicular to the X axis, pointing in the direction of Earth's orbital motion. The Z axis is defined to complete the right-handed coordinate system. This defines a co-rotating system to the Sun-Earth system. The definition of X and Y are in this case the opposite of the Geocentric Solar Ecliptic system.

The provided FITS file has a single table extension, listing

- A time coordinate in units of MJD
- The X, Y and Z coordinates of the spacecraft, in units of m.

Appendix C

Persistence Considerations

This appendix describes the concrete storage method for the datasets described in Appendix B and estimates their current size in storage.

C.1 Persistence Method(s)

CosmicObservations, fluxes and auxillary data are currently stored in FITS files, with the CosmicObservations being in a date separated directory structure (following yyyy/mm/dd/). Each day-folder contains BAM-OBS files separated by the FoV, each file containing up to 500 CosmicObservations. If there are SM-SIF or BAM-SIF observations available for this day, they are saved in one file per source (i.e. at most one file for SM-SIF, one for BAM-SIF), each containing all the CosmicObservations for that source, regardless of CCD row and FoV.

The fluxes are saved in a single FITS file per source (BAM-OBS, SM-SIF, ...), each containing the tables of that dataset for each CCD row and FoV separately.

The auxillary datasets are saved in one FITS file each.

C.2 Size Estimations

Detection algorithms have been developed and written in Python and the default persistence method adopted is TBD. This results in the following estimations.

Note: the following estimations are applicable to catalog version : v1.0

The size of the output catalog of CosmicObservations per year can be estimated by extrapolating the size of the datasets for each fully extracted year so far, listed in Table C.1.

Table C.1: Data volume for CosmicObservations per year for catalog version v1.0

Year	CosmicObservation data volume [GB]
2014	22
2015	23
2016	26
2017	29

It can be clearly seen that the data volume per year is increasing with mission time. This has to do with the fact that the baseline level of galactic cosmic rays in every observation is increasing as solar activity is moving toward solar minimum, less effectively shielding the inner solar system.

The data volume is entirely dominated by the BAM-OBS dataset, whose rate of acquisition is constant. While SM-SIF observations are becoming more frequent as the mission progresses, this only has a minimal effect on the overall catalog size.

Extrapolating from Table C.1, we assume that the average added data volume per year is 30 GB, assuming that the increasing flux in galactic cosmic rays in further years is offset by the low flux during the early mission. This leads to an estimated catalog size of 30 GB/year, or 2.5 GB/month.

Table C.2 lists the size of the datasets for the fluxes and auxillary data, from January 2014 to January 2018. The flux data groups all datasets (SM-SIF, SM-PPE, BAM-SIF, BAM-OBS) and is dominated by the BAM-OBS and PPE data, whose sampling is constant and the only scaling factor for the catalog size. The spin phase and spacecraft location data sizes are dominated by the sampling at which they are provided.

Table C.2: Data volume for fluxes and auxillary datasets for catalog version v1.0

Dataset	Data volume Jan 2014 - Jan 2018 [MB]
Flux	663
Spin Phase	69
Spacecraft Location	6.5

Extrapolating from Table C.2, we find that the flux dataset has an approximate size of 165 MB/year, the spin phase a size of 17 MB/year and the spacecraft location a size of 1.6 MB/year.

Erklärung

Hiermit bestätige ich, dass ich diese Arbeit selbstständig und nur unter Verwendung der angegebenen Hilfsmittel angefertigt habe.

Ort, Datum	Christian Kirsch